Modelling lava rheology with free surface velocimetry and analogue fluids

---

A thesis submitted in partial fulfilment
of the requirements for the degree
of
MASTER OF SCIENCE
at the
UNIVERSITY OF CANTERBURY
by

Dale Robert Cusack

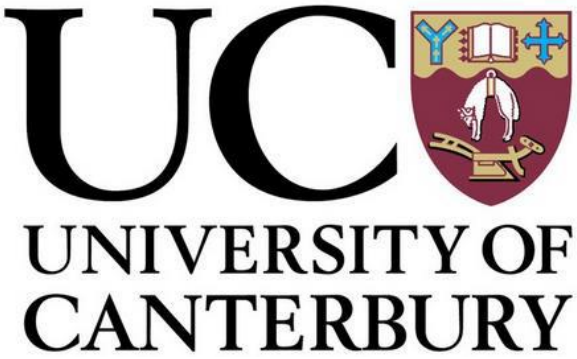

UNIVERSITY OF CANTERBURY 2019

Hawaiian pahoehoe Credit: U.S. Geological Survey Department of the Interior

Abstract

Lava flows are a recognised natural hazard that can extend into inhabited or economically sensitive regions. The ability to forecast lava flow paths is dependent on an understanding of the lava rheology. The aim of this work is to investigate the relationship between rheology and free surface velocity to enable the runout distances and flow paths of active lava flows to be calculated. Lava rheology is complex and flows can be either Newtonian, non-Newtonian or a mixture of both in nature. Lava viscosity is not only temperature dependent but also dependent on bubble and crystal growth.

The approach is to initially simplify the conditions. Isothermal Newtonian and non-Newtonian fluids are used as lava analogues in the initial experimental approach. The fluids are poured down an inclined V channel under gravity and small polystyrene beads are scattered over the free surface. A video of the fluid flow is captured when it is fully developed and in a steady state as it moves down the channel. The free surface streamwise velocity is determined using Streams video processing software and the entrained flow of the polystyrene beads sitting on the fluid's free surface.

A COMSOL based Navier-Stokes model was developed to simulate the flows that were measured in the experiments. The free surface velocity was used as an input to the COMSOL model where viscosity is iteratively changed to find a match. In both the Newtonian and non-Newtonian fluids, viscosity was determined and compared with a commercial rheometer. The Newtonian fluid's viscosity, μ was measured to be 61.4 ± 0.5 Pa·s in the viscometer, and calculated to have a mean viscosity of 61 ± 7.8 Pa·s for the model. The non-Newtonian fluid's viscosity is encompassed in the power law coefficients. For the rheometer they were $k = 14$ and $n = 0.4$. The experimental results were $k = 21.65 \pm 1.15$ and $n = 0.205 \pm 0.015$.

It was discovered that the model is very sensitive to the accurate measurement of the independent variables flow height, h which had a measurement error of $\pm$ 1.5 mm and inclination angle, β which had a measurement error of $\pm$ 0.5°. This leads to a velocity uncertainty $\pm$ 1.2 mm/s, and a viscosity variation of $\pm$ 7.8 Pa·s.

Acknowledgements

I would like to thank my MSc supervisors Ben Kennedy and Mathieu Sellier for their guidance and encouragement. It was Ben's challenge to do something with my summer research project data and Mathieu's brilliant ability to explain mathematics clearly and simply that drew me into the world of rheology.

A very special gratitude goes out to James Hewett who tirelessly answered all the engineering questions I threw at him and for the outstandingly detailed reviews of my work.

I wish to thank Phoebe Fordyce, Janina Gillies and Jim Cole for their fantastic assistance in editing my writing.

I am grateful for the help Professor Ken Morrison gave me in the Chemical and Process Engineering laboratory with the viscometer, refractometer and rheometer.

I am also grateful to the following university staff: Matt Cockcroft, Chris Grimshaw, and Sacha Baldwin for their unfailing support and assistance.

And finally, last but by no means least the amazing people who contribute to the support forums for MATLAB, Python and COMSOL, for without whose time I would still be scratching my head.

Dale Cusack

Contents

Chapter One: Introduction

As human life expands closer to volcanoes the hazards that they pose to society increase (Fournier d'Albe, 2007; Doocy, Daniels, Dooling, & Gorokhovich, 2013; Behncke & Neri, 2003). The recent volcanic activity in Hawaii has shown the destructive potential of lava flows (Neal et al., 2019). Civil defence agencies struggled to predict the path that lava flows would take, making evacuations difficult to prioritise (Kim, Pant, & Yamashita, 2018). It was also difficult for hazard managers and scientists to determine how long it would take flows to reach critical infrastructure such as the Puna Geothermal Venture power plant which was storing 220, 000 litres of pentane on site. These gaps in our knowledge highlight the need for further research into lava flow behaviour in order to assist with hazard management.

Lava flows come in different forms depending upon the nature of the magma beneath the volcanoes. Highly silicic magmas tend to form lava domes (e.g. Soufriere) and the lavas being extruded from these volcanoes have viscosities in the order of 10^9 Pa·s, (Blake, 1990). Though not a common form of lava, alkali carbonatite lavas have viscosity ranges that vary depending on the nature of the magma intruding through the overlying carbonate system. The 1993 eruption of Oldoinyo Lengai in Tanzania was highly viscous (Dawson, Pinkerton, Pyle, & Nyamweru, 1994) compared with earlier eruptions from 1988 (Dawson, Pinkerton, Norton, & Pyle, 1990). The most common low viscosity lava is basaltic and it is the one whose flow is of most concern to hazard managers.

Typical approaches to predicting lava run-out distances and flow-speed have relied on either the bulk geochemical data of the lava composition in a bottom up approach to estimate viscosity, e.g. PyFLOWGO (O. Chevrel, Labroquère, Harris, & Rowland, 2017) or the effusion rate at the vent. Bulk geochemical data and melt vs. crystal percentages are not usually available in real time. Lava vent effusion rates do not account for the evolution of the flow as it moves down the channels, bifurcating, forming crusts and levees and cooling. As viscosity changes with temperature flow speed will vary as the flow moves away from the vent. To better understand the evolution of the flow in real time a better knowledge of the underlying rheology is required through developing benchmarked fluid dynamics codes and rheological appropriate models. (Cordonnier, Lev, & Garel, 2016; Dietterich, 2015)

Lava rheology determines how a lava will deform in response to stress, and lava viscosity is the resistive force within lava (the internal friction) that shapes its flow. Lava's viscosity varies with its composition, temperature, volatile content, (Lensky, Lyakhovsky, & Navon, 2002) and proportion of crystals and bubbles (Manga, Castro, Cashman, & Loewenberg, 1998). The study of the rheology of lava at the Earth's surface is important to make predictions about lava flow-direction (Griffiths, 2000), flow distance (Harris and Rowland, 2009), flow-rate (Melnik, 2016) and potentially its evolution below ground. (Ferlito et al., 2009)

The crucial question for hazard managers to avoid future disasters such as Mount Nyiragongo in the Congo (Favalli, et al. 2009) or the Eldfell eruption in Iceland, (Williams, 1973) is how to predict the area at risk from lava flows. Models like VolcFlow (Kelfoun, Vallejo Vargas, & Vargas, 2015), PyFLOWGO (O. Chevrel et al., 2017), Magflow (Negro, Fortuna, Herault, & Vicari, 2007) and Downflow (Favalli, Pareschi, Neri, & Isola, 2005) that predict lava flow paths require knowledge of the flow's properties which may evolve in time (Favalli et al., 2005). While many properties of the fluid are important in calculating velocity, viscosity is the crucial property for determining run out distances (Prakash & Cleary, 2011); as viscosity increases, flow speed decreases and potential run out distances also decrease.

Viscosity is difficult to directly measure in the field due to hazards and experimental challenges associated with high temperatures (M. O. Chevrel et al., 2018). Additionally, it is difficult to indirectly measure because of its interdependence on other properties such as temperature, which is highly temporally and spatially variable. Spatial variance in temperature is in part controlled by the morphology of the flow. For example, lava tubes are self-insulating and support high temperatures over long distances. Complex feedbacks exist between slope angle, flow rate, flow morphology and cooling rate as exhibited by the ability of insulating pāhoehoe flows to transition to ʻaʻā, drastically changing in cooling rate and viscosity. Lava flows can be monitored remotely for effusion rate, temperature and run out distance (M. R. Patrick, Kauahikaua, Orr, Davies, & Ramsey, 2016). Excellent attempts have also been made by Lev, Spiegelman, Wysocki, and Karson (2012) to determine lava rheology using video analysis in the laboratory.

Lava is a complex multiphase fluid and understanding its flow behaviour is not a trivial problem. To solve this problem it must be broken into many smaller, simpler components. This

research will tackle one component of the larger problem, by measuring the free surface velocity of an isothermal, homogenous single phase Newtonian fluid and using it to calculate its viscosity. How this will be achieved is set out in the following sections. Insights from this research will allow future work to consider other aspects and provide a full synthesis of the lava flow problem.

An introduction to viscosity

Viscosity is defined as the internal force per unit area of a fluid that resists flow. It was first described mathematically by Sir Isaac Newton circa 1700. Newton's law of viscosity relates the shear stress of adjacent fluid layers to the velocity gradients between them. This can be seen in Figure 1 as a fully developed laminar flow between two parallel plates. The bottom plate is fixed and the top plate is moving under a force, F (Pa·s). The shear stress (τ) is defined as the tangential force per unit area given by the relationship:

$$\tau = \mu \frac{\partial u}{\partial y} = \mu \frac{U}{h}$$

Where, μ is the dynamic viscosity of the fluid, $\frac{\partial u}{\partial y}$ is the shear rate ($\dot{\gamma}$) and U is the flow speed.

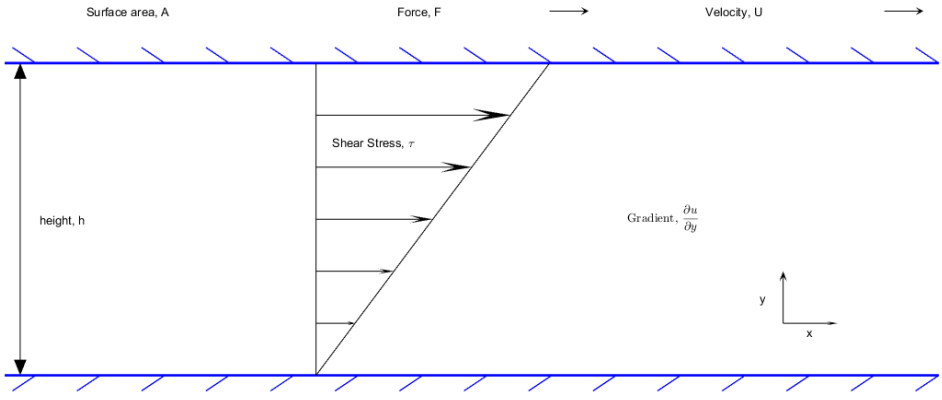

Figure 1. Fluid flow between two boundary plates (blue). Dynamic shear viscosity is the resistance to shearing stress. At $y = h, u = U$, at $y = 0, u = 0$. The velocity of each of the walls matches the velocity of the fluid, which is known as the 'no slip boundary' condition.

For Newtonian fluids, there is a linear relationship between shear stress, τ and shear rate γ̇, as seen in Figure 2 where Newtonian fluids plot as a straight line through the origin.

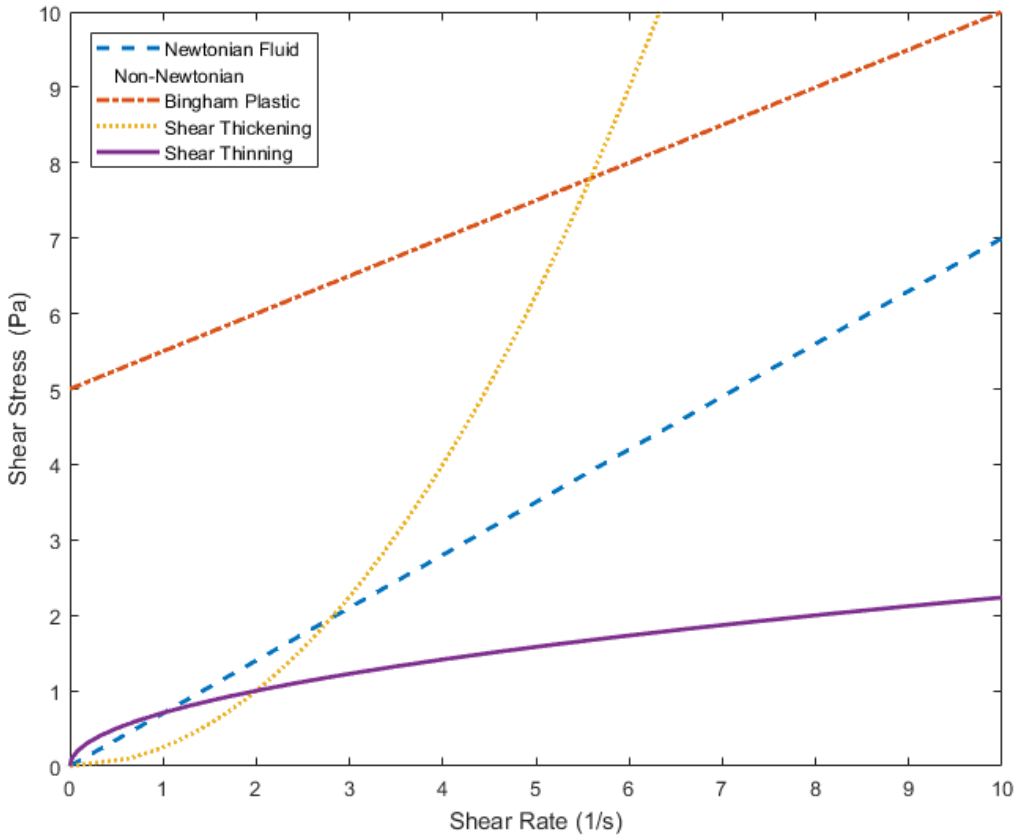

Figure 2. While Newtonian fluids have a linear relationship between shear rate and shear stress, non-Newtonian fluids do not. The ordinate at y = 0 for Bingham fluids is the yield stress that must be overcome for these fluids to flow.

When an elastic solid is subjected to stress it deforms until the stress is released at which point it returns to its original shape. By contrast, Newtonian liquids are not defined by their shape and when subjected to stress it is their viscosity that characterizes them. There are two different categories used to classify the response to stress on fluids, Newtonian and non-Newtonian (Figure 2). Non-Newtonian fluids can be further broken down into multiple subcategories depending on their relationship between shear stress and shear rate. For example, shear thinning fluids like some toothpastes and mayonnaise show a drop in viscosity as shear rate increases, (Roberts, Barnes, & Carew, 2001). Bingham fluids, like paint, require a minimum shear stress threshold to be overcome before they flow (Liu & Mei, 1990). Whereas, shear thickening fluids like “Oobleck” (cornflour and water) exhibit an increase in viscosity with increasing shear rate (Crawford et al., 2013). The viscoelastic non-Newtonian fluids are unique in that they exhibit both an elastic and viscous response to stress.

The viscosity velocity relationship

Viscosity affects the flow field and in some simple cases it is possible to find a direct relationship between the viscosity and the measured velocity. Viscosity is inversely proportional to velocity, and measuring velocity is much simpler than directly measuring viscosity. This is one of the simplifications made in this research, where the flow velocity is used to derive fluid's viscosity. Early attempts to quantify flow velocity were done photogrammetrically in the field by James et al. (2010) who used laser scanners and photographs collected over time and space intervals to generate time varying 3D topography. Flow velocity and volumetric flux were measured in this way. However, flow thickness could not be directly measured and had to be inferred from thermodynamic principles. James et al. (2011) went on to produce an updated stereoscopic method using multiple cameras to produce digital elevation models (DEMs) and derive viscosity from Jeffreys' equation (Jeffreys 1925):

$$U_{max}\frac{\rho g d^2 \sin\theta}{n\mu} \qquad \text{Eq. 1}$$

Where U_{max} is flow velocity, ρ is lava density, g is acceleration due to gravity, d is flow thickness, θ is topographic slope angle, n is a dimensionless constant and μ is the dynamic viscosity. This equation, however, is not suitable to describe non-Newtonian fluids as they do not follow Newton's law of viscosity which requires a linear relationship between stress and shear rate. To solve for velocity in non-Newtonian fluids the Navier-Stokes equations must be used, these equations will be discussed in detail in the next chapter. Jeffreys' equation also assumes that the geometry of the flow is a boundless flat plane, whereas real lava flows have levee walls and are temperature dependent. Takagi & Huppert (2010) looked at the effect of various channel morphologies on flow speed and their V channel results will be tested within this research.

There is still debate as to the conditions where basaltic lava flows can be approximated by Newtonian or Non-Newtonian flow rheology and some suggest it changes over the length of a flow from Newtonian to Bingham to even pseudo-plastic (Moore 1987), and others suggest lava flow lobes are considered to behave as Newtonian fluids deep inside the hot part of the flow and change to pseudo plastic flows out towards the cooler sub-crustal layers (O. Chevrel,

personal communication, September 4th, 2018). This research will investigate the behaviour of Newtonian fluids but develop a methodology that is extensible to non-Newtonian fluids.

The aim of this research is to therefore investigate the relationship between free surface flow speed and viscosity using velocity distributions on the surface of a flow spreading under gravity to predict viscosity in Newtonian and non-Newtonian fluids. If successful, this technique could be applied in the field on spreading and channel confined flows; two common geometries of active lava. This could lead to the rapid determination of viscosity of an advancing flow and help refine hazard models in areas likely to be impacted by lava flows. The V channel is a good, simple approximation of a levee-controlled-channel. Takagi and Huppert (2010) have already shown that the minor details of the channel shape are not as important as changes in the flux (flow rate per unit area) of lava flows.

Lava flow models

Determining the nature of lava rheology has always been a challenge. The volcanic environment where direct measurements can be made is extremely hazardous. Laboratory work with lava at around the required 1200°C to form basaltic lava is also challenging, though it has been undertaken. Farrell et al. (2018), at Syracuse in New York modelled coaxial strain in basalt lava crust, while Lev et al. (2012) modelled box channel flow of basaltic lava using velocimetry, and Giordano et al. (2004) at Hanover University did penetration tests to determine viscosity on trachytes. Few places like Hawaii's Kilauea volcano or Syracuse University and the University of Canterbury exist in the world where such work can be done and probably explains why so few non-analogue experiments have been performed. The role of analogues is therefore extremely important in determining the governing factors of lava flow while allowing for control of independent parameters in a cost effective and safe manner.

Early attempts to model lava flow behaviour started with Jeffreys' equation (Jeffreys, 1925). This equation assumed that lava flows were infinitely flat sheets of uniform thickness on an inclined plane, i.e. no boundary conditions. This equation also assumes a Newtonian fluid regime. When Shaw, Wright, Peck, and Okamura (1968) pushed a rotational viscometer into lava flows in Hawaii they discovered the flow they were analysing had a yield stress. The Jeffreys' equation was extended by Moore and Henry (1987) to include boundary conditions

and a Bingham rheology. Moore went on to discover that the behaviour of lava flows ranged from Newtonian near the vents to Bingham further along the flow and shear thinning closer to the toe.

Chevrel et al. (2018) tried to directly measure the rheology again with a rotational viscometer but due to equipment failure were unable to obtain the required data. They used a petrologic approach with crystal, bubble and textural data to calculate the viscosity. This is a common approach once this data is available, but this might take too long for hazard managers.

With the increase in computer processing power, numerical models have started to emerge that can simulate solutions to the Navier Stokes equations using finite element or finite volume methods. This technique will soon be combined with advances in computer vision and artificial intelligence to enable a stereoscopic image of an active lava flow to be captured, have its velocity field determined and then the viscosity derived from the Navier-Stokes equations. This work was pioneered by Lev, Spiegelman, Wysocki, and Karson (2012) and lava viscosities were calculated from video captured of a channelized lava flow. Their challenges with flow thickness and temperature measurements can be overcome, initially in the laboratory with more thermocouples and stereoscopic methods to derive flow thickness.

Existing fluid simulation models

Dietterich et al. (2015) have conveniently reviewed and benchmarked many of the computational fluid simulation methodologies. Dietterich et al. (2015) deploy four experimental benchmarks:

Benchmark A: Isothermal, isoviscous sloping flow
Benchmark B: Isothermal, isoviscous sloping flow into obstacles
Benchmark C: Cooling, isoviscous axisymmetric flow
Benchmark D: Cooling, solidifying sloping flow

In the first experiment, Benchmark A, golden syrup is poured down an inclined plane. In the second they place an obstacle in the flow path of the golden syrup. Benchmark C uses an isoviscous, cooling silicone oil and benchmark D uses molten basalt poured onto a sloping

surface of sand at a steady flux. The models predictions are compared to the experimentally observed results. The models examined include:

- OpenFOAM
- VolcFlow
- Flow3D
- MOLASSES
- COMSOL

OpenFOAM is a finite volume method (FVM) solver. It is similar to COMSOL, which uses finite element analysis (FEA), but OpenFOAM is open source software. VolcFlow is a 2D solver for isothermal Newtonian or Bingham fluids over a DEM. Flow-3D is another FVM solver that can also be applied over a DEM. Flow-3D is a fully commercialised product that is easier to use than the open source options but is also expensive and slow. MOLASSES uses cellular automation, a discrete model that allows cells to vary their values based upon their neighbour's values over time according to a set of rules.

Table 1. Normalised Root Mean Square Error (NRMSE) values for each model over each benchmark. Lower values are closer to predicted values. Table adapted from Dietterich, et al. (2015) Where X is streamwise, Y is spanwise, H is thickness, R is radius and T is temperature.

Model	BM-A X	BM-A Y	BM-A H	BM-A&B H	BM-C R	BM-C T	BM-D X	BM-D Y	BM-D H
OpenFOAM	2.6	6.95	28.72	6.62	1.53	0.17	6.34	7.27	22.53
FLOW-3D	6.59	11.33	7.46	15.53	6.36	0.09	4.86	10.1	12.48
VolcFlow	7.2	25.06	3.13	14.22	1.94	-	3.92	12.65	23.39
COMSOL	7.11	14.06	4.63	16.09	7.18	0.27	4.21	9.73	20.84
MOLASSES	8.3	3.99	8.56	11.6	0.56	-	21.02	38.48	6.15

While all models achieve a result within 10% (of the Normalised Root Mean Square Error, NRMSE) in cross slope propagation, only OpenFOAM achieved a similar result in down slope propagation as well. However, when we look at the summarized results in Table 1, across all the experimental parameters and models we see no clear pattern of one model outperforming the others. COMSOL does appear to have a consistent NRMSE across the measured variables in the experiment. Dietterich et al. (2015) concluded that model accuracy is largely dependent upon initial assumptions, and mesh construction.

One of the main strengths of COMSOL is that it can simplify complex 3D models into representative 2D problems that require significantly less computational effort to solve. Dietterich et al. (2015) observes the main drawback with this simplification approach in their experiments is that it omits the effect of temperature and viscosity in the vertical direction and thus lacks the ability to simulate behaviour of lava overtopping objects in its path. Dietterich et al. (2015) was unable to use this approach to reduce the computational complexity of a changing mesh as their flow developed around obstacles. In this study's proposed experiments, the flow is in a steady state and does not vary in the vertical direction and the mesh does not change as no obstacles are placed in the flow path. A simplified 2D representative cross section can be created to reduce computational load. If it was decided to include the cooling effects, crystal growth and crust development then OpenFOAM could be a more appropriate modelling solution as these parameters can be modelled in this software. However, the institutional experience and isothermal nature of the problem lends itself to COMSOL in this instance.

All these approaches are trying to solve the same governing equations for viscosity but some models use different fundamental assumptions. Costa and Macedonio (2005) built a numerical model that uses the shallow water approximation. This approach simplifies the equations when the horizontal scale of the flow is much greater than the vertical one. Therefore a limitation in this approach is that it does not allow for variances in viscosity across the flow thickness, a limitation that Castruccio, Rust, and Sparks (2014) justify in their model by discussing the aspect ratio of flow length to flow thickness. They conclude that if the flow is significantly long and the aspect ratio is not exceeded then a 2D model is sufficient in their Herschel-Bulkley flow model. The main limitation of their approach is they require an accurate estimate of the crystal fraction of the flow.

Building on the work of Miyamoto and Sasaki (2002, 2004) in their use of cellular automation to solve an analytical solution to Navier-Stokes, Prakash and Cleary (2011) have extended the approach using Smoothed Particle Hydrodynamics and three dimensional digital terrain models. Their extended model uses the full Navier-Stokes solution and a heat transfer model combined with realistic topography to calculate lava run out distances. These calculations are very computationally taxing and take several days to run. This approach was later reviewed by (Zago et al., 2018) and the code extended to be run on graphical processing units to reduce the

computation time. Zago et al. (2018) attempted to use the benchmarking tools developed by Cordonnier et al. (2016).

Cordonnier et al. (2016) led a workshop at Cities on Volcanoes 7 in 2012, to present a benchmark model for mass flow deposits in an attempt to better compare the efficacy of lava flow models. They have also reviewed several models against their benchmark including FLOWGO and MAGFLOW, as well as the aforementioned cellular automation models like VOLCFLOW and FLOW3D. The stochastic models use probabilistic distributions in place of unique values. As a consequence, these models excel at predicting flow paths and run out distances. These types of models are strongly reliant on DEMs to determine the flow paths and resulting gravity currents. A free surface velocity approach has no such requirement.

Table 2. Some of the models reviewed by (Cordonnier et al. 2016) with associated strengths and weaknesses.

Model	Fast	Emplacement	Includes Crystallization	Crustal Melting	Hazard Maps	Vertical Profile of Parameters
FLOWGO	yes	yes	yes			no
MAGFLOW	yes					no
VOLCFOW		yes				yes
FLOW3D		yes				yes
OPENFOAM				yes		yes
GPUSPH						numerical diffusion
NB3D						numerical diffusion
DOWNFLOW	yes				yes	no thickness, no temporal variation

GPUSPH and FLOWGO showed the most potential in being able to model most (23/25) of the required benchmark parameters. With the current ongoing development of PYFLOWGO the slope angle driving force limitation may be overcome soon (Chevrel et al., 2017).

Lava forms a crust as it cools and this crust insulates the underlying flow. As the crust freezes it records the buckling induced by the visco-plastic strain within the flow. Farrell, Karson, Soldati, and Wysocki (2018) have found a rheological relationship between the ropy pāhoehoe textures of the crust and the underlying flow viscosity. This is important because often the flow is hidden beneath the crust and a fully developed model would benefit from incorporating and extending upon these findings. A limitation of this method would be when the crust separates from the underlying flow as occurs in lava tubes (Harris & Rowland, 2015).

Lev et al. (2012) developed a method to use video and finite element analysis to determine rheological properties of lava. Their method used optical flow tracking to determine the velocity field from the movement of bright pixels. The method proposed here will make several improvements by using trackable markers to determine the velocity field, allowing accuracy to be improved. Lev et al. (2012) used a flat sheet flow and a derivative of the Jeffreys' equation for finite element analysis in one set of experiments as well as a U shaped channel and a steady state flow in another. Here, the V channel morphology is used with the Takagi and Huppert (2007) steady state solution for Newtonian flow and the Navier-Stokes equation in COMSOL. Lev et al. (2012) had to estimate flow thickness after cooling, whereas we will use a barrier at the head of the V channel that limits the height of the free surface flow to define our free surface height. Lev et al. (2012) solves the Stokes equations using ELMER, an open source finite element package, whereas we will use COMSOL to model our V channel and determine velocity of the free surface.

Research purpose and objectives

With most fluids viscosity affects the flow field and there is therefore an implicit relationship between fluid viscosity and observed flow velocity (Drazin & Riley, 2006). The purpose of this research is to use analogue fluids to explore this relationship within known geometries. This will be done by comparing experimental results with mathematical models.

Questions and aims of this research (aims are in italics)

1. How can the magma rheology be deconstructed into a smaller, simpler yet realistic system? *Determine with: Dimensional analysis and Buckingham Pi theory to identify the determining variables.*
2. What are the governing equations that describe the system and can it be modelled mathematically and solved? *Solve with: COMSOL, Navier-Stokes and continuity equations.*
3. Can experiments be conducted in a controlled manner and produce reliable, repeatable and useful data? *Identify with pilot study.*

4. How can the data be analysed, interpreted and compared with the model? *Compare with: Takagi Huppert analytical equations* (Takagi & Huppert, 2007).
5. How does the experimental data compare with the mathematical model? *Compare with statistics.*
6. What is the value of the research outcome*? Discussion of the relevance and utility of these results in the future of lava flow modelling.*

This research will share many of the same techniques as previous work done by Lev et al. (2012), but it will differentiate itself by using a V channel morphology, the Navier-Stokes equations to solve for the flow and indirectly identify the fluid viscosity, a flow barrier to aid steady state development, and trackable markers to increase accuracy in determining free surface velocity. If successful, these flow markers will extend the reliability of the measured velocity significantly over Lev's work.

Chapter Two: Methods

The research goal was to create a mathematical computer model to represent the flow and allow the indirect identification of the viscosity of a fluid flowing down an open V channel. This chapter discusses the two approaches used to complete this.

The first section outlines how the mathematical model was implemented for the computational solution using the finite element analysis (FEA) software COMSOL Multiphysics 5.2 (COMSOL) to simulate the flow of a fluid down a V channel and the mathematical theory behind the model.

The second section outlines the dimensional analysis and Buckingham Pi theory used to design the physical experiments. This technique was used to explore the relationships between the parameters of the study and to design the experimental procedures. In the experimental approach, fluids of known physical properties were released under gravity down an inclined V channel in order to determine their rheology from the free surface velocity of their flow. The experimental setup is presented and it is shown how the flowing free surface was captured with video to determine the flow's velocity field. The analytical solution (Takagi & Huppert, 2007) is then calculated and validated against the COMSOL model.

2.1 Computational solution

Several suitable software packages exist to model fluid flow as discussed in the background section. COMSOL was chosen because it is available and it performed as well as the other modelling packages. It also has an easier learning curve and more intuitive interface than the open source products like OpenFOAM.

2.1.1 Navier-Stokes

The relationships between a fluid's free surface velocity, density, pressure, temperature and its viscosity are described in the coupled partial differential equations derived in the late 1800s by the French mathematician Claude-Louis Navier and the English mathematician George Gabriel Stokes. This equation models the flow of any fluid, e.g. air, ice, water or lava. The Navier-

Stokes equations are generally too difficult to solve analytically and the existence and uniqueness of solutions is an open Millennium Prize problem (Fefferman, n.d.). Solution approximations are derived using computational fluid dynamics (CFD) software and discretisation techniques such as finite element analysis. This is the technique of dividing large, complex systems into smaller, simpler parts (finite elements) and these parts are then used to model and solve the complex system in turn.

The Navier Stokes equations describe the conservation of mass, momentum and energy with four independent coordinates of space, (x, y, z) and time, (t). There are six dependent variables: pressure, (p), density, (ρ), temperature (T) and a velocity vector ($\vec{\boldsymbol{u}} = u + v + w$). The dependent variables are functions of the independent variables.

The three dimensional unsteady form of the Navier Stokes equation has the form:

Continuity
$$\frac{\partial \rho}{\partial t} + \frac{\partial (\rho u)}{\partial x} + \frac{\partial (\rho v)}{\partial y} + \frac{\partial (\rho w)}{\partial z} = 0 \qquad \textbf{Eq. 2}$$

X Momentum
$$\frac{\partial (\rho u)}{\partial t} + \frac{\partial (\rho u^2)}{\partial x} + \frac{\partial (\rho uv)}{\partial y} + \frac{\partial (\rho uw)}{\partial z} = -\frac{\partial p}{\partial x} + \left[\frac{\partial \bar{\bar{\tau}}_{xx}}{\partial x} + \frac{\partial \bar{\bar{\tau}}_{xy}}{\partial y} + \frac{\partial \bar{\bar{\tau}}_{xz}}{\partial z}\right] \qquad \textbf{Eq. 3}$$

Y Momentum
$$\frac{\partial (\rho v)}{\partial t} + \frac{\partial (\rho uv)}{\partial x} + \frac{\partial (\rho v^2)}{\partial y} + \frac{\partial (\rho vw)}{\partial z} = -\frac{\partial p}{\partial y} + \left[\frac{\partial \bar{\bar{\tau}}_{xy}}{\partial x} + \frac{\partial \bar{\bar{\tau}}_{yy}}{\partial y} + \frac{\partial \bar{\bar{\tau}}_{yz}}{\partial z}\right] \qquad \textbf{Eq. 4}$$

Z Momentum
$$\frac{\partial (\rho w)}{\partial t} + \frac{\partial (\rho uw)}{\partial x} + \frac{\partial (\rho vw)}{\partial y} + \frac{\partial (\rho w^2)}{\partial z} = -\frac{\partial p}{\partial z} + \left[\frac{\partial \bar{\bar{\tau}}_{xz}}{\partial x} + \frac{\partial \bar{\bar{\tau}}_{yz}}{\partial y} + \frac{\partial \bar{\bar{\tau}}_{zz}}{\partial z}\right] \qquad \textbf{Eq. 5}$$

Energy

$$\frac{\partial(E_T)}{\partial t}+\frac{\partial(uE_T)}{\partial x}+\frac{\partial(vE_T)}{\partial y}+\frac{\partial(wE_T)}{\partial z} = -\frac{\partial(\rho u)}{\partial x}-\frac{\partial(\rho v)}{\partial y}-\frac{\partial(\rho w)}{\partial z} - \frac{1}{Re_f Pr_f}\left[\frac{\partial \vec{q}_x}{\partial x}+\frac{\partial \vec{q}_y}{\partial y}+\frac{\partial \vec{q}_z}{\partial z}\right] \quad \textbf{Eq. 6}$$

Where,

- E_T is the total energy
- $\bar{\bar{\tau}}$ is a nine component stress tensor created by multiplying the three component vectors such that each element of the stress tensor is a second order derivative of the velocity components
- $\vec{q}$ is the heat flux
- Re is the Reynolds number
- Pr is the Prandtl number

The left side of the momentum equations represent the convection terms and those on the right side represent the diffusion and source terms. Diffusion is related to the stress tensor and viscosity. Since all variables occur in all the equations (**Eq. 2, Eq. 3, Eq. 4, Eq. 5, Eq. 6**) they are a coupled system of equations and all have to be solved simultaneously. These equations can be solved using COMSOL which uses Navier-Stokes written below in its condensed form:

$$\rho\left(\frac{\partial \boldsymbol{u}}{\partial t}+\boldsymbol{u}\cdot\nabla\boldsymbol{u}\right) = -\nabla p + \nabla\cdot\left(\mu(\nabla\boldsymbol{u}+(\nabla\boldsymbol{u})^{\mathrm{T}}) - \frac{2}{3}\mu(\nabla\cdot\boldsymbol{u})\boldsymbol{I}\right)+\boldsymbol{F} \quad \textbf{Eq. 7}$$

Where $\nabla\cdot\boldsymbol{u}$ notation is shorthand for:

$$\nabla\cdot\boldsymbol{u} = \frac{\partial u}{\partial x}+\frac{\partial v}{\partial y}+\frac{dw}{dz}$$

This equation (**Eq. 7**) is equivalent to Newton's second law of motion ($F = ma$) and applies to Newtonian fluids.

- The left hand side is the mass and acceleration, where:

  - ρ is density or mass per unit of volume.
  - $\left(\frac{\partial \boldsymbol{u}}{\partial t}+\boldsymbol{u}\cdot\nabla\boldsymbol{u}\right)$ is acceleration or the rate of velocity change per unit time, (t) in any given direction.

- The right hand side are the forces, where:

  - $-\nabla p$ is a pressure gradient within the fluid.
  - $\nabla \cdot \left(\mu(\nabla \boldsymbol{u} + (\nabla \boldsymbol{u})^{\mathrm{T}}) - \frac{2}{3}\mu(\nabla \cdot \boldsymbol{u})\boldsymbol{I}\right)$ is the stress from internal forces within the fluid, μ is the dynamic viscosity or flow resistance of the fluid, and T is the transpose operator
  - and F is the external force acting on the fluid e.g. gravity

The fluids used in these experiments are incompressible so the compressible component is removed,

$-2/3\ \mu(\nabla \cdot \mathrm{u})\mathrm{I}$ leaving:

$$\rho(\boldsymbol{u} \cdot \nabla)\boldsymbol{u} = \nabla \cdot [-pl + \cdot \mu(\nabla \boldsymbol{u} + (\nabla \boldsymbol{u})^{\mathrm{T}})] + \boldsymbol{F} \qquad \textbf{Eq. 8}$$

This equation is used with the continuity equation that represents conservation of mass (i.e. No mass is created or destroyed and in the incompressible case, the density is not changed within the system):

$$\frac{\partial \rho}{\partial t} + \nabla \cdot (\rho \boldsymbol{u}) = 0$$

To extend the model to allow for non-Newtonian fluids, a power law can be used:

$$\mu = k(\dot{\gamma})^{n-1} \qquad \textbf{Eq. 9}$$

Where

$\dot{\gamma}$ is the shear rate, (s^{-1})

k is the flow consistency index, (Pa.s).

n is the flow behaviour index, (dimensionless) indicates the degree of non-Newtonian behaviour of the fluid.

There are several different power law models that can be used to describe non-Newtonian behaviour, depending on whether the fluid under consideration has (1) a yield stress,(Bingham fluids), or (2) decreases viscosity with increasing shear strain (shear thinning), or (3) decreases viscosity with increasing shear strain associated with high shear strain (pseudo plastic fluids). To be able to use the Navier-Stokes solver in COMSOL, however, a model must first be built in the software that embodies the geometric and physical properties of the V-channel used in the experiments.

2.1.2 COMSOL Multiphysics model

As our interest is in the velocity of the fluid under steady state flow, only a small part of the experimental domain needs to be represented in the model since if the flow is fully developed it is invariant in the flow direction. The inlet reservoir that contains the fluid does not need to be included, nor does the outlet or collection reservoir. In CFD only the fluid needs to be modelled and the actual channel itself can be subtracted from the geometry. The fluid is discretized into finite elements and the Navier-Stokes equations are solved for each element. The workflow used in building the COMSOL is as follows:

i. Open a new COMSOL project and add the required physics packages
ii. Build a 2D slice of the model's geometry
iii. Extrude the slice to create a 3D model
iv. Define the boundary conditions
v. Build the mesh
vi. Enter the parameters and variables used to solve the equations
vii. Define the coordinate systems
viii. Visualize the results

(i) Physics packages

A new 3D space project was created using the model wizard. For the physics package, the laminar flow single phase fluid (spf) interface was chosen because the Reynolds numbers in lava flows are lower than the critical value for turbulence (~2000 in a pipe flow) (Avila et al., 2011) and a stationary study was selected as the field variables were not changing with time (steady state flow).

(ii) Geometry

In COMSOL the geometry of the model was built to the same scale as the apparatus in the laboratory to replicate the experimental configuration as closely as possible. After the physics package selection, the next step in creating the COMSOL model was to build the geometry of the flowing fluid (see Figure 3). The model is simplified because the domain is the fluid flow, not the V shaped steel channel used in the experiments.

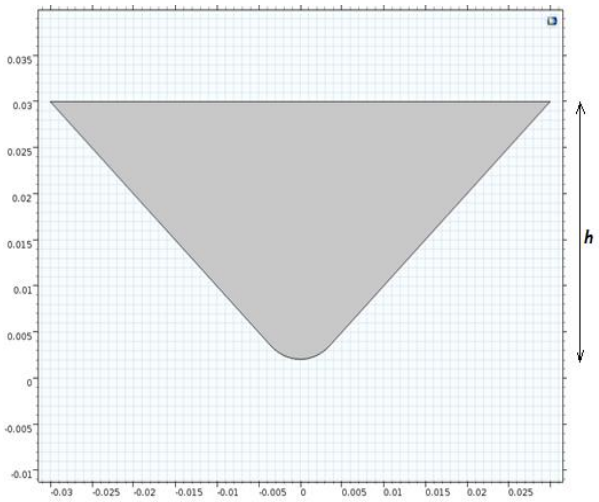

Figure 3. The plane geometry of the V channel built in COMSOL. The bottom of the model $(x, y) = (0,0)$ is rounded the same way the physical experimental V channel is. The flow thickness is a input variable that defines the shape of the model and in this example the flow thickness h, is 30 mm.

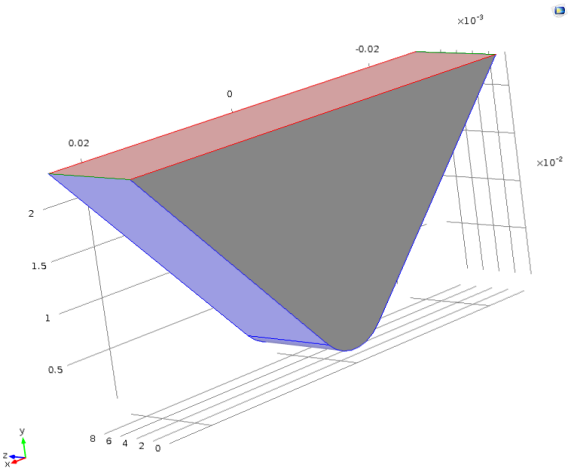

Figure 4. 3D model of the V channel where the 2D shape has been extruded along the z axis. The blue surfaces are no-slip boundary surfaces and the pink surface is a free surface between the fluid (grey) and the air (not shown). A periodic boundary condition is applied to the grey surface for flow down the channel.

(iii) 2D to 3D

The model is then extruded in the z direction (normal to the page in Figure 4) to create a 3D slice. The geometric model does not need to have the same length as the experimental V-channel because the flow will tend towards a fully-developed flow in the streamwise direction, z. The COMSOL model can thus be simplified this way to reduce computation time, without affecting the result.

(iv) Boundary conditions

No-slip boundary conditions are set on the two blue coloured faces of the V-channel, and a free surface is defined on the pink surface of the flow with a slip condition (Figure 4).
A periodic flow condition was specified on the grey faces (Figure 4) where,

$$u_{\text{source}} = u_{\text{destination}} \text{ and } P_{\text{source}} = P_{\text{destination}}$$

The volume force equation (**Eq. 7**) is used to make the fluid flow and defined as:

$$F = \begin{cases} x = 0 \\ y = -f_y \\ z = f_z \end{cases}$$

Where, $f_y = \rho g \cos(\beta)$, $f_z = \rho g \sin(\beta)$ in $\mathrm{N/m^3}$ and β is the inclination angle of the channel.

(v) Building the mesh

The model's mesh was built in COMSOL using the pre-set template for '*fluid dynamics'* with the '*element size settings'* shown in Table 3. A triangular 'Normal' mesh was applied and swept back so that the z axis has one element of depth (Figure 5), to reduce the computational load.

Table 3. Mesh variables.

Element Size parameters	Range	Final Value
Predefined	Extremely Fine, Normal, Extremely Coarse	Normal
Degrees of freedom to solve	144120, 5896, 352	5896
Arbitrary mesh level	1, 2, 3	2
Maximum element size	2.08E-4, 0.00107, 0.00527	0.00107
Minimum element size	3.19E-6, 3.19E-4, 0.00112	3.19E-04
Maximum element growth rate	1.05, 1.15, 1.4	1.15
Curvature factor	0.2, 0.6, 1	0.6
Resolution of narrow regions	1, 0.7, 0.3	0.7
Solution time (s)	153, 7, 1	7

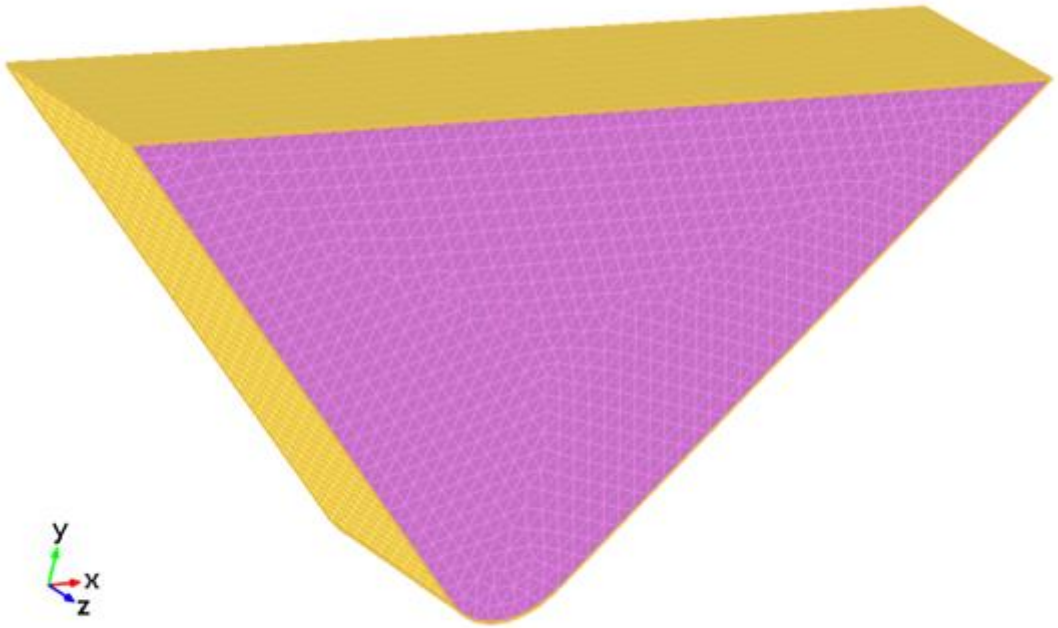

Figure 5. Mesh applied to the geometry.

2.1.2.1 Mesh convergence study

A mesh convergence study was undertaken to determine the optimum mesh settings. This is a process of resolving the model with finer and finer element sizes and comparing the results between the different meshes. This was done using a parametric sweep of the element size parameters within the range of the COMSOL pre-set values ‘extremely fine’, ‘normal’ and ‘extremely coarse’ and a monotonic arbitrary value. It can be seen in Figure 6 that the solution has converged between coarse and normal and there is very little observable difference between normal and extremely fine. This means the mesh can safely be calibrated for normal and not put an undue computational load on the software to derive the answer.

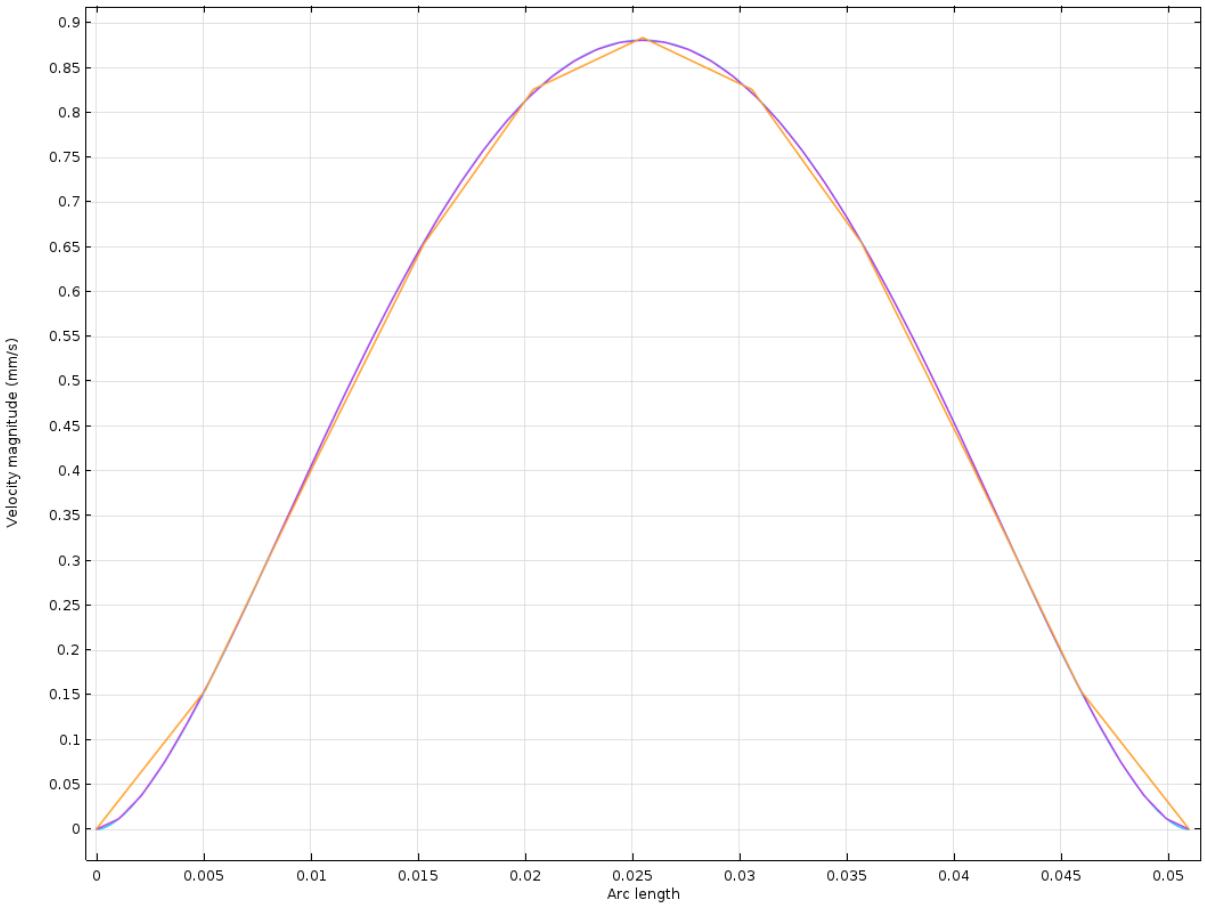

Figure 6. The mesh convergence of the three plots of different mesh sizes, orange is 'coarse', pink is 'normal' and cyan is 'extremely fine'.

(vi) Properties and variables

Table 4. Fluid properties used in the COMSOL V channel model. The body force, F (N/m^3) is derived by multiplying g by the scalars, $\sin(\beta)$ and $\cos(\beta)$, where β is the inclination angle of the flow and ρ, the density of the fluid.

	Name	Expression	Unit
Gravity, g	g	9.81	ms^2
Density, ρ	rho	1430	Kg/m^3
Body force, F_y	fy	rho*g_const*cos(b)	N/m^3
Inclination angle, β	b	10/180 * pi	
Dynamic viscosity, μ or η	mu	nu * rho	kg/ms
Kinematic viscosity, ν	nu	0.185	m^2/s
Flow depth, h	L	height	
Experiment number	exp	1	
Body force, F_z	fz	rho*g_const*sin(b)	N/m^3

In COMSOL, materials were defined as global variables with the properties of the experimental fluids and could be changed independently for each individual experiment.

(vii) Coordinate Systems

The coordinate system is defined as shown in Figure 7 with the velocity field $\vec{u}$ (x, y, z) set initially to $0\ \mathrm{m/s}$ and pressure to 0 Pa. The free surface flow height was, $h = 30$ mm. The standard flow rate Q, was overridden because the Navier-Stokes equations with a prescribed gravity force is used instead. The model's dependent variables were set to physics controlled.

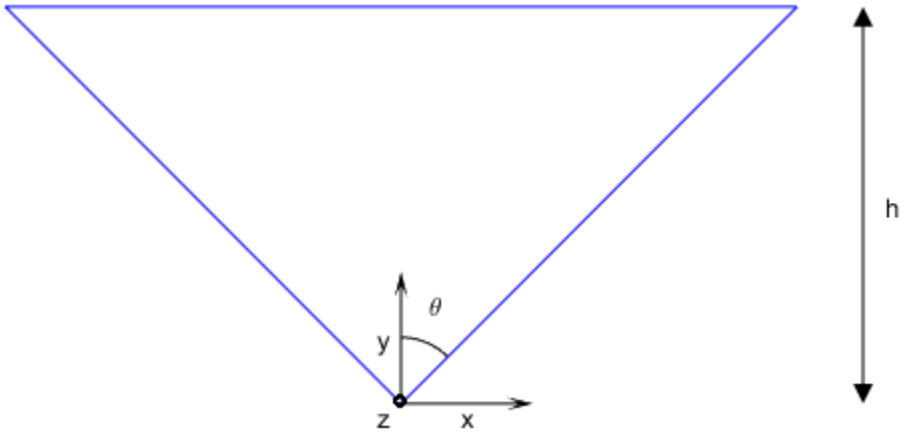

Figure 7. A V-channel cross section in the (x,y,z) coordinate space where x is cross-channel, y is perpendicular to the inclination angle, and z is in the streamwise direction along the channel.

The model is then complete and ready to solve for velocity using the parameters specified in (vi) above. This model was used to calculate the velocity field, given a viscosity derived from the experimental data. The resulting COMSOL velocity can then be compared with the experimentally observed velocity measured during the experiments.

2.2 Physical experiments

2.2.1 Dimensional analysis

To see how different parameters affect the model's behaviour, individual parameters were isolated and varied independently during experiments. The goal is to vary the parameters as independently as possible. Dimensionless groups are used to identify the relationships between the parameters. Buckingham Pi theory was used to identify the relevant dimensionless groups. To identify the parameters that are relevant in the experiments, the natural systems that the experiments emulate must be examined. In consideration of a lava flow moving down a gravity slope the dependent variables to be measured are first identified, which are flow velocity u and dynamic viscosity μ. Then the independent variables to be controlled are identified. Density ρ, flow thickness h, gravity g, and slope angle β, of which the latter acts as a scalar multiplier against gravity so can be ignored during dimensional analysis. There are three independent variables, but only two that can be practically varied: flow thickness and density. The effects of surface tension are ignored as the volumes (>1L) being used are sufficiently large that surface tension is proportionally negligible.

Table 5. Physical quantities relevant to fluids flowing down a slope under gravity. Slope angle, β is dimensionless.

	Flow height h (m)	***Density*** $\rho\left(\frac{kg}{m^3}\right)$	***Gravity*** $g\left(\frac{m}{s^2}\right)$	***Viscosity*** μ (Pa·s)	***Velocity*** $u\left(\frac{m}{s}\right)$
Mass (kg) [M]	*0*	*1*	*0*	*1*	*0*
Length (m) [L]	*1*	*-3*	*1*	*-1*	*1*
Time (s) [T]	*0*	*0*	*-2*	*-1*	*-1*

From Table 5, there is a relationship where velocity is proportional to:

$$u \propto \frac{\rho g h^2}{\mu} \qquad \textbf{Eq. 10}$$

Which has the dimensionless form:

$$[L][T]^{-1} \propto [M][L]^{-3}\,[L][T]^{-2}\,[\mathrm{L}]\,/\,[\mathrm{M}][L]^{-1}[T]^{-1}$$

This is now dimensionally correct and if the dimensionless inclination angle, (β) is reinstated it resembles Jeffrey's equation (Jeffreys, 1925). Where $u_{max}(y = h)$ from the coordinate system shown in Figure 1.

$$u_{max} = \frac{\rho g \sin(\beta) h^2}{\mu}$$

Jeffrey's equation describes a flow moving down an inclined rectangular plane with no side walls. In these experiments, however, the flow is moving down a V-channel of the form shown in Figure 7. So Jeffrey's equation is not suitable in these experiments.

2.2.2 Analytical solution

Fortunately, an analytical solution to the Naiver-Stokes equation has already been derived by Takagi and Huppert (2007), that describes an incompressible Newtonian fluid flowing through

a V-shaped confining channel under gravity. The velocity in the streamwise direction is defined as

$$u = \sum_{i=0}^{\infty}\sum_{j=0}^{\infty} a_{ij}\cos(\lambda_i X)\cos(\lambda_j Y) \qquad \textbf{Eq. 11}$$

where λ_i, λ_j are the scalar coefficients:

$$\lambda_i = \pi\left(\frac{1}{2}+i\right), \lambda_j = \pi\left(\frac{1}{2}+j\right), \quad i \in \mathbb{Z}$$

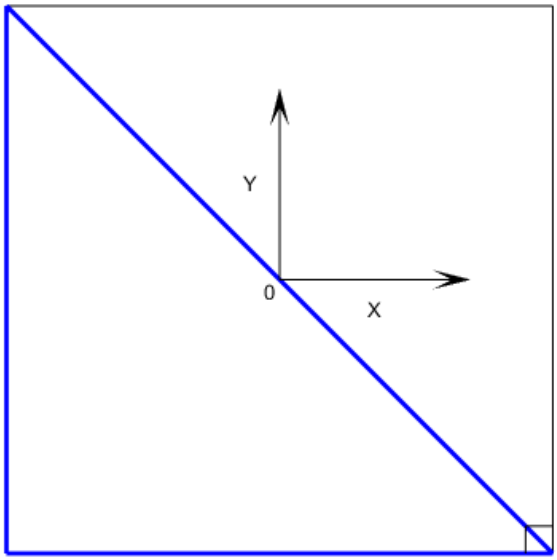

Figure 8. Transformed coordinates X, Y where the bold line represents the V-channel.

X and Y are the transformed coordinates from Figure 8:

$$X = \frac{1}{h}\left(y + \frac{x}{m'}\right) - 1$$

$$Y = \frac{1}{h}\left(y - \frac{x}{m'}\right) - 1$$

Where h is defined as the flow thickness and $m' = \tan(\theta)$ where θ is half the angle of the V channel angle as shown in Figure 7.

The a_{ij} components are evaluated thus,

$$a_{ij} = \frac{(-1)^{i+j} 4 M m'^2 h^2}{\left(1+m'^2\right)\lambda_i\lambda_j\left(\lambda_i^2 + \lambda_j^2\right)} \qquad \textbf{Eq. 12}$$

Where M is a parameter dependent on the inclination angle of the V channel,

$$M = \frac{g}{\nu}\sin\beta \text{ with } \beta \neq 0 \qquad \textbf{Eq. 13}$$

Where ν is the kinematic viscosity of the fluid. The requirement that $\beta \neq 0$ limits the size of the inclination angle such that the flow is due to gravitational forces down-slope rather than the slope of the free surface of the flow itself. This is mathematically expressed as, $|\partial h/\partial z| \ll \tan\beta$ (Takagi & Huppert, 2010).

The volumetric flow rate is defined as:

$$Q = KMh^4 \qquad \textbf{Eq. 14}$$

K is a scalar constant that depends on the angle θ:

$$\mathrm{K} \approx \frac{0.137\mathrm{m}^3}{(1 + \mathrm{m}^2)}$$

Two boundary conditions exist for this flow. It is assumed that there is a no-slip boundary on the walls of the channel and that tangential stress is zero on the free surface, y = h.

2.2.3 Scaling

In order to determine how the experiments approximate natural lava flows, it is important to examine the forces that are contained within the parameter space. There exists a stress σ_1, such that:

$$\sigma_1 \propto \rho gh$$

The units of stress, Pa, in dimensionless form are $ML^{-1}T^{-2}$. This stress is the volume force as described previously (**Eq. 7**).

It is possible to find another stress expression if viscosity is divided by time $\frac{\mathrm{Pa.s}}{\mathrm{s}}$, it has the same units as stress:

$$\frac{[\mu]}{[t]} = \frac{ML^{-1}T^{-1}}{T} = ML^{-1}T^{-2} = \text{Pa} \qquad \textbf{Eq. 15}$$

If flow velocity u is divided by flow thickness h:

$$\frac{[u]}{[h]} = \frac{L}{LT^1} = T^{-1} \qquad \textbf{Eq. 16}$$

Therefore dividing equation **Eq. 15** by **Eq. 16** reveals another stress:

$$\sigma_2 \propto \frac{[\mu][u]}{[h]} = \frac{ML^{-1}T^{-1}LT^{-1}}{L} = \frac{M}{LT^2}$$

A further stress expression can be derived from:

$$\sigma_3 \propto [u]^2[\rho] = \frac{L^2M}{T^2L^3} = \frac{M}{LT^2}$$

Comparing the ratio of these stresses.

$$\Pi_1 = \frac{\sigma_3}{\sigma_2} = \frac{\rho uh}{\mu}, \quad \Pi_2 = \frac{\sigma_1}{\sigma_2} = \frac{\rho gh^2}{\mu u}, \quad \Pi_3 = \frac{\sigma_1}{\sigma_3} = \frac{u^2}{gh}$$

Which reveals Π_1 is the Reynolds number, Π_2 is the Bond number and Π_3 is the Froude number.

2.2.4 Buckingham Pi theory

In order to correctly scale the experiments to a size that has similar rheological properties to natural lava flows and could fit in a laboratory, the dependent parameters have the greatest influences on flow velocity needed to be identified. Dimensionless groups are useful in highlighting key relationships between dependent variables.

To determine the dimensionless groups that govern the physical parameters relevant to these lava rheology experiments Buckingham Pi theory was used. This technique identifies the

dimensionless groups that govern this system. Buckingham Pi theory states that if there is a physically meaningful relationship among n-dimensional parameters (P_n) with k independent dimensions:

$$G(P_1, P_2 \dots P_n) = 0$$

Then these parameters can be combined into $n - k$ independent dimensionless parameters, (Π)

$$f(\Pi_1, \Pi_2 \dots \Pi_{n-k}) = 0$$

There are $n = 5\ (\rho, g, h, \mu, u)$ governing parameters which include $k = 3$ dimensions (M, L, T). Therefore the system can be described with $n - k = 2$ independent dimensionless groups.

$$\Pi_1 = h^a \rho^b g^c u^d$$

$$[\Pi_1] = L^a \ M^b L^{-3b} \ L^c T^{-2c} \ L^d T^{-d}$$

Grouping by M, L and T and since the exponents of each group must sum to zero:

For M: $b = 0$

For L: $a + c + d = 0$

For T: $-2c - d = 0$

Ignoring the case of $b = 0$, there are a set of 2 simultaneous equations with 3 unknowns. While there is no unique solution to these equations an arbitrary set of solutions that satisfy them can be found.

Let $a = n$, it follows that $b = 0, c = n, d = -2n, \quad n \in \mathbb{Z}$

Therefore,

$$\Pi_4 = h^1 \rho^0 g^1 u^{-2}$$

$$\Pi_4 = \frac{hg}{u^2}$$

Which can be rewritten as the Froude number (F_r), a dimensionless number that relates inertia to gravitational forces.

$$Fr = \frac{u}{\sqrt{hg}} \qquad \textbf{Eq. 17}$$

For the second Π group using μ

$$\Pi_5 = h^a \rho^b g^c \mu^d$$

$$[\Pi_5] = L^a \ M^b L^{-3b} \ L^c T^{-2c} \ M^d L^{-d} T^{-d}$$

Grouping by M, L and T and since the exponents of each group must sum to zero:

For M: $$b + d = 0$$

For L: $$a - 3b + c - d = 0$$

For T: $$-2c - d \ = 0$$

This yields a set of 3 simultaneous equations with 4 unknowns for which there exists an integer solution in terms of a.

$$b = \frac{2a}{3}, c = \frac{a}{3}, d = -\frac{2a}{3}$$

Which can be simplified by letting a = 3,

$$a = 3, b = 2, c = 1, d = -2$$

Therefore Π_2 is:

$$\Pi_5 = h^3 \rho^2 g^1 \mu^{-2}$$

$$\Pi_5 = \frac{h^3 \rho^2 g}{\mu^2}$$

This can be rewritten as the Archimedes number, (N_f) and is otherwise known as the inverse viscosity. This represents the ratio of buoyancy forces to inertial forces:

$$N_f = \frac{\rho\sqrt{gh^3}}{\mu} \qquad \textbf{Eq. 18}$$

This can be multiplied by the Froude number to produce another dimensionless group.

$$N_f F_r = \frac{\rho\sqrt{gh^3}}{\mu}\frac{u}{\sqrt{hg}} = \frac{\rho u h}{\mu}$$

Which is the Reynolds number, R_e

$$R_e = \frac{\rho u h}{\mu} \qquad \textbf{Eq. 19}$$

The system can now be described with three dimensionless groups:

$$F_r = \frac{u}{\sqrt{hg}}, \qquad N_f = \frac{\rho\sqrt{gh^3}}{\mu}, \qquad R_e = \frac{\rho u h}{\mu}$$

The Reynolds number is the balance of the inertial forces $\rho u h$, to the viscous forces μ. A high Reynolds number ($\approx Re > 2000$) indicates a turbulent flow and a lower Reynolds number represents a viscous dominated flow.

Table 6. Properties of lava analogues compared to natural in situ lava flows.

Fluid/Unit	$\boldsymbol{h}$ **m**	$\boldsymbol{\rho}$ **kg/ m^3**	$\boldsymbol{g}$ **m/ s^2**	$\boldsymbol{\mu}$ **Pa · s**	$\boldsymbol{u}$ **m/s**	N_f	$\boldsymbol{F_r}$	$\boldsymbol{R_e}$
Golden Syrup	0.0315	1430	9.81	55	0.0045	0.4553	0.0081	0.0037
Carbopol® 980	0.03	1029	9.81	137	0.052	0.7	0.096	0.012
Kilauea (1974) [1]	2.6	905	9.81	110	8.25	108	1.63	176.5
Etna (1983) [2]	4.5	1630	9.81	1700	30	44	4.52	200
Etna (2001)	1.35	2500	9.81	1700	0.55	298	0.15	1.1
Mauna Loa[3]	5	2000	9.81	2600	1.55	1374	0.22	5.96
Mauna Loa (1984) [3]	4	1000	9.81	1164	5.3	734	0.85	18.21
Mauna Loa (1984) [3]	8	2400	9.81	2000	0.3	465	0.03	0.04
Mauna Loa (1984) [3]	6	1700	9.81	100	1	919	0.13	1.41

In order to determine whether the analogue fluids would behave similarly to their natural counterparts, the physical properties of both systems are compared. Table 6 is a list from a

[1]Harris & Rowland, 2015, [2]Dawson, Pinkerton, Norton, & Pyle, 1990, [3]Moore 1984

literature review of approximate values from natural systems alongside the fluid analogues. It can be seen that the Mauna Loa flows cover a range of Re and Fr numbers that the Golden Syrup and Carbopol® sit within.

The experiments are designed to vary the variables, h, ρ, g, μ and u. Here, we do not alter gravity. Viscosity and density can be changed by using different fluids. Velocity can be differed by changing the inclination angle. There is also limited ability to alter the flow thickness by changing the fluids flow rate, Q. There are, therefore, n = 5 independent quantities and to conduct m = 5 different values for each variable would require $m^n = 5^5 = 3125$ experiments. Clearly, the parameter space is important. Removing gravity brings this number down to 625 experiments. To reduce this number further the sensitivity of the system to each parameter must be considered.

From the dimensionless groups identified using Buckingham Pi theory, the Froude number is significantly dependent on velocity whereas the Reynolds number is dependent on dynamic viscosity. Since gravity is the dominant force in this flow regime, the Froude number should be the most significant. The Froude number can be varied by changing the flow height or flow velocity. Therefore, the sensitivity of the free surface velocity to the free surface height, h, and the inclination angle (β) is investigated. This means that the aim is for $2^5 = 32$ experiments, a more manageable number than 625.

2.2.5 Parametric test

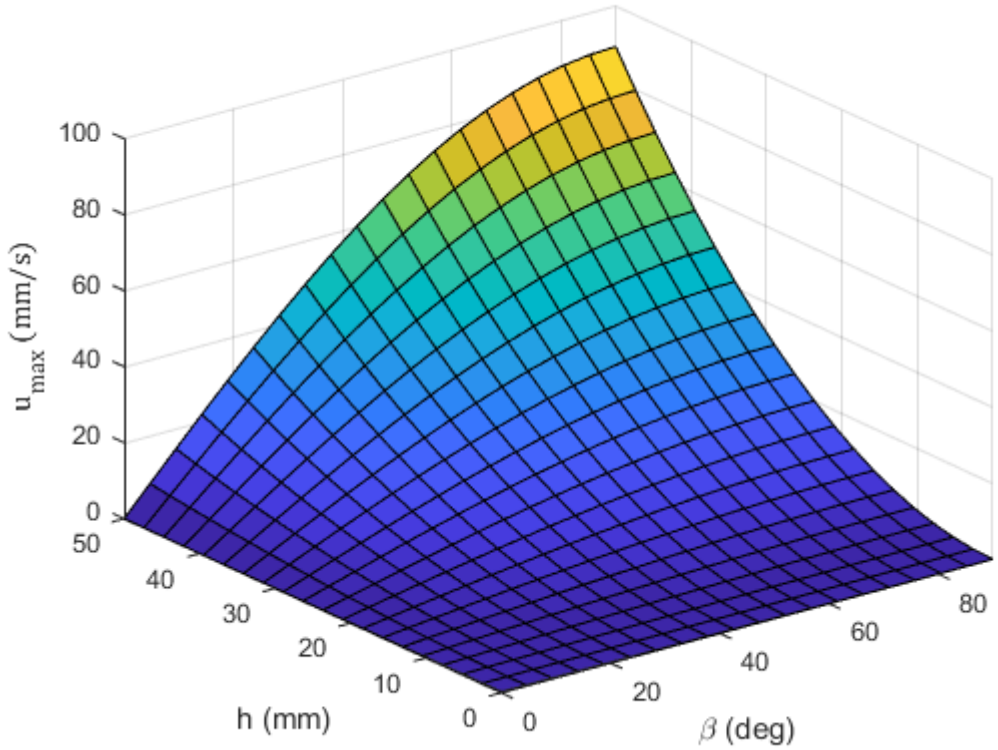

Figure 9. Parametric study of the independent variables, flow height h, inclination angle β and streamwise velocity, u. Dynamic viscosity μ of Golden Syrup 58 Pa·s at 22°C from *Llewellin, Mader, and Wilson (2002).*

Using the analytical solution from Takagi and Huppert (2007) in equation (**Eq. 11**), a 3D graph, (Figure 9) of the velocity as a function of the inclination angle from, $0° < \beta < 90°$ versus the flow height from, $0\ \text{mm} < h \leq 50\ \text{mm}$ is plotted using MATLAB. Viscosity was fixed at $\mu = 58$ Pa·s and the maximum streamwise velocity for each across the parameter space was calculated. Viscosity was chosen as the fixed parameter because u_{max} has a reciprocal relationship with kinematic viscosity ν:

$$u_{max} \propto {}^{1}/_{\nu}$$

There is a monotonic increase in maximum velocity as h and β increase to a peak streamwise velocity of $89.1\ \text{mm/s}$ for $h = 50\ \text{mm}, \beta = 90°$. The velocity increases non-linearly with inclination angle in a sinusoidal pattern with maximum velocity peaking at 90° which is intuitively expected and seen in equation **Eq. 13** that defines the parameter M. Velocity also increases non-linearly with an increase in free surface height such that, $u_{max} \propto h^2$, a

relationship as demonstrated in equation **Eq. 10** and that can be seen in the a_{ij} coefficients of equation **Eq. 12**. Therefore, it is seen that the system is very sensitive to changes in flow thickness, and moderately sensitive to changes in inclination angle between 0 and 90°. Therefore, these two parameters will be varied four times each for a total of $2^5 = 32$ experiments. This will be attempted in the ranges 0°<β<90° and 0 mm<h<50 mm.

2.2.6 Entrance length

In order to match the experiments to the COMSOL model the data must be collected from the experiments when the flow is fully developed. To determine when the flow is developed or in a steady state the entrance length of the flow must be considered.

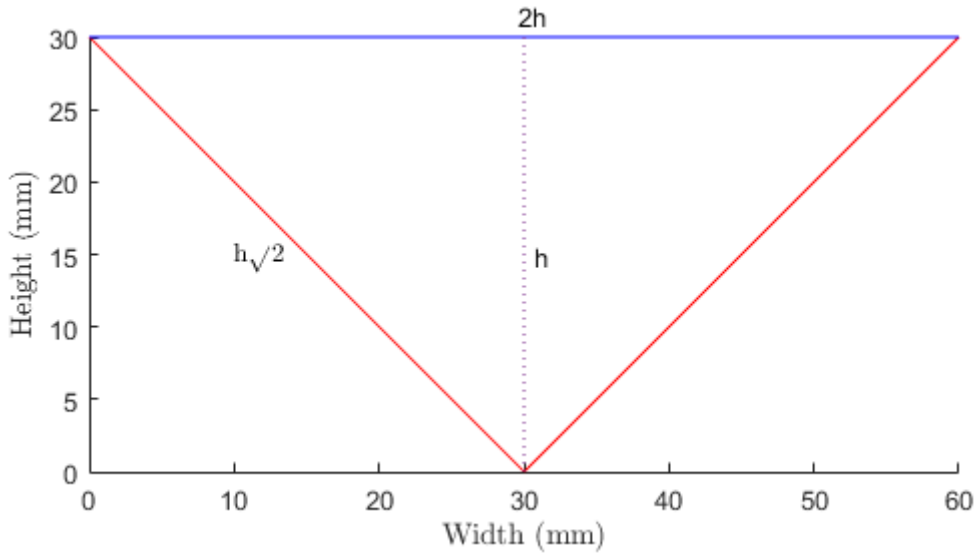

Figure 10. Wetted perimeter in red, flow surface in blue.

The entrance length is defined as the distance the flow must travel before the central velocity has reached 99% of its terminal value.

$$L_h = .05 R_e D_h$$

In the V channel the area of a 45°- 45°- 90° isosceles triangle as shown in Figure 10, is:

$$A = h^2$$

The perimeter of the cross sectional area that is wetted P, is:

$$P = 2\sqrt{2}h$$

D_h is defined as the hydraulic diameter and is given by,

$$D_h = \frac{4A}{P} = \frac{4h^2}{2\sqrt{2}h} = \frac{2h}{\sqrt{2}}$$

Therefore L_h is,

$$L_h = 0.05Reh\sqrt{2}$$

Substituting in the Reynolds number, $R_e = 0.0037$ for golden syrup from Table 6 and a flow height h, of 30 mm gives $1.57\text{x}10^{-6}$ m for the flow to have a fully developed velocity profile. While the theory suggests that this is very small, in practise the flow did appear (Figure 11) to take longer to develop in the z direction. This is most likely due to the fact that the entrance length equation is for pipe flow and not V-channel flow. Plotting the convergence of the Takagi solution over time we can see in Figure 11 how long it took the flow to converge for a test flow. Therefore video was acquired after a displacement of z = 500 mm.

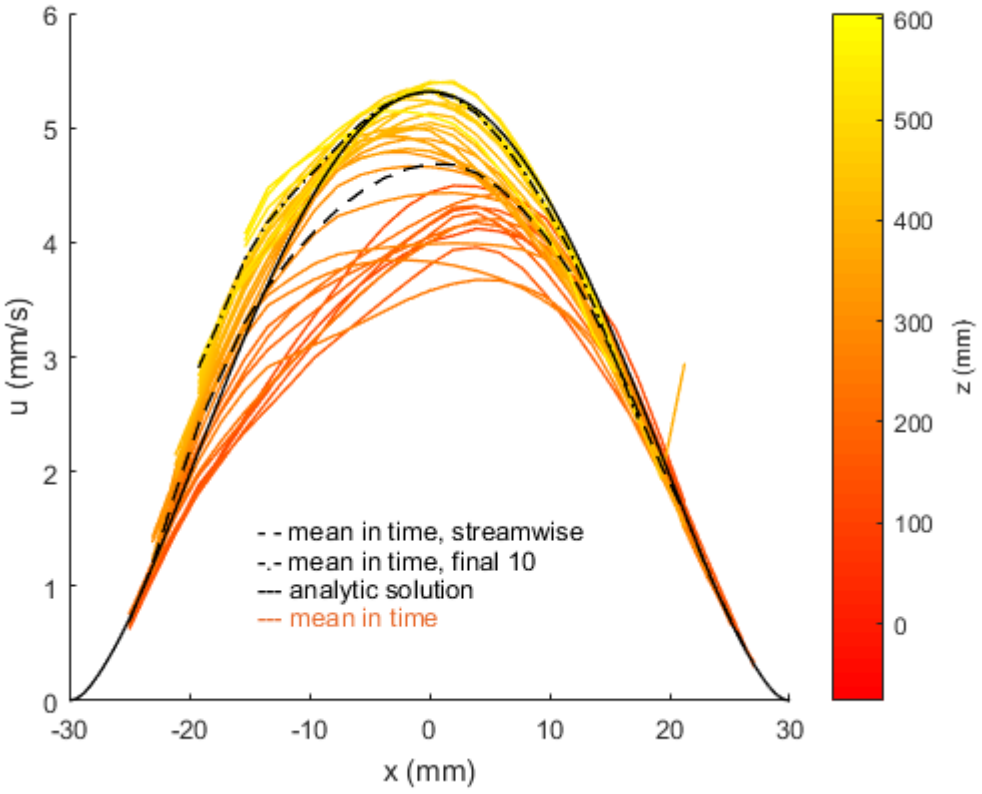

Figure 11. Velocity in the streamwise direction has converged within z < 500*mm*.

2.3 Experimental setup

Figure 12 and Figure 13 show the experimental setup. A 1m length of 10 cm thick V shaped stainless steel channel was purchased and mounted onto a table and secured in place with timber. The head of the channel could be raised to create an inclination angle that could be recorded. A 10 L container with a tap in the bottom was filled with 5L of Chelsea brand golden syrup. A weir was placed at the top of the channel and a removable dam was inserted 150 mm downstream to allow fluid to collect a significant volume before the dam was removed and the fluid allowed to flow down the channel. The weir allowed some control of the flow depth, h to enable repeatability as the head pressure dropped in the supply tank. This was faster than refilling the head tank as removal of the polystyrene beads took considerable time. The weir also allowed fixed volume experiments to compare with the steady state if required.

Figure 12. The Inclined V channel set up as used in the golden syrup experiments.

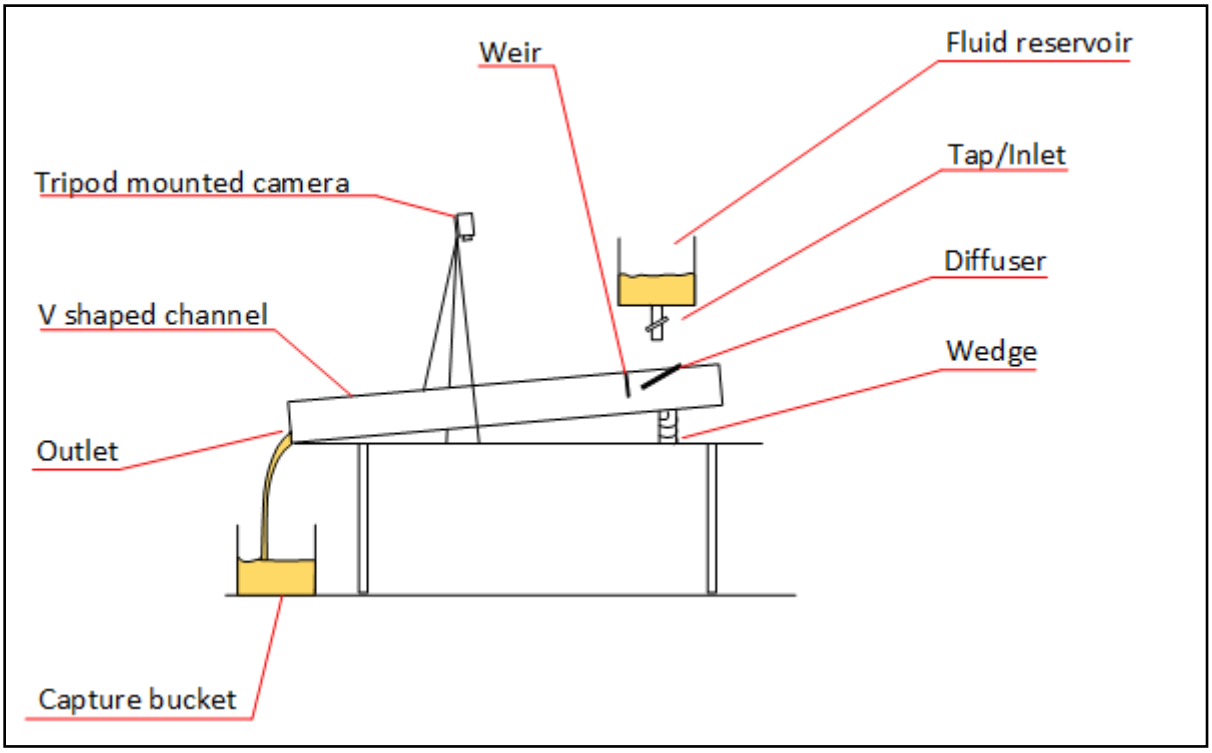

Figure 13. Schematic representation of the experimental setup.

To determine the free surface velocity field of a fluid moving down an inclined V channel, a range of velocities spanwise (x direction, Figure 7) across the flow were recorded. White polystyrene beads were used and sprinkled randomly across the flow as it exited the weir at the top of the channel. Polystyrene was chosen for several reasons: it is low cost, it floats without breaking the surface on top of the fluid, its white colour is a good contrast for video capture and it is non-hazardous.

To enable sufficient contrast for video processing, as much ambient light as possible was blocked out using black plastic sheeting hung from the ceiling and the table was covered in the same material to reduce reflections and glare. The V channel was spray painted black. A Sony RX10mk3 DSLR camera was mounted on a tripod positioned perpendicular to the flow to capture video of the flow in motion. White balance was set manually and auto focus turned off. A metal ruler was placed inside the channel above the flow to provide a scale for the video analysis.

After the flow was initiated, video was captured when the front of the flow lobe reached the end of the channel and spilled into the collection bucket to allow the flow to enter a fully developed state. After completing a few trial runs, a mean free surface velocity in the streamwise direction was plotted to determine how long it took for the flow to develop.

The entire experiment, data processing and simulation process chain is complex and is detailed more clearly in the flow chart seen in Figure 14.

2.4 Data processing

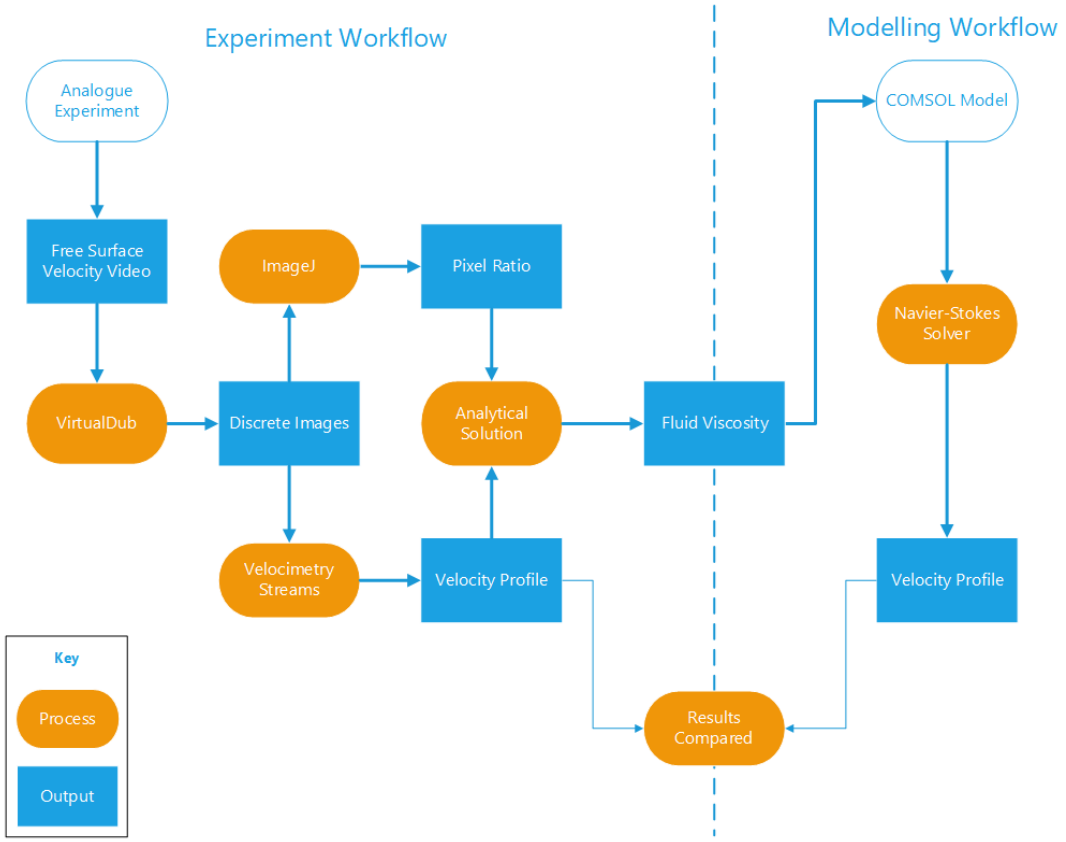

Figure 14. A visualisation of the workflow that shows how the data is processed and then compared with the solution predicted by the model. The blue boxes represent the data and the orange boxes are the software used to process the data.

2.4.1 Video processing

The interpolation software is sensitive to the time difference between photos and the velocity of the particles moving in the flow. If the particle is displaced too much between successive frames the software can fail to correctly track the particles. It was therefore much simpler to capture video and then use Veedub 1.9.11 video editing software to crop the video down to just the flow part of the frame and then decimate the 30 frames per second (fps) video into 1500 jpg images over a fifty second time interval. This optimal timeframe was derived by trial and error as the maximum velocity converged.

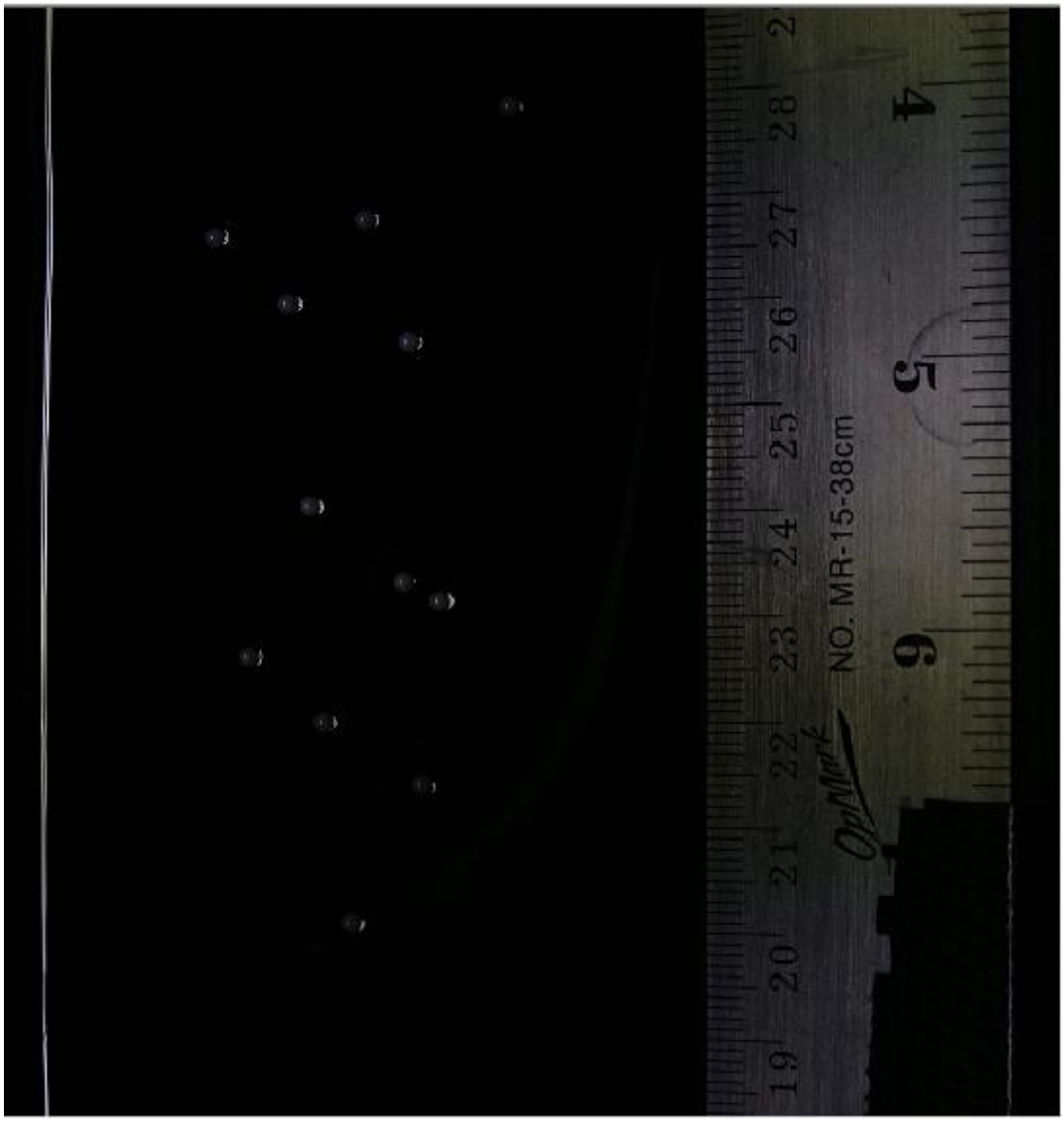

Figure 15. Beads entrained on the surface of the flow. The bright line on the left of the image is extraneous light reflecting off the meniscus between the flow and the V channel wall. The ruler is left in the frame for only a few seconds so that the pixel ratio can be calculated, it is removed from frame to help control light.

The unprocessed still image taken from the video in Figure 15 is cropped in Veedub so the bright reflection and ruler is removed. If they remain in the image then small artefacts (ghost particles) appear during the velocity processing from subtle changes in light during video capture.

The camera video is transferred to computer and opened in Veedub. The contrast is increased to 200 and the brightness dropped by one to eliminate bloom on the reflective surface of the golden syrup. A null transform is then applied to crop the full frame video down to just the flow in the V channel. A range of between 1000 and 2000 frames is selected that has a good

coverage of the tracking beads over the length of the image and the video is then exported as a sequential series of jpg images ready for velocimetry processing.

A single frame with the metal ruler in focus is exported as a jpg file from Veedub and loaded into ImageJ 1.52a. The ImageJ ruler tool is used to measure the width of the flow in pixels, and by measuring the number of pixels along a visible section of the ruler the number of pixels per millimetre can be determined. Since the V channel is a right angle, Pythagoras theorem can be used to calculate the flow depth, as seen in Figure 10.

2.4.2 Velocimetry

Images are imported into computer software called Streams 2.06 (Nokes, 2018) for analysis. Streams uses differences in intensity and geometry to identify the seed particles. A new image sequence is created in Streams. The temporal step is seconds and the interval is determined as the reciprocal of the camera's framerate 1/50 or 0.02 secs per image.

The particles within the image are then identified using a monochrome single threshold algorithm, with a threshold between 25 and 70 depending on lighting conditions during video capture. It was found that 30 gives the best results with the least number of ghost particles from bubbles and the meniscus formed at the flow edges.

After the particles are identified (Figure 16) a particle tracking velocimetry (PTV) analysis is conducted using a distance costing method with default values for weighting power, distance weight and reference length. Finally a velocity field is generated using Streams' default values for all parameters. From the velocity field the calculator tool is used to calculate a velocity, v with axis variables as spanwise (x), and averaged in depth and time, ($\overline{y}$, $\bar{t}$). The velocity profile graph is inspected and the velocity field data is then exported as a header-less csv file.

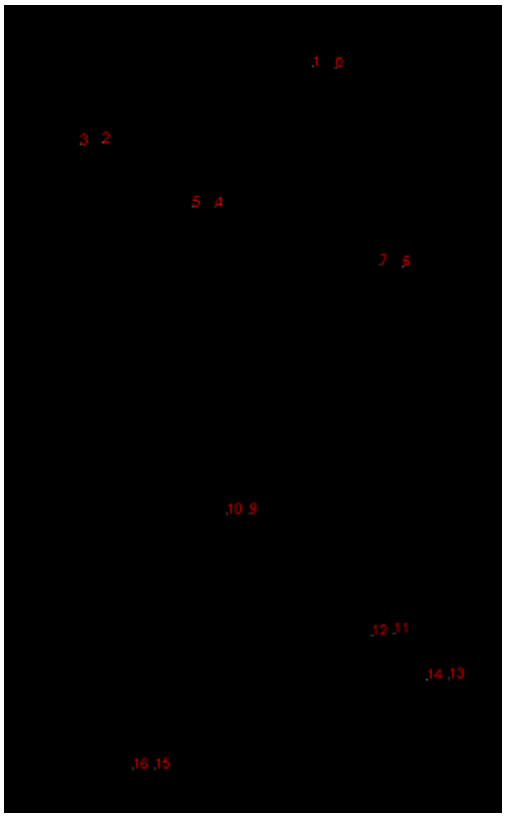

Figure 16. Seed particles are identified and numbered by Streams using the contrast between pixels. This process is sensitive to contrast so anything in frame that is reflecting light can interfere.

2.4.3 Viscosity computation

Three methods were used to calculate and compare the viscosity of the golden syrup:

1. Particle tracking velocimetry from experiments.
2. A Haake RC 20 viscometer in the department of Chemical and Process Engineering, (CAPE).
3. A method that uses the relationship between viscosity and refractive index.

2.4.4 Newtonian viscosity calculation method 1

The output of the velocimetry software Streams is a velocity field generated by plotting $\overline{x}, y, \overline{t}$. The maximum average velocity u, in the flow direction, is then used to solve **Eq. 11** using a computer program written in Python 3.6 and Jupyter notebook to derive the dynamic viscosity (see Appendix VII Takagi python function).This inverse model solves for the input viscosity with the analytical solution.

The computer code uses two 'for-loops' to perform the double sum in the Takagi steady state equation (**Eq. 11**). The equation is solving for velocity so an initial best guess of the viscosity is made using published data. This estimate seeds the initial calculation attempt on viscosity, iterating in large increments until the output model's maximum velocity exceeds the measured experimentally observed velocity maximum. This is necessary to reduce the computer processing time it takes to complete the calculation. Finally, the last incremental viscosity value used by the program before the experimental velocity was exceeded is then fed back into the model. This allows for a more refined estimate for the viscosity.

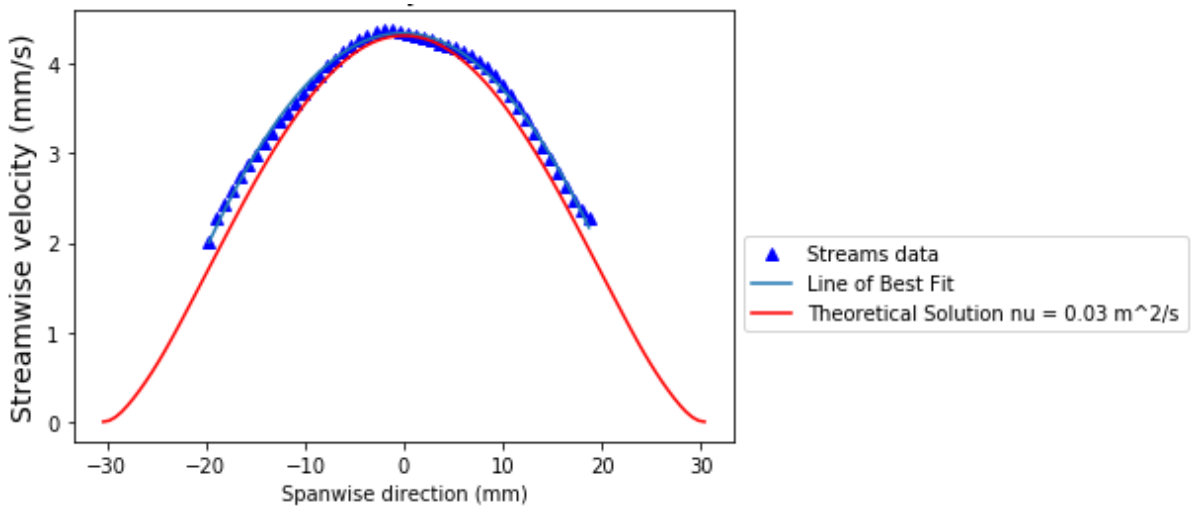

Figure 17. The best fit solution is the one that minimises the area between the two curves. In this image, experiment 45's data is fitted using a least squares method. The curve is then matched to the theoretical model by varying the viscosity of the model while minimising the difference in area between the two curves.

For this fine-tuning stage, an objective function is used.

$$I = \int_a^b |D(x) - F(x)|dx$$

Where F(x) is the analytical solution and D(x) is the function that describes the experimental data, a and b are the channel boundary where the velocity is zero.

The area under the velocity curve, from the velocimetry software Streams (the light blue line between the blue triangles in Figure 17), is calculated using Python's 'polyval' function to derive an equation for the curve. Here is the example from Figure 17.

$$\text{Fitted quadratic through experimentat data} = -0.006112\,x^2 - 0.001725\,x + 4.345$$

It can be seen from Figure 18 that the analytical solution is not parabolic but more bell shaped. The curvature of the Takagi solution changes and approaches zero as the solution approaches zero velocity. This is most likely due to the boundary conditions in the Takagi solution. The experimental data plots on the analytical curve in the same place as the parabola above the dashed red line of demarcation. Therefore it is acceptable to approximate the analytical solution using a parabola. While it was not implemented at the time, deriving the line of demarcation and limiting the objective function to minimise the area under the parabola above the demarcation line would be more appropriate.

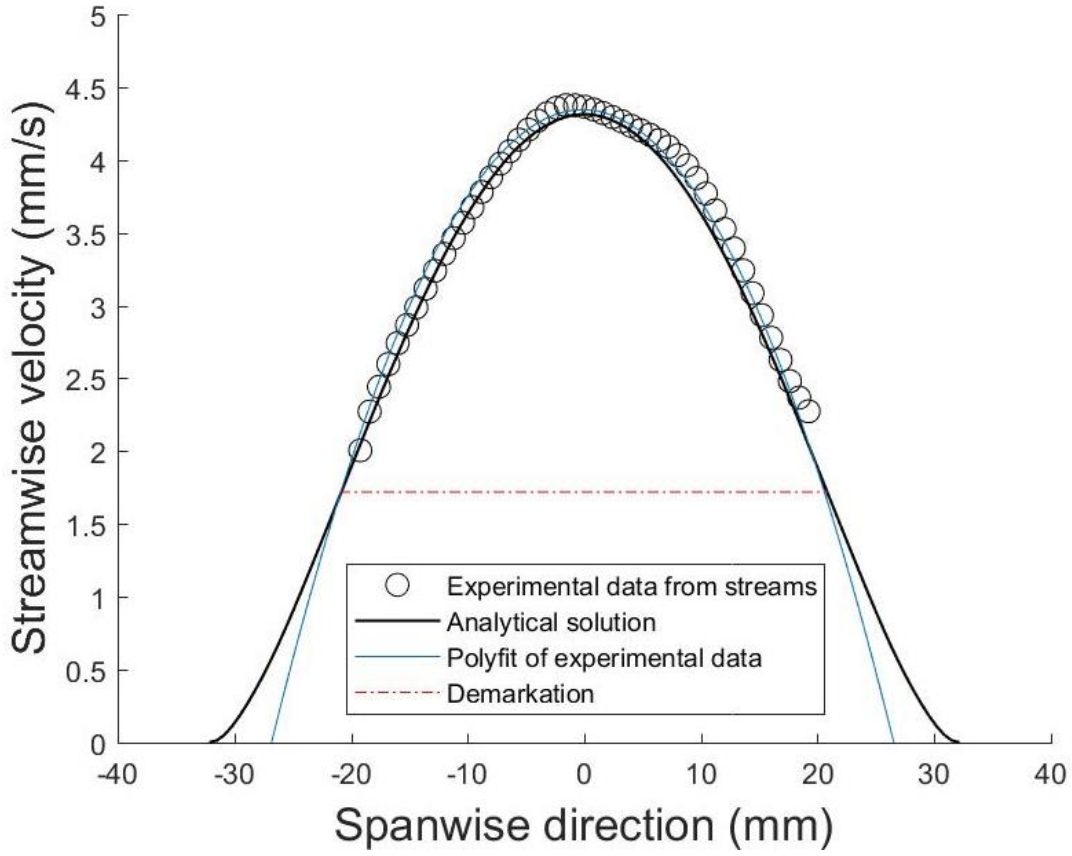

Figure 18. Parabolic fit of the streams data compared to the analytical solution.

The experimental data does not extend out to the edges of the flow because of the meniscus between the flow and the channel wall and a difficulty in entraining beads in that part of the flow. The roots of this parabola are therefore obtained from the ‘numpy-roots’ function. The

area is the integral between the roots of the equation, and the 'numpy-trapz' function was used to do a Riemann sum of the area under the graph.

$$\int_{-26.805}^{26.523} -0.006112\,\mathrm{x}^2 - 0.001725\,\mathrm{x} + 4.345 = 154.472\,\mathrm{m}^2 s^{-1}$$

The process is repeated for each velocity generated by the 'for-loops' of the theoretical solution, (the red line in Figure 17). The same functions are used to generate equations for the parabolas and then their areas are determined in the same way. The process is repeated by incrementally increasing the best guess of viscosity until the difference in area between, the velocity profile from the experiments, and the velocity profile from the equation is minimised. The final result is the viscosity required to produce the velocity profile.

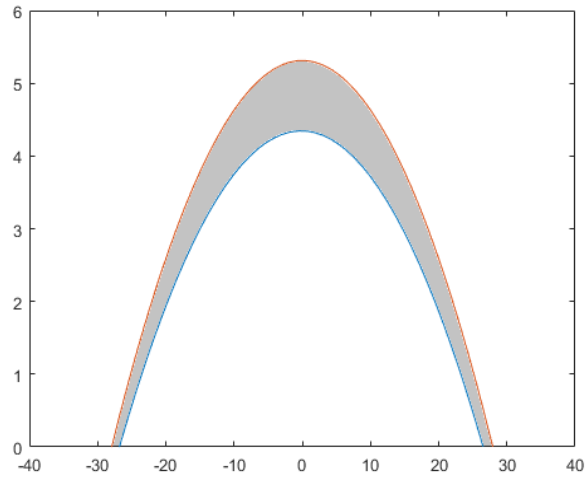

Figure 19. Experimental Velocity profile in orange, analytical in blue.

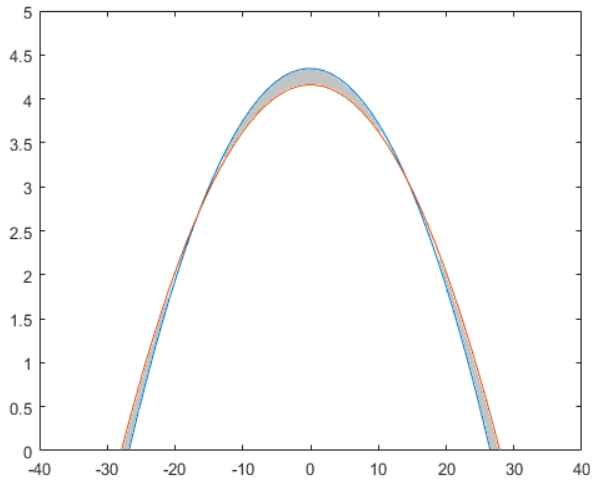

Figure 20. Area between the two parabolas has been minimised.

The grey shaded area represents the difference between the two solutions. By minimising this difference the best fit viscosity is determined. For example, in Figure 16 the area under the velocity profile of the experimental result (orange parabola) is calculated to be: $154.4918\,\mathrm{m}^2\mathrm{s}^{-1}$, the area of the analytical velocity profile (Figure 20 blue parabola) is calculated to be: $154.4989\,\mathrm{m}^2\mathrm{s}^{-1}$. The difference of areas after the optimisation: $0.0071\,\mathrm{m}^2\mathrm{s}^{-1}$.

The resulting viscosity derived from the analytical solution is used along with the other experimental parameters (density, flow thickness, inclination angle) for the golden syrup as

input for the computational model using COMSOL. The output velocity field from COMSOL is compared to the velocity profile from the golden syrup experiments.

2.4.5 Newtonian viscosity calculation method 2

A sample of the golden syrup was collected midway through the experiments and analysed by Associate Professor Ken Morison on the CAPE laboratory's Haake RV20 viscometer. The viscometer and syrup samples were preheated to the same temperature as the volcanic processes laboratory where the experiments were conducted, 20.7°C. The viscometer was calibrated using Canon viscosity reference standard oil n1000 before analysis. Viscosity was measured twice. The shear rate was ramped up at a constant rate then held for 20 seconds and then ramped down. This was done to check for hysteresis in the fluid (Huxley, 1967).

2.4.6 Newtonian viscosity calculation method 3

There is an empirical relationship between viscosity, density and molecular mass. Associate Professor Ken Morison measured the refractive index of the golden syrup on an Atago NAR-3T refractometer and determined it to be 1.4948 which gave an associated 81.55% molecular mass of sucrose and a density of 1418 kg m^{-3}. From the relationship:

$$\mu_{sucrose} = \mu_{water(T°C)} \times e^{\left(dAs \times dSW + dBs \times dSW^2\right)}$$

Where the coefficients are defined as,

$$dAs = 0.000693T + 3.165$$
$$dBs = 0.000022T - 0.00631$$
$$dSW = \frac{m_f}{(1 - m_f)}$$

Where T is temperature m_f and is mass fraction and are taken from the CRC handbook of Chemistry and Physics (Lide, 1999). This equation was implemented in MATLAB to calculate the dynamic viscosity of the golden syrup at an ambient room temperature of 20.7°C and a water viscosity of 0.0009835 Pa·s.

2.5 Non-Newtonian fluid

For non-Newtonian fluids, there is no analytical solution. Once the velocity profile has been determined using the same methodology as the Newtonian fluid, the velocity profile is then used as input into the COMSOL model along with the other independent variables, flow depth, h, flow inclination angle, β, and fluid density, ρ. The COMSOL model is extended to use the power law **Eq. 9** to solve for a non-linear relationship between the shear stress and the strain rate of the non-Newtonian fluid. Figure 21 shows the updated flow chart of processes involved. The dotted box shows the experimental workflow that is unchanged between methods.

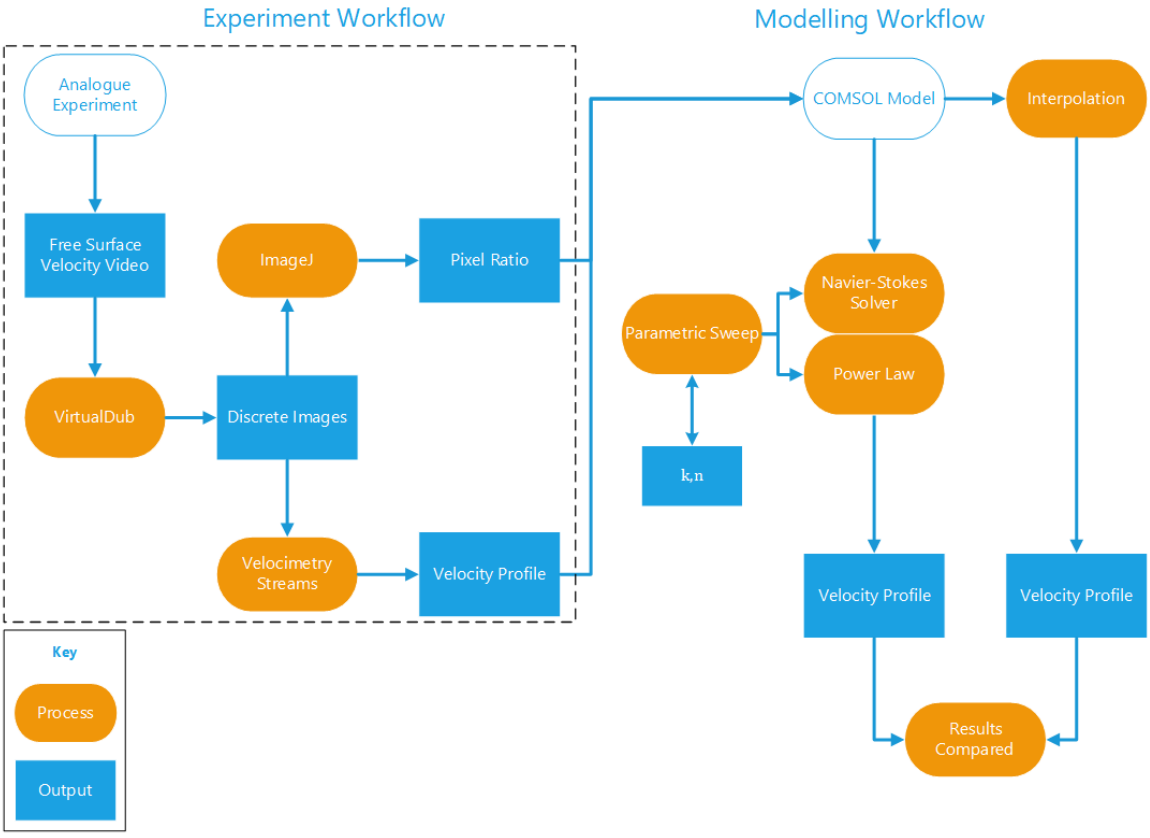

Figure 21. Updated flow chart of non-Newtonian parameter identification method. The dotted black outline highlights the data collection process which shares a common methodology with the Newtonian fluid, with the exception of an analytical solution, which is not available for non-Newtonian fluids. The modelling process is completed entirely in COMSOL.

2.5.1 Carbopol® preparation

The Carbopol® was prepared in accordance with the manufacturer's recommendations, for full details see Appendix III Preparation of Carbopol® polymer 980.

2.5.2 Data processing

For each experiment conducted with the non-Newtonian fluid, Carbopol® 980, the process of acquiring the data was the same as it was for the Golden Syrup. The video of the fluid in motion was processed the same way as the Newtonian fluid with Veedub64 and Streams 2.06. The output table of spanwise displacements vs velocities from streams needed to be adjusted before it was used in COMSOL.

The data was loaded into MS Excel. The pixel ratio was calculated the same way using ImageJ, and a correction was applied to the spanwise (x) values and an offset of half the flow width was applied to centre the data at $x = 0$.

A new 1D component was added to the COMSOL model used for the Newtonian modelling and the Global ODE and DAEs module was added to this component. Under Geometry an interval was created with a range that spanned the flow width of the velocity profile. A point was also added and the x values were populated with the spanwise x values from excel.

2.5.3 Viscosity computation

Two methods were used to calculate and compare the viscosity of the Carbopol®:

1. Particle tracking velocimetry from experiments.
2. Anton Paar MCR302 Rheometer in the CAPE laboratory.

2.5.4 Non-Newtonian viscosity calculation method 1

Once the experiments were completed and the data had been processed through Streams, it had to be imported into COMSOL. An interpolation function was added to the COMSOL

'Definitions' tab and data was sourced from the excel csv file containing the corrected Streams data. The interpolation was then plotted (Figure 22).

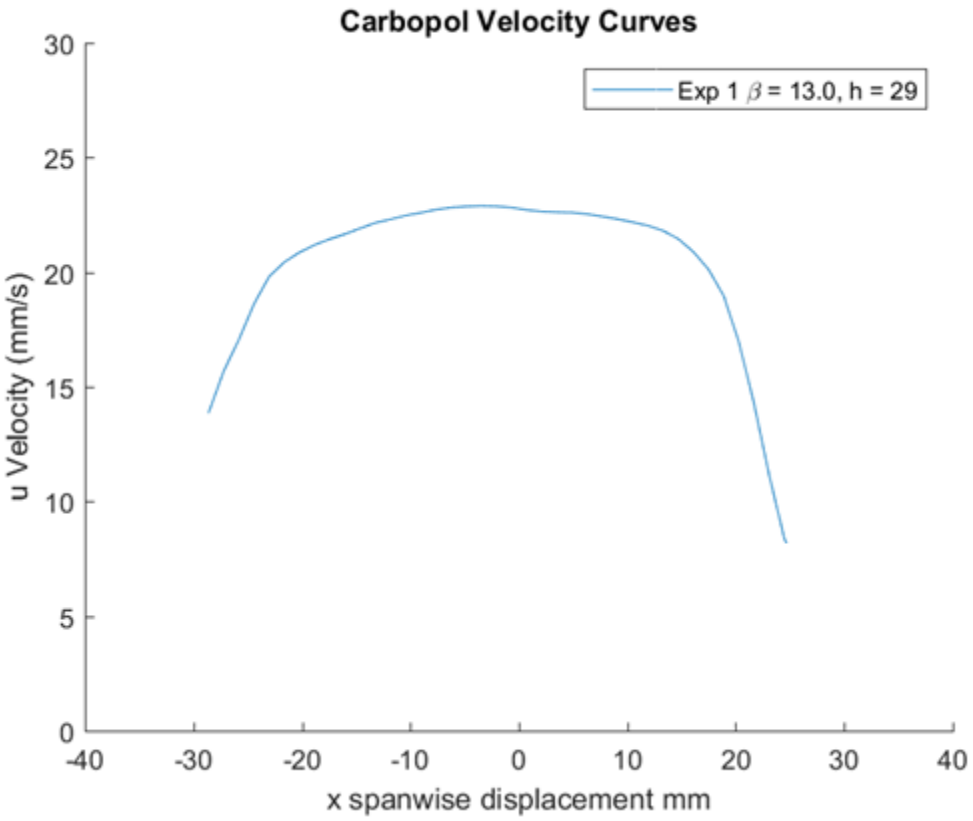

Figure 22. COMSOL Interpolation of the Streams data.

The parameters for flow height and the variables for flow inclination angle were set in COMSOL, as measured during the experiment. In COMSOL, the 'Laminar Flow' module was changed for non-Newtonian fluids. Under fluid properties (Figure 23) non-Newtonian power law was selected. The fluid consistency index, m and the flow behaviour index, n were set as variables, m_pow, n_pow. These two new parameters were then added to, and defined in the global definitions parameters list.

A parametric sweep was created (Figure 24) and configured to sweep across a range of k (m_pow) and n (n_pow) coefficients.

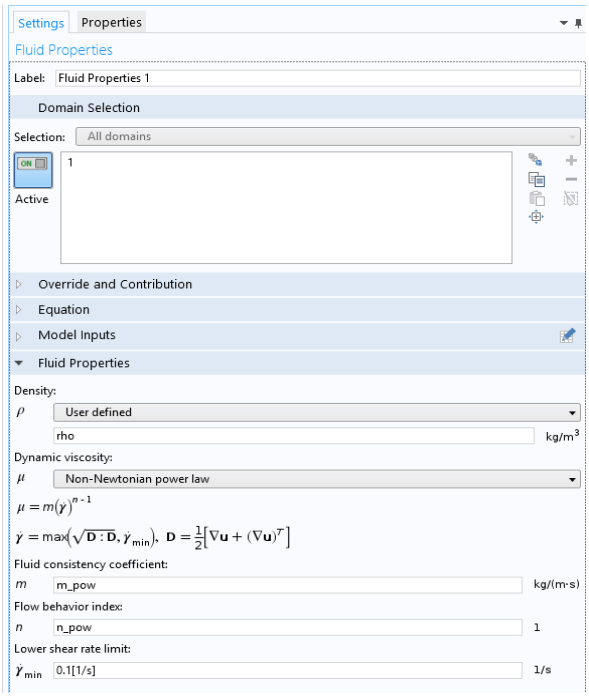

Figure 23. The Navier Stokes solver is configured to use the power law.

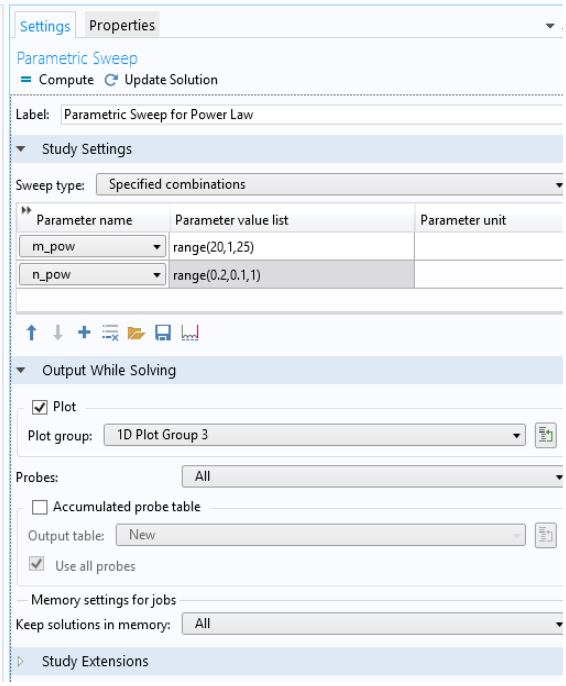

Figure 24. The parametric sweep parameter list allows for a range of values to be computed at once.

The velocity profile from Experiment 1 has a maximum velocity calculated from MATLAB of 22.9 mm/s. The velocity profile has a steep rise and fall and a wide maximum. The COMSOL solution with the best fit to the shape and velocity maximum is the green line in Figure 25 (bottom right) from k = 18, n = .2.

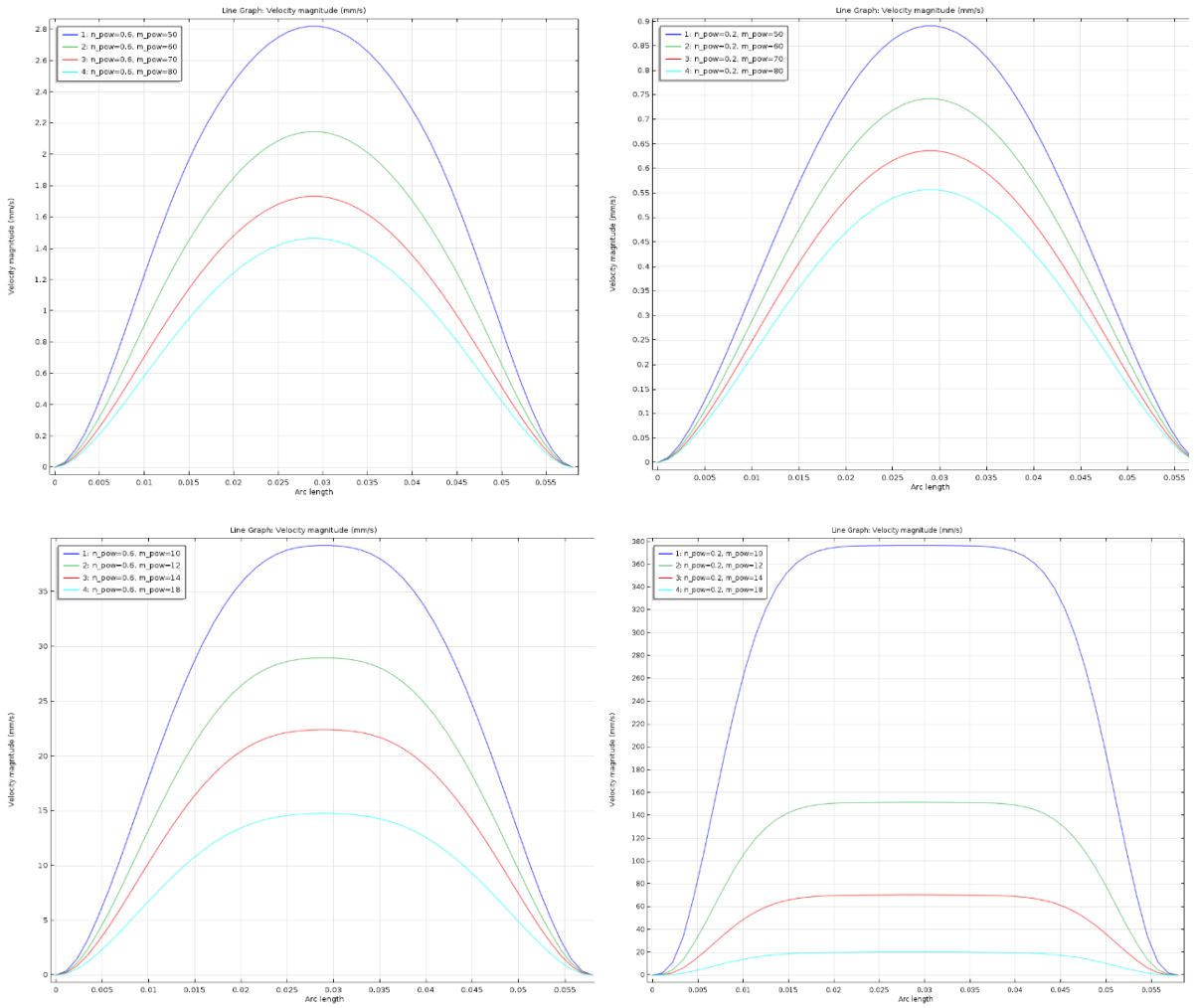

Figure 25. Velocity profiles converging on the experimental data in the teal coloured line.

The m variable was then further refined to minimise the gap between the two peak velocities between the COMSOL model and the experiment 1 data.

Table 7. Parametric sweep parameters for determining k and n for the power law.

n	k	line maximum	k	line maximum	k	line maximum
0.2	17.5	23.252	17.55	22.928	17.56	22.864
0.2	17.75	21.686	17.6	22.61	17.57	22.8
0.2	17.8	21.389	17.65	22.297	17.58	22.736
0.2	17.9	20.809	17.7	21.989	17.59	22.673

The results were then plotted over the imported experimental data. The closest match was selected (e.g. the green line in Figure 25 bottom right) and used to re-optimise the sweep until the solution matched the experimental velocity profile.

2.5.5 Non-Newtonian viscosity calculation Method 2 by Anton Paar rheometer

The newly commissioned Anton Paar MCR302 rheometer was used to measure the viscosity of the Carbopol®. The cup and bob was used for the measurements. The sample was placed in the cup and the overflow was cleaned away. The sample was then preheated to 21.7°C and then the test was performed three times. The torque was ramped up to the highest shear rate, a pause of 20 seconds was added to the process and then the sample was ramped back down. This method would reveal any hysteresis in the fluid.

This method meant that if the sample did not follow the exact same path back down again there was some thixotropic effects in the fluid. If there were indeed a hysteresis loops, they would be visible in a shear rate vs. shear stress plot.

Figure 26. Anton Paar MCR302 Rheometer in the CAPE laboratory. Rheocompass software is running on the PC and the temperature controlled water bath is below the Rheometer on the floor. A ball and cup has already been fitted to the rheometer.

2.6 Assumptions

All models invariably have to make compromises. Here is a list of the simplifications used in these methods to model lava flows using golden syrup and Carbopol® flows in V channels.

1. **An analogue fluid is used in place of basaltic p$\bar{a}$hoehoe lava.**

   Justification: Analogue fluids are easier, faster, cheaper and safer to work with than hot lava. The method of measuring the free surface velocity and calculating the viscosity is transferable to lava at a later stage.

2. **Experiments are isothermal.**

   Justification: It is also recognised that yield stress and viscosity are temperature dependent and that along the entire length of a lava flow, temperature varies from the vent to the most distal front. This effect was investigated by M. Dragoni, Bonafede, and Boschi (1986) and N. Dragoni (1989) and it was found that the temperature drop in many lava flows was less than 100°C from vent to front. Over a small enough distance the flow can be considered isothermal, because a thermal boundary layer forms at the flow surface and reduces heat loss. The entrance length of the flow in these experiments is 150 mm. In other words, the flow is fully developed within 150 mm of leaving the inlet and the fluid viscosity can be calculated from the free surface velocity of a 100 mm video frame of the flow. The free surface velocity of a lava flow that is fully developed can be measured over the same spatial distance. Any temperature difference from the top of the video frame to the bottom will be negligible. These low temperature isothermal experiments and convergence analysis will help identify the minimum flow length required to achieve a reliable flow velocity to improve future non-isothermal models.

3. **The syrup and Carbopol® fluids are homogenous.**

   Justification: Lava is composed of melt, crystals and volatiles which combine to define the overall viscosity. However, this approach is concerned with the velocity gradient relationship with viscosity so the effect of different individual components is not relevant (Harris & Rowland, 2015).

4. **The initial syrup fluid is Newtonian.**

   Justification: The initial experiments used simpler Newtonian fluids to create the models. This can then be validated independently using the Takagi and Huppert (2010) analytical solutions before the models are extended to more complex non-Newtonian fluids. In many cases, natural lava flows behave as Newtonian fluids (M. Dragoni & Tallarico, 1994); high temperature flows with few bubbles and a crystal fraction below $0.44\Phi_m$ (where Φ_m is the maximum packing fraction) (Castruccio et al., 2014). The melt component of lava is considered to be a Newtonian fluid (Griffiths, 2000)

5. **The non-Newtonian fluid is Shear thinning**
   Justification: Lava is made up of crystals, melt and bubbles. These components combine to change the rheological properties of lava. For example bubble formation and deformation can create thixotropic properties in the flow as bubbles deform and recover in relation to shear stress (N. S. Bagdassarov, 2004). Lava can exhibit shear thinning properties due to a strain rate dependency. It can also exhibit a yield stress dependency i.e. Bingham fluids. Lava flows can also combine these two; a shear thinning lava with a yield stress would be a Herschel-Bulkley fluid. Since lava flows can exhibit multiple flow regimes, this project will attempt to use a power law to model shear thinning fluids as they have fewer unknown parameters to solve for and are less complex than Herschel-Bulkley fluids.

6. **The flow channel will be V shaped.**
   Justification: Topography, temperature and effusion rate also effect the rheology. If the effusion rate and the temperate remains near constant, and lava flow is gravitationally driven by topography, then levies can form that confine the flow to narrow channels. As the edges of the flow further cool they can close over, becoming immobile and forming insulated lava tubes. In these flow conditions, the fluid behaves predominantly as Newtonian in nature and encompass the majority of the lava flow. E.g. Mt Etna's 2001 LFS-1 flow was 97% channel constrained (Pinkerton, H. Sparks, 1996).

   Takagi and Huppert (2010) explored the relationships between channel shape and flow characteristics and concluded that the channel morphology does not have a large influence on the flow. In their earlier paper (Takagi & Huppert, 2007), the authors presented the analytical solutions to rounded channels and V channels, a necessity for testing the efficacy of the model to be developed here. As a consequence of using this analytical solution the flow must be laminar, fully developed and have a constant flux. The advantage the V channel has over the rounded channel is that in eventual temperature dependent experiments a V channel has less surface area and should stay hotter longer and thus flow further before freezing. Most importantly however, the V channel allows the methodology to be tested against channelized flow and extending the model to other channel morphologies should be straightforward.

7. **Crustal effects are omitted.**
   Justification: Basaltic p$\bar{a}$hoehoe lava flows form crusts as they cool on the surface. Work has already been done to investigate the relationship between the folding on the crust and its rheology (Gregg, Fink, & Griffiths, 1998; Farrell et al., 2018). The effect of the crust on the flow is twofold: the crust causes drag until the underlying flow eventually detaches and the flow becomes a lava tube. The crust also insulates the flow beneath it. The viscosity of the crust will therefore be different to that of the flow beneath it due to temperature differences and crystal content. It is not possible to directly observe the flow when it is sealed inside a lava tube with the exception of skylight openings that might appear. The free surface velocity method could be used in the skylights, but other methods would be required to calculate viscosity within a lava tube.

Figure 27. Lava tube skylight surrounded by ropy textured p$\bar{a}$hoehoe lava crust. *(Creative commons, pixabay GmbH, 2016)*.

Chapter Three: Results - Newtonian Fluid

This chapter presents the results of the experiments. The Newtonian syrup is presented first followed by the non-Newtonian Carbopol®. The results of testing the Newtonian fluid are presented starting with the Haake viscometer, the Atago refractometer and finally the results of using the analytical solution with the experimental data to calculate the viscosity. These results are then compared to the COMSOL model predictions in each experimental case.

Rheometer and refractometer results for Newtonian fluid

The viscometer measured the viscosity of the syrup and the results are displayed in Table 8. It can be seen that there is no single value for the dynamic viscosity of the fluid and that the viscometer gives a range of values. This represents the uncertainty in the viscometer's measurement. A sample of golden syrup was tested in the rheometer after the new rheometer was commissioned and the old viscometer retired, which was done to ascertain the relationship between changing shear rate and viscosity. This sample was tested without being used in the experiments and had never been exposed to the laboratory environmental controls, and thus represents the unaltered fluid conditions. It matches up well with the trend in fresher experiments in the series with a dynamic viscosity of 26 Pa·s.

The result from the refractometer was less than that of the viscometer but it is seen that the refractometer approach is extremely sensitive to the accurate measurement of the mass fraction of sucrose. A 1% increase in the mass fraction of the sucrose increases the viscosity of the syrup by 20 Pa·s. The manufacturer publishes a 0.3% accuracy of the Atago NAR-3T refractometer and this value was used to calculate the range in the calculating of viscosity. Refractometers are sensitive to impurities in the fluid and this could have happened as the syrup had been reused in the experiments. Refractometry is also temperature dependent and small changes in temperature can affect the results but only marginally where a ±0.5°C temperature change corresponds to a ±0.5Pa·s change in viscosity. There is a discrepancy between the viscometer and refractometer. It is proposed that the viscometer is more correct than the refractometer as the refractometer approach is based on a best fit curve to experimental data.

Table 8. Dynamic viscosity of the syrup. For the viscometer data, the mean is 62.4 and the variance is 1.7 with Bessels's correction applied for sample variance (Upton & Cook, 2014). Variance, (s^2) is the average of the squared distance from the mean, or a measure of spread from the mean. Results in brackets are for the one month syrup.

Method	**Viscosity (Pa·s)**
Viscometer test 1	60.85 - 61.96 (365 – 405)
Viscometer test 2	62.85 – 63.97 (365 – 430)
Refratometry	52.5 – 54 (672 – 702)

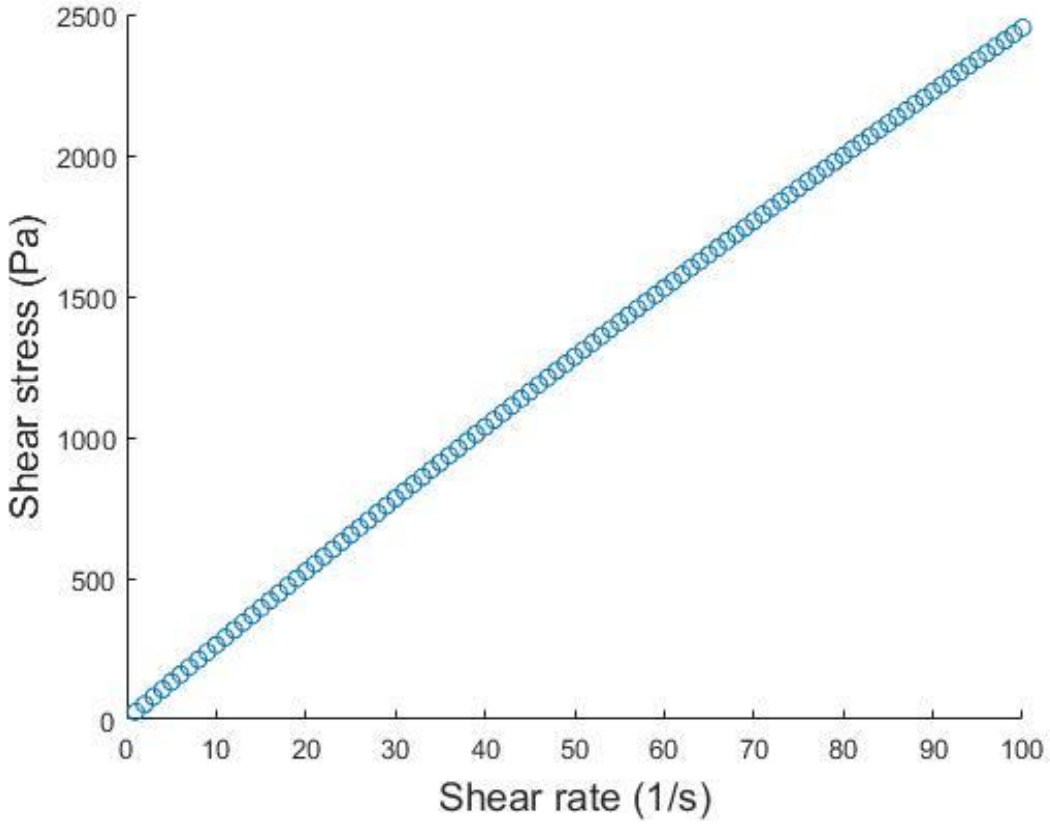

Figure 28. The shear rate-shear stress plot is linear indicating a Newtonian fluid. Shear thinning, Herschel Bulkley, shear thickening fluids have lens shaped curves. The line going through the origin also indicates the absence of yield stress. The gradient of this line is the viscosity.

Experimental results for syrup

Several pilot experiments were conducted initially in order to calibrate the equipment and improve the design. Once the system was finalised a series of 28 experiments were performed on the golden syrup. The data is summarised in Table 9 and Table 10. Experiment number, fluid inclination angle, (β), the fluid's flow width (w) and date and time were collected at the time of the experiment. The experiment is recorded on video and post processing variables, pixel ratio, offset, flow width, flow height and velocity are derived from the video analysis. In Table 10 the dynamic viscosity for each experiment was calculated using the analytical solution, and the mean ($\bar{x}$) was 60.2 and the variance (s^2) was 9.57

Table 9. Data recorded and processed from experiments. The fillet of the V channel was measured to be 3 mm. Strike through experiments are outliers that have been removed.

Experiment	Pixel	Beta angle	Flow width	Flow height,
~~1~~	7.9	10.0	54.0	24.0
~~2~~	10.4	10.0	57.0	25.5
3	8.1	5.5	45.7	19.9
4	7.9	5.2	50.3	22.2
5	10.5	5.1	49.3	21.6
6	10.2	9.5	50.3	22.2
7	8.9	9.5	52.9	23.5
8	9.0	10.5	51.4	22.7
9	9.9	14.3	50.0	22.0
10	9.6	23.0	41.9	18.0
11	11.8	20.5	41.2	17.6
12	11.8	17.5	43.4	18.7
13	11.5	17.5	42.5	18.3
14	10.1	15.5	44.3	19.2
15	10.4	15.5	42.6	18.3
~~16~~	9.3	14.0		
17	10.4	8.9	47.4	20.7
18	11.2	10.7	47.8	20.9
19	7.6	10.7	46.2	20.1
20	9.7	12.5	45.0	19.5
21	10.1	12.5	45.5	19.8
22	10.6	12.5	51.0	22.5
23	8.5	7.9	54	24
24	10.4	7.6	49.0	21.5
~~25~~	9.7	4.6	58.6	26.3
26	8.9	7.8	66.8	30.4
~~27~~	11.2	4.7	65.5	29.7
~~28~~	9.1	7.8	66.8	30.4

Table 10. Calculated values of viscosity, Reynolds number, Froude number and wetted perimeter from the observed velocity. $\bar{x}$ = 60.2 S^2= 9.57.

Experiment number	Maximum velocity [mm/s]	Dynamic viscosity [Pa·s]	Density [kg/m^3]	Reynolds number	Froude number	Wetted perimeter
1	2.9	26.9	1418	0.0085	0.0039	0.0562
2	1.5	59.6	1418	0.0022	0.0019	0.0627
3	1.5	55.3	1418	0.0024	0.0020	0.0612
4	3.5	46.8	1418	0.0067	0.0045	0.0627
5	3.2	58.1	1418	0.0051	0.0039	0.0663
6	3.5	53.9	1418	0.0059	0.0044	0.0642
7	3.6	66.6	1418	0.0048	0.0046	0.0622
8	4.7	53.9	1418	0.0063	0.0066	0.0507
9	3.3	66.6	1418	0.0035	0.0048	0.0498
10	3.7	58.1	1418	0.0048	0.0051	0.0529
11	2.8	73.7	1418	0.0027	0.0039	0.0516
12	3.6	55.3	1418	0.0050	0.0049	0.0542
13	3.0	61.0	1418	0.0036	0.0041	0.0518
14	2.4	63.8	1418	0.0026	0.0034	0.0495
15	1.9	70.9	1418	0.0022	0.0025	0.0586
~~16~~	-	-	1418	-	-	-
17	2.4	63.8	1418	0.0030	0.0032	0.0568
18	2.7	62.4	1418	0.0033	0.0036	0.0552
19	2.8	62.4	1418	0.0035	0.0037	0.0559
20	3.1	72.3	1418	0.0038	0.0039	0.0636
21	2.5	65.2	1418	0.0036	0.0030	0.0679
22	1.7	73.7	1418	0.0020	0.0022	0.0608
23	1.8	63.8	1418	0.0029	0.0021	0.0744
24	4.0	34.0	1418	0.0143	0.0044	0.0851
25	3.2	45.4	1418	0.0083	0.0035	0.0841
26	4.3	56.7	1418	0.0091	0.0047	0.0860
~~27~~	0.7	311.96	1418	0.0002	0.0008	0.0679
~~28~~	0.9	262.3	1418	0.0003	0.0010	0.0721

Sample velocity profiles generated over a range of high to low values for the independent variables, h and β are visible in Figure 29. The velocity for each experiment is parabolic in shape with u_{max} in the center of the channel flow that falls off to zero at the boundary. While it appears that the fastest flow has the most parabolic shape, this is an artifact of the graph axis as slower flows have lower maximum velocities. The flows do not all share the same intercepts on spanwise direction axis, where the streamwise velocity is zero because the wetted perimeter is different for each experiment. It was predicted that increasing the independent variables h and β would produce a monotonic increase in u_{max}. The relationships between h and umax and β and u_{max} are plotted and shown in Appendix V

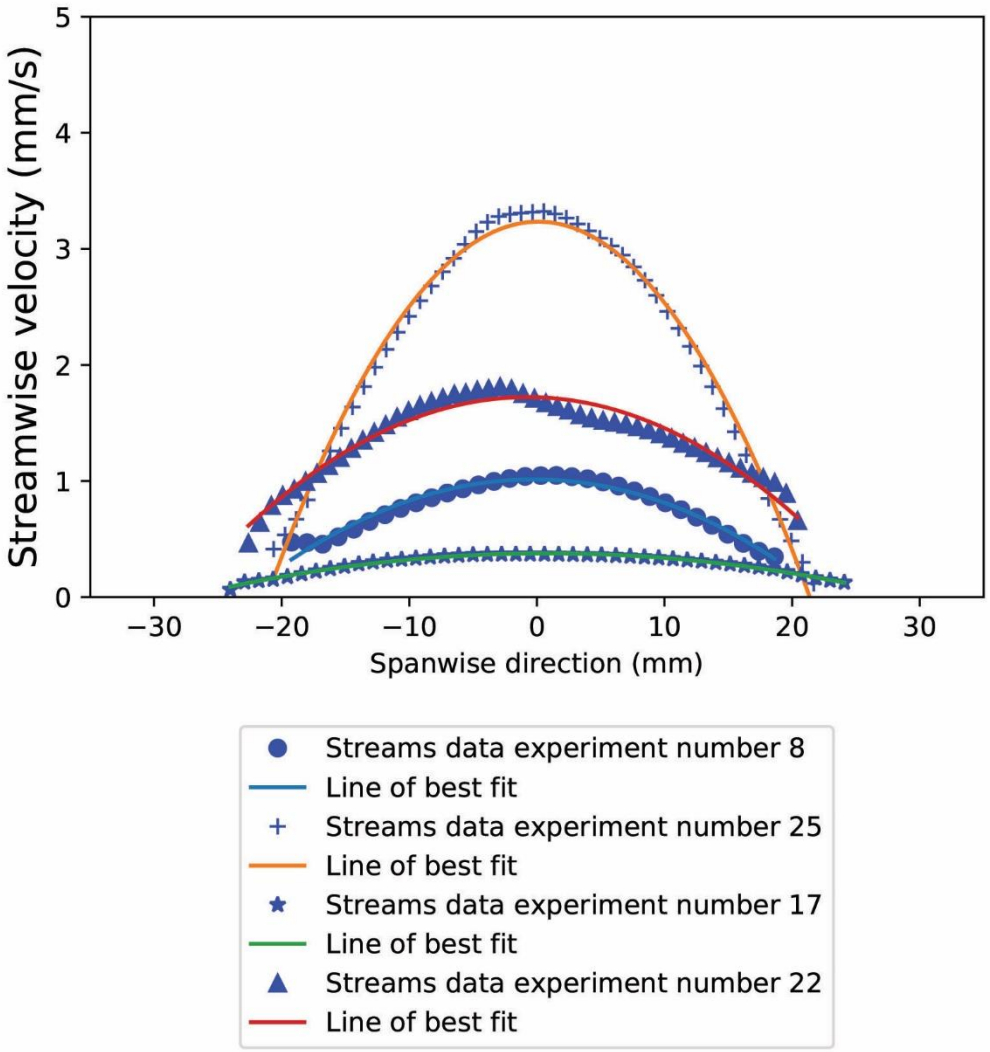

Figure 29. Four experimental velocity results calculated by Streams 2.06 and plotted together.

Analytical solution results for Newtonian fluid

To calculate the actual viscosity of the experimental data the analyitical solution was used. Once the velocity fields were determined for each experiment μ was then calculated using the Takagi equation. The corresponding analytical solution's velocity field was matched against the experimental one as closely as possible. Figure 30 plots the experimental velocity field generated from Streams against the velocity field from the analytical solution for experiment number 19. The analytical solution produced a symetrical bell shaped curve that appears parabolic in the middle but changes the direction of its curvature towards the edges. The u_{max} value fitted the experimental data very well. There was good agreement with the shapes and the position of the two u_{max} of the curves in the center of the flow, but poor agreement on the flow edges. The experiments lacked data in the low speed parts of the flow towards the channel edges due, in part, to the meniscus of the flow interfering with the image processing, and the size of the entrained bubbles catching, and sticking to the boundary walls.

Figure 31 shows the results of all the individual syrup experiments through time after solving the Takagi equations. The syrup shows an increasing viscosity trend as the syrup ages and sucrose crystals grow, bubbles form and the syrup dehydrates. The addition of fresh syrup towards the end of the experiments shows the viscosity drop as the water to sucrose ratio changes.

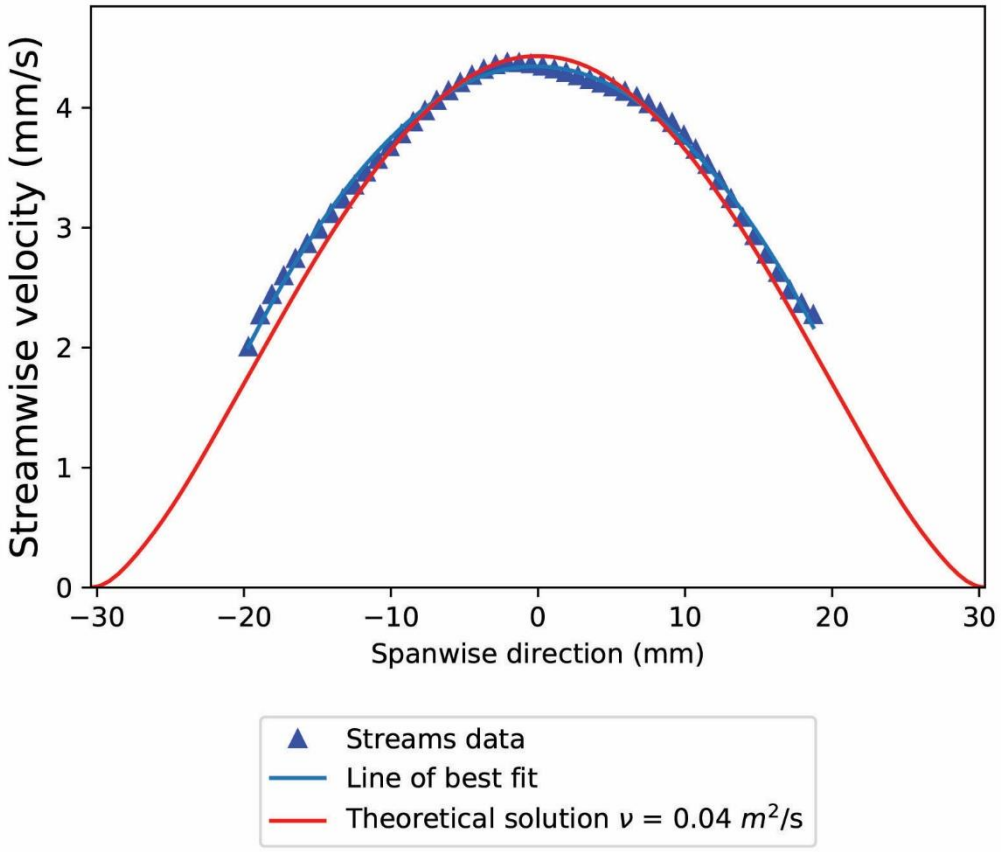

Figure 30. The experimental data from experiment 19 (blue triangles) plotted against the analytic solution (solid red line). The dynamic viscosity derived from the analytic solution is 58 Pa·s. The difference in area between the two parabolas of streams data and analytic solution is 154.51 m^2s^{-1} – 154.3 m^2s^{-1} = 0.2 m^2s^{-1}

Table 11. Experiment number 26 non-Newtonian fluid experiment and simulation properties.

Experiment type	**Steady state flow model**	**Fluid type**	**Golden syrup**
Incline angle (β) (degrees)	7.8°	Fluid density (kg/m^3)	1418
Depth of flow (mm)	30.4	Calculated kinematic Viscosity (m^2/s)	0.041
Experiment Max velocity (mm/s)	4.35	Dynamic viscosity (Pa·s)	58
COMSOL Model Max Velocity (mm/s)	4.44	COMSOL solution time	15

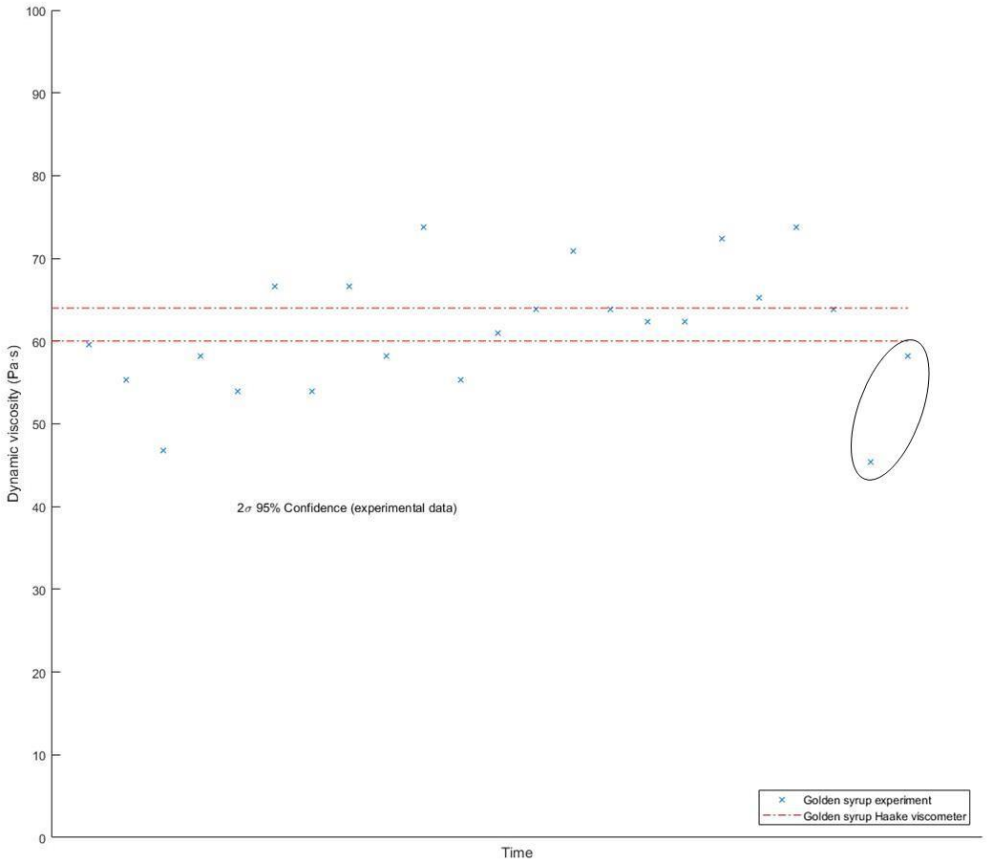

Figure 31. The confidence of the dynamic viscosity for each experiment performed through time. The two values inside the elipse show the drop in viscosity when fresh syrup was added to top up the reservior.

COMSOL simulation results for Newtonian fluid

COMSOL simulations were run to model each set of experiments using the independent variables h and β and the dependent variable μ, calculated using the analytical equation. Figure 32 and Figure 34 present the simulation results showing the velocity contours in 3D for a slice of the simulation and a 2D velocity profile. Figure 32 shows the velocity distribution inside the flow and not just at the free surface captured by Streams or calculated by the analytical solutiuon. The color changes show the change in velocity moving away from the low speed blue colored flow at the channel walls and peaking with the dark red colored flow at the middle towards the top. Figure 33 shows the shear rate in 3D for the COMSOL simulation. Shear rate

is highest along the centre of the channel walls but quickly drops towards the middle of the flow.

In Figure 34 the 2D velocity profile from the COMSOL solution is plotted on the same axis as the experimental data from Streams and the analytical solution from Takagi. The COMSOL simulation velocity profile is also a very good match for the Streams data. It exhibits the same near parabolic shape and a local maximum for u_{max} in the middle of the flow.

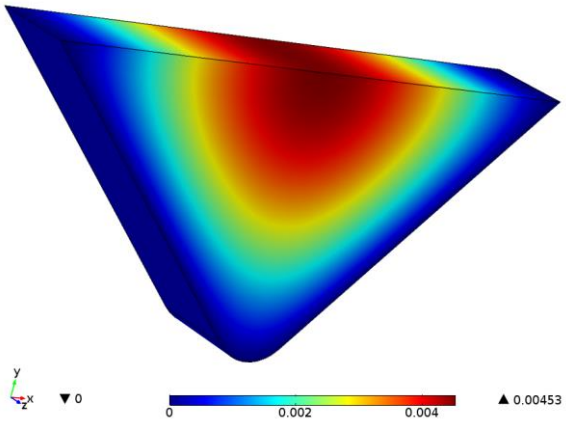

Figure 32. This COMSOL solution of experiment 26 shows the expected maximum velocity of 4.42 mm/s for a fluid 30.4 mm thick at an inclination angle of 7.8° and a dynamic viscosity of 58 Pa·s. The legend is a colour-bar of velocity ranges (mm/s) from lowest in blue to highest in red.

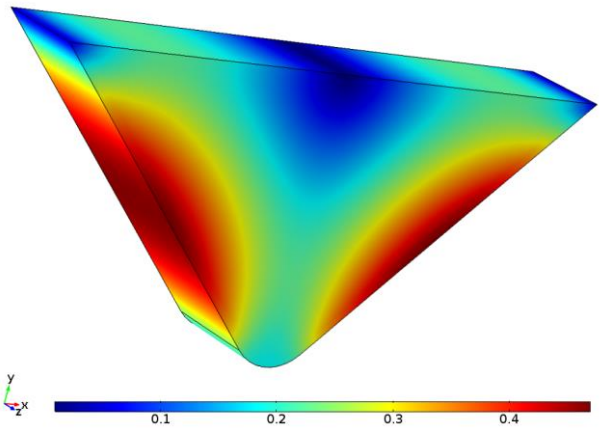

Figure 33. Shear rate is highest along the channel walls and reduces to a minimum at the top centre of the flow. This is reflected in the parabolic shape of the velocity profile seen in Figure 34. The legend is a colour-bar of shear rate ranges (s^{-1}) from lowest in blue to highest in red.

Figure 35 plots all 23 of the Takagi solutions against all the COMSOL simulations. The results are plotted in MATLAB and use a least squares approximation to fit the line (Figure 35). A Mean Absolute Error (MAE) was also calculated using the formula:

$$\frac{\sum_{i=1}^{n} \mathrm{abs}\,(y_i - x_i)}{n}$$

Where y_i are the experimentally measured maximum velocities and x_i are the COSMOL models predicted values. The MAE is a measure of a model's quality as it assesses how close the model's predicted value is to the actual value. The closer to zero the better the result. The MAE for this model was calculated to be 0.0032, which simply shows the equivalency of the two equations, or the limit of the numerical prescision of these methods.

As the Takagi solutions are analytical solutions to the Navier-Stokes equations there is a very good agreement between the two solutions. The small discrepancies for u_{max} might be explained by the fact that Takagi's solution ignores inertia and COMSOL does not.

For Newtonian fluids the COMSOL model performs very well at determining the viscosity from the free surface velocity. The Takagi and Huppert (2007) analytical solution is also a viable method for determining the viscosity for these types of non-Newtonian fluids in steady-state flow.

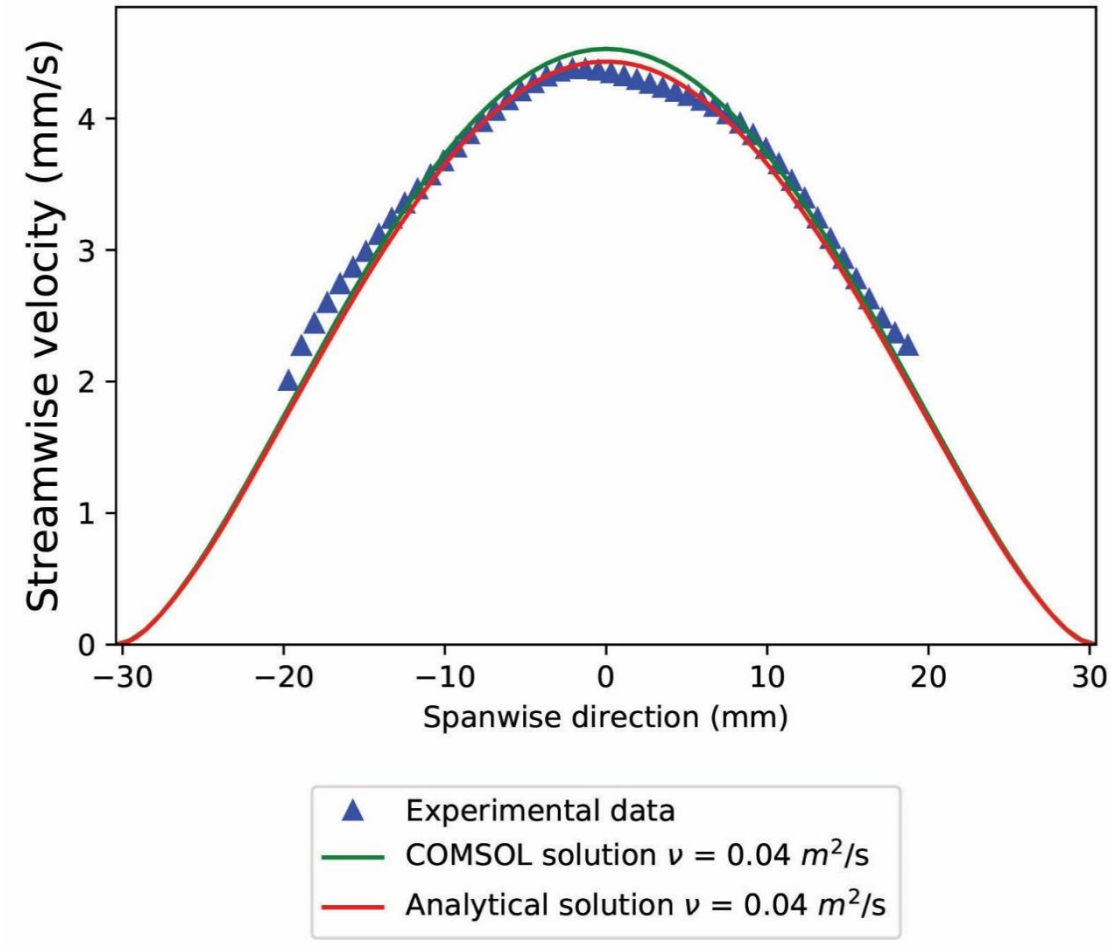

Figure 34. The three velocity profiles plotted on the same axis. The COMSOL solution is from the input parameters from experiment 19, as seen in Table 11, the maximum velocity magnitude is 4.42 mm/s.

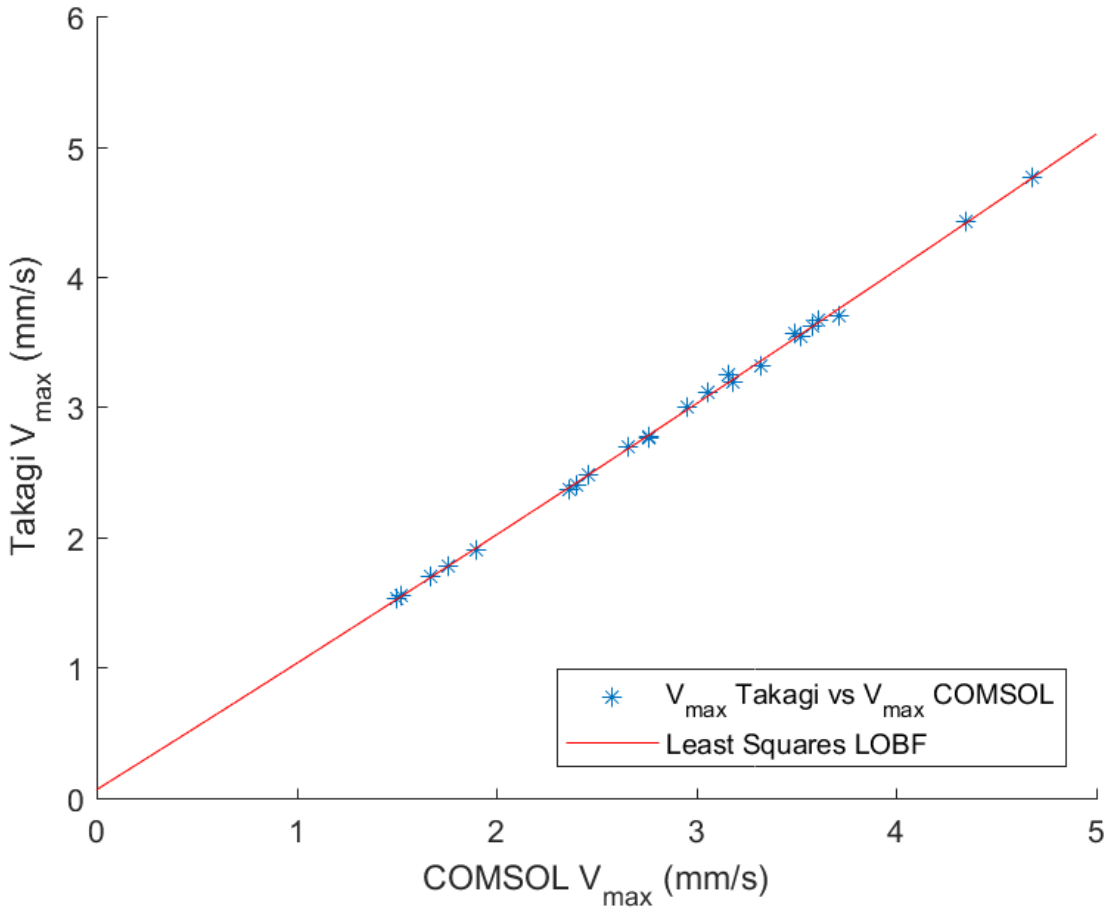

Figure 35. The COMSOL model (Navier-Stokes) simulations match the analytical solutions for each of the experiments.

Figure 36 summarises the results from the three methods. The mean and standard deviation of the experimental data is plotted against the refractometer and viscometer data. It can be seen that the experimental result mean value sits inside the upper and lower estimates from the viscometer.

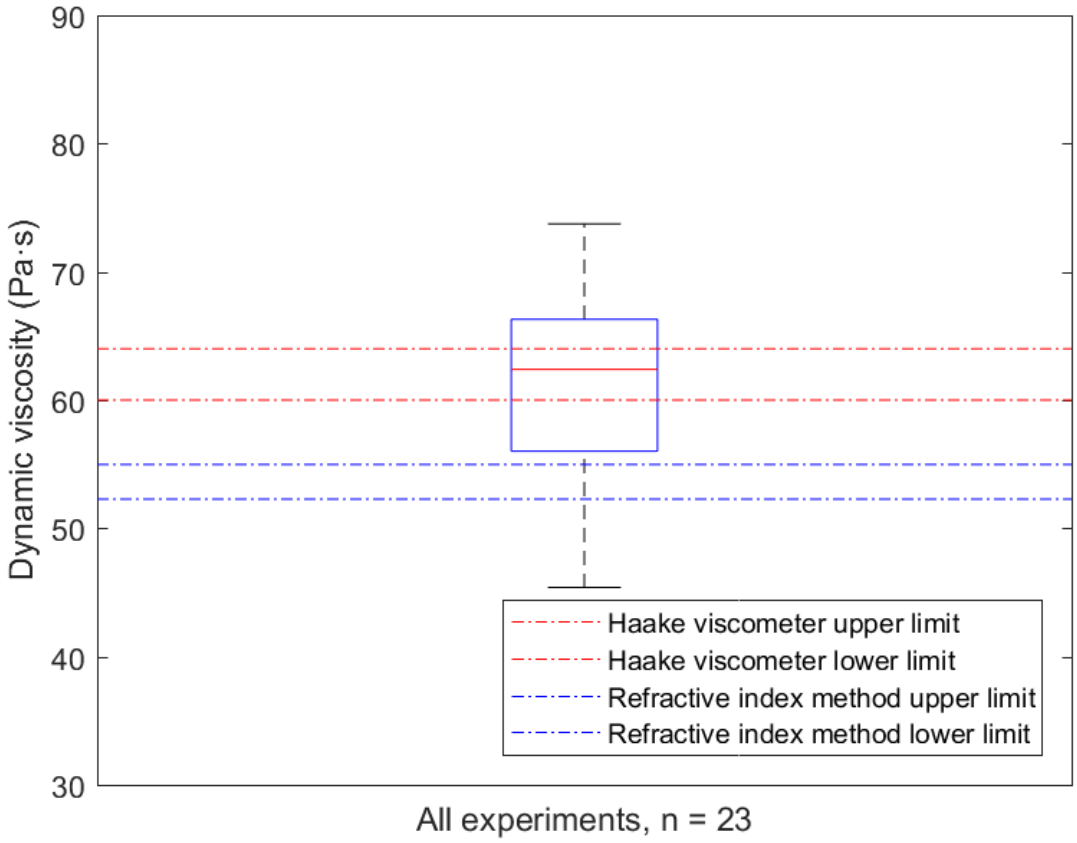

Figure 36. Over the n = 23 experiments performed on golden syrup the mean viscosity was 61 Pa·s with 95% confidence. The standard deviation is 7.7 Pa·s The Temperature was 20.7±.3°C

Sources of error, sensitivity and limitations for Newtonian fluid

Data collection

From Table 8 and Figure 36, we can see the three different methods have produced answers that are reasonably close. The calculation of viscosity from free surface velocity using velocimetry is successful. Some individual experiments, however, failed. Experiment numbers 1 and 2 were rejected because the data was collected before the flow was fully developed. This was visible as the flow had two different widths at the top of the video frame to the bottom. Experiment number 16 was rejected because the ruler was omitted from the video frame and there was no means to calculate the flow thickness. Numbers 27 and 28 were rejected because these two experiments were conducted a significant time after the previous ones and the viscosity had changed due to the climate control system dehydrating the fluid.

Quality of results

Figure 36 shows the standard deviation of all the experiments, and how they compare with the uncertainty measured by the Haake rheometer and the Atago refractometer. The refractometer measurement was difficult to read in the machine for reasons unknown. The viscosity from the refractometer method uses a fitted curve based upon observed results and the fluid measured fit just within the limits of the data previously examined. Perhaps the discrepancy resulted from a combination of temperature, impurities and the difficulty in reading the refractive index in the machine. The viscometer measured the results twice on one day within two hours so very little change in the fluid properties was allowed to occur, whereas the experiments took several days and more time was available for the results to be affected by the air conditioning. An increase of viscosity with time can be seen in Figure 31 as the values trend higher. The low viscosity of the last two experiments was due to a new bucket of golden syrup being added to top up the reservoir, thereby lowering the bulk viscosity. It appears that the fresh syrup has a lower viscosity that quickly changes once opened and allowed to evaporate some moisture and increase its relative crystal percentage. This is similar to the behaviour of lava in the sense that as lava cools, crystals start to form and increase its viscosity (Rowland & Walker, 1988).

Golden Syrup Properties over Time

As the experiments take time to complete, the fluid properties have time to change. The volcanic processes lab has a climate controlled environment that reduced the moisture content of the syrup with time once the golden syrup container had been opened. Figure 37 shows the crystals that grew in the syrup and the bubbles that become entrained within the fluid. The bubbles had the effect of lowering viscosity by reducing shearing stress. The paucity of the sucrose crystals and their tabulate shape meant they had negligible effect on the bulk viscosity of the fluid.

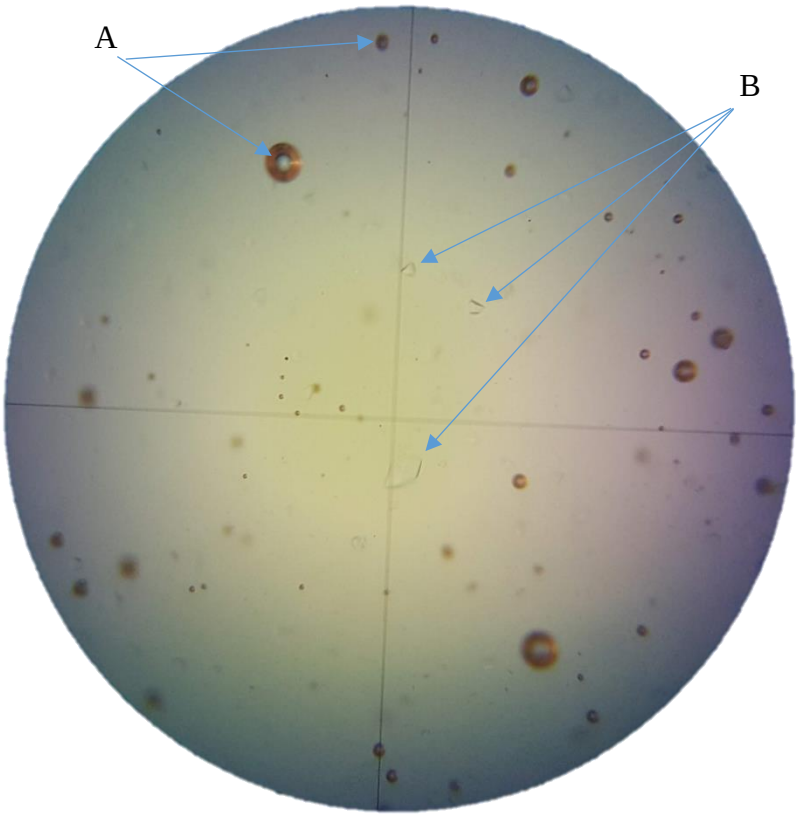

Figure 37. 10x Magnification of the Golden Syrup under a microscope in plain light showing air bubbles (A) and sucrose crystals (B). Bubbles sizes ranged in size from 0.001 mm to 0.5 mm. Bubbles can decrease viscosity by shearing and lubricating the flow at high strain rates, but at lower strain rates, they can increase viscosity by behaving like rigid bodies (N. Bagdassarov & Pinkerton, 2004). They can also change the flow to viscoelastic as they deform under increasing shear pressure but return to their original shape after the shear pressure is removed (Llewellin et al., 2002).

The dehydration of the golden syrup was, however, a problem. The initial container that was used for earlier pilot work was moved from a non-climate controlled room to a climate controlled room. During the early experimental work, it was noticed that the viscosity of the fluid was changing over time. Just a few days was enough to change the water content by 3.5% and the viscosity by an order of magnitude. It was then decided that a new container would be purchased and the experiments completed over as short a time as possible to alleviate these problems.

Parameter space

The parametric space that the experiments covered is shown in Figure 38. An attempt was made to cover as much of the space as possible within the confines of the experimental setup and feasibility. The lack of values at the high β, high h is because the experimental apparatus could not create a high enough flow rate to accomplish such conditions. Similar experimental constrains made it difficult to work with very low angles and low flow thickness. The final number of experiments after removing outliers and failed experiments was 23. In terms of the Buckingham Pi analysis done in the methods section, this is short of the 32 experiments suggested previously. This effectively means instead of 5 variations per independent parameter (2^5), it was, $log_2(23) = 4.5$ which is still an acceptable number of experiments to measure a single fluid's viscosity.

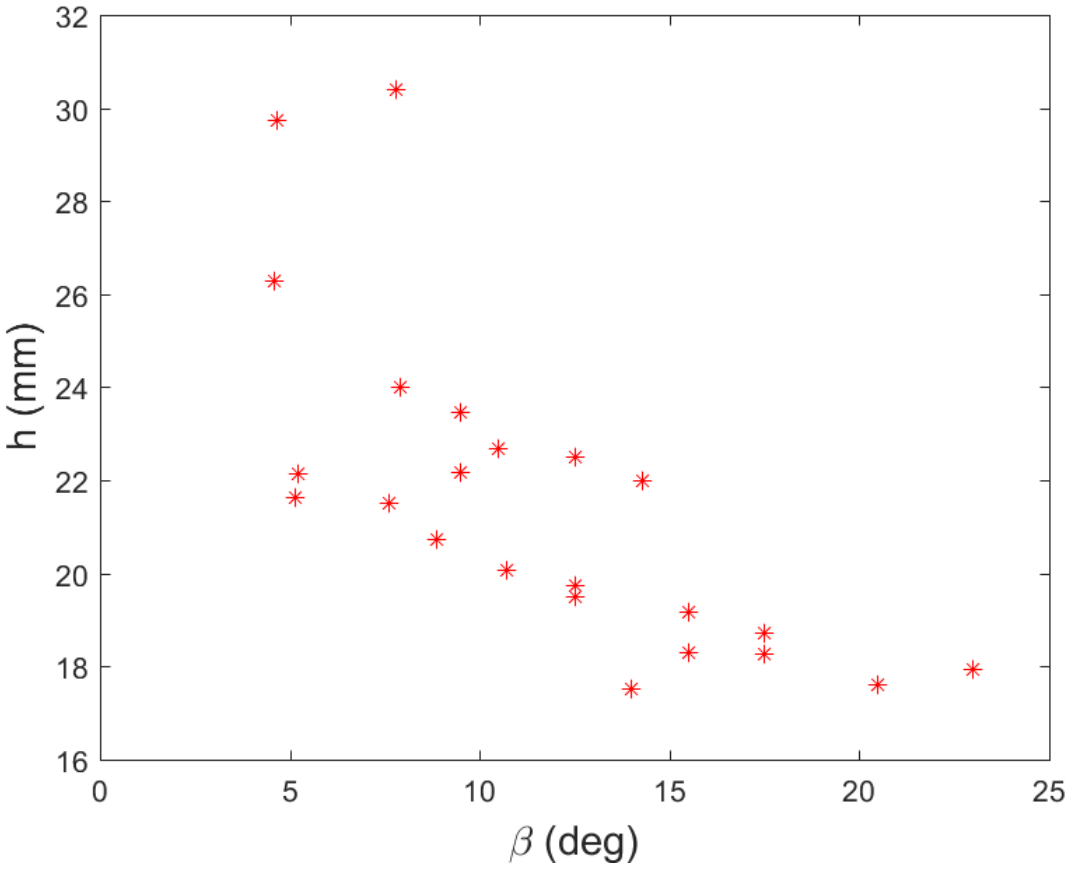

Figure 38. Parametric space of independent variables. Red stars are the independent variable pairs.

COMSOL model factors that influenced the results

Independent variables

From Appendix V h vs experiment the expected result would be no change in viscosity for changes in flow depth as the viscosity is uniform and constant. Variation here is most likely due to difficulty in correctly determining the flow depth. A reverse dipstick was used and the depth was also derived from the video using the relationship depth = half the width. Both methods gave answers that varied by 1.0 to 1.5 mm so an average measurement error of ± 1.5 mm is used. The bottom of the V channel was rounded and this 'fillet' had to also be accounted for. The average value between the two methods was used for the final flow depth. Figure 64 and Figure 63 in Appendix V show no special correlation between these two variables, which is to be expected. Any experimental bias would be seen here. The variation here is most likely due to procedural errors in the measurements of β, which was determined by repeated measurements to be ± 0.5° the error in measuring h and the influence of ghost particles in the video analysis. It is also important to note that the relative percentage of the error in measuring h is perhaps greater for shallow flows than it is for the deeper ones, creating a bias of less accurate results for shallower flows in these experiments. This is seen in Appendix V, Figure 63 as the spread of results around the mean is greater at the lower depth values than it is at the higher values. Tenuously, it could be suggested that viscosity was easier to predict for higher beta angles than lower ones as the results are clustered slightly closer to the rheometer values at higher angles. Flow height appears not to have any correlation with the accuracy of determing the viscosity. This could be interpreted as flow thickness is free from introducing bias beyond the ability to accurately measure it.

The biggest challenge during the experimental procedures was the accurate measurement of h, flow depth. The two methods used showed differences of up to 7% between the image method and the reverse dipstick method. Using a dipstick alters the flow behaviour as the flow is deflected around the dipstick and the free surface is deformed as the dipstick penetrates it. A reverse dipstick attempts to measure from a datum line that is a known distance from the V channel bottom down to the flow without touching it.

Sensitivity of independent parameters

While the relationship between h, β and u_max was examined in the methods section of this thesis, the impact of the uncertainties of measuring these parameters can now be clearly seen. From Figure 39 and Figure 40, it is seen how much the flow speed varies with height and inclination angle, and just how great an effect a small change in height has on flow speed. This could be interpreted as the main source of uncertainty in this method of determining viscosity. In the field around volcanoes, practical measurements of lava flows will have the same problem. If the uncertainty in the flow thickness can be determined then that uncertainty can be reflected in the presentation of the final viscosity. The red lines represent the ±1.5 mm uncertainty in measuring the flow thickness.

In Figure 40 the red asterisk represents the value obtained in experiment number 8 of a fluid 26.7 ± 1.5 mm thick at an inclination angle of 10.5 ± 0.5° and a Streams derived viscosity of 53.9 Pa·s. Dotted red lines indicate the uncertainty in measuring h and β. The value of the velocity is therefore contained within the area bounded within the rectangle e.g. 3.1 - 4.3 mm/s. This clearly shows the sensitivity of velocity to height and inclination angle as a 1.5 mm increase in height and 0.5° increase in inclination angle leads to a 1.2 mm/s change in velocity. Height has the greatest impact on the uncertainty of velocity as can be seen from the change in shape of the velocity curves as β increases. Therefore, it is of vital importance to accurately measure these two variables and special care must be taken to measure h.

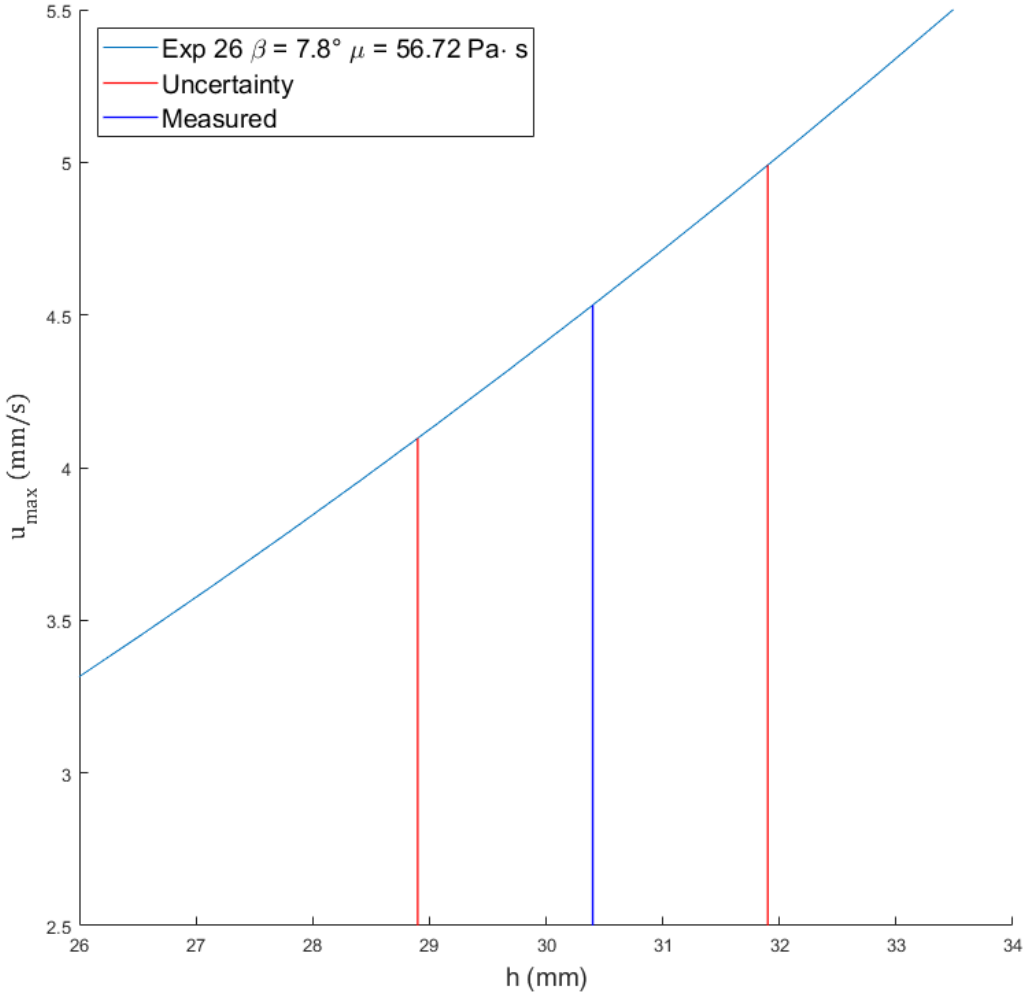

Figure 39. This figure uses Experiment 26 as an example to show that the expected change in velocity over a 12 mm range in h is about 4 mm/s.

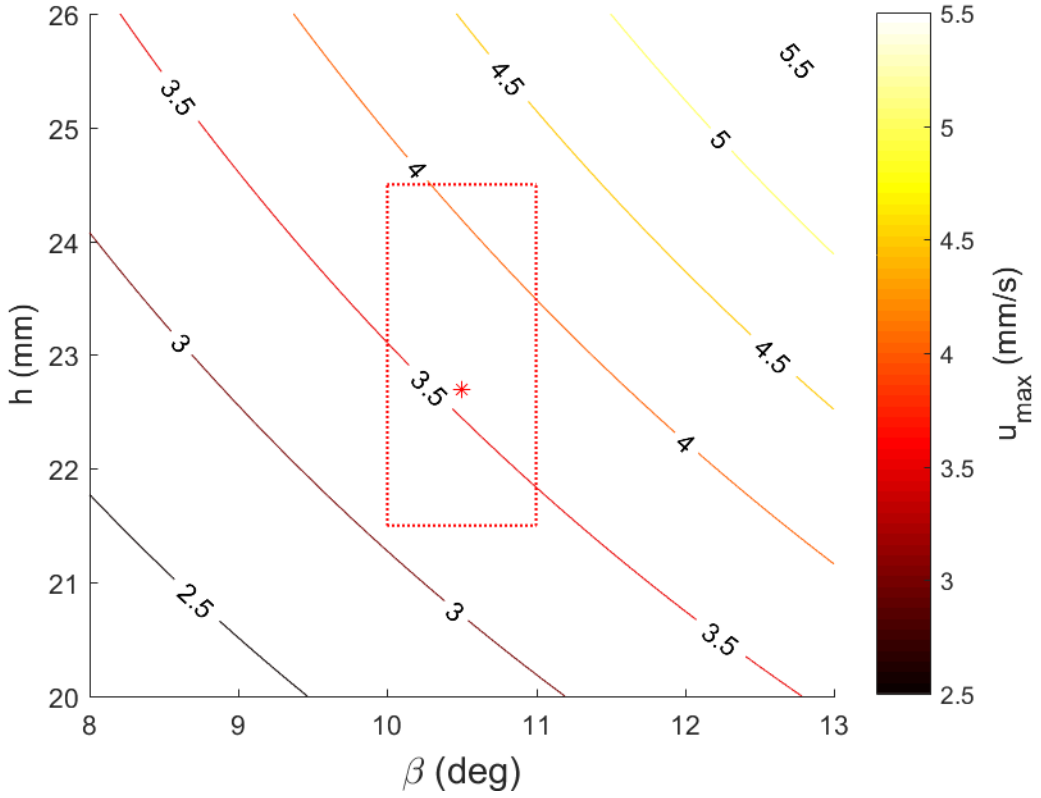

Figure 40. This contour uses the analytical solution to show the range of expected velocities where $8° \leq \beta \leq 13°$ and $20 \leq h \leq 26$.

Temperature

Viscosity is certainly temperature dependent and the goal of these experiments was to control temperature to simplify the model. The experiments were performed initially in a non-air conditioned room before an unrelated incident caused the apparatus to be moved to a new location. This changed the fluid's temperature as the ambient temperature in the new lab at ground floor was different to the sun exposed 6th floor room the experiment was previously set up in. To control for this, the experimental data collected prior to the move was abandoned and the experiments redone. Temperature of the fluid and the surrounding air was measured during each experiment and the average temperature was determined to be $21° \pm 0.4°C$. This value was also used by the rheometer when calculating viscosity.

Chapter Four: Results: non-Newtonian fluid

This section presents the results from the experiments using a non-Newtonian fluid alongside the results of the COMSOL non-Newtonian simulations. There is no refractometer solution for this fluid and there is no analytical solution for non-Newtonian fluids either. Hence, the rheometer result will be presented against the COMSOL simulations. The simulations will use the free surface velocities from the experiments.

Carbopol® 980 polymer was chosen to be the non-Newtonian fluid analogue. It is a shear thinning fluid and its viscosity is easily adjusted to a suitable range for experimentation. The Carbopol® polymer was prepared as per the method outlined in the Appendix III Preparation of Carbopol® polymer 980.

The same experimental setup was used for the Carbopol® as was used for the golden syrup experiments. The same procedures were followed with the recording of data, seeding the surface with polystyrene beads and post processing of the data.

Two methods were used to calculate and compare the viscosity of the Carbopol®:

1. Anton Paar MCR302 rheometer in the CAPE laboratory.
2. Particle tracking velocimetry from experiments with COMSOL simulations.

Non-Newtonian fluid - Anton Paar MCR302 rheometer result

A sample of the fluid was collected after two experiments and taken to the CAPE laboratory for analysis. The Anton Paar MCR302 rheometer was used to analyse the Carbopol® not just to confirm its viscosity but also to determine its other rheological properties.

There is no single value to describe viscosity in a non-Newtonian fluid because its viscosity is shear rate dependent. The results are presented in Table 12 and plotted in Figure 41. It can be seen there is no significant hysteresis in the fluid and that Carbopol® is a shear thinning fluid. The log shaped curve shows shear stress initially increases rapidly with a small change in shear rate, followed by a long tail where shear stress continues to grow but at a reduced rate.

Figure 41 is the full set of results that spans much higher shear rates than the experimental data set. The line of best fit is an attempt to mathematically fit a power curve to the data points. It can be seen that it is not a perfect fit to the data and fails to capture the behaviour of the fluid at low shear rates, which could be because the power law model is forced through the origin. A Herschel-Bulkley fluid, for example, has a yield stress and so the y intercept is not zero. It can also be seen that the power curve diverges from the rheometer data as shear rate increases.

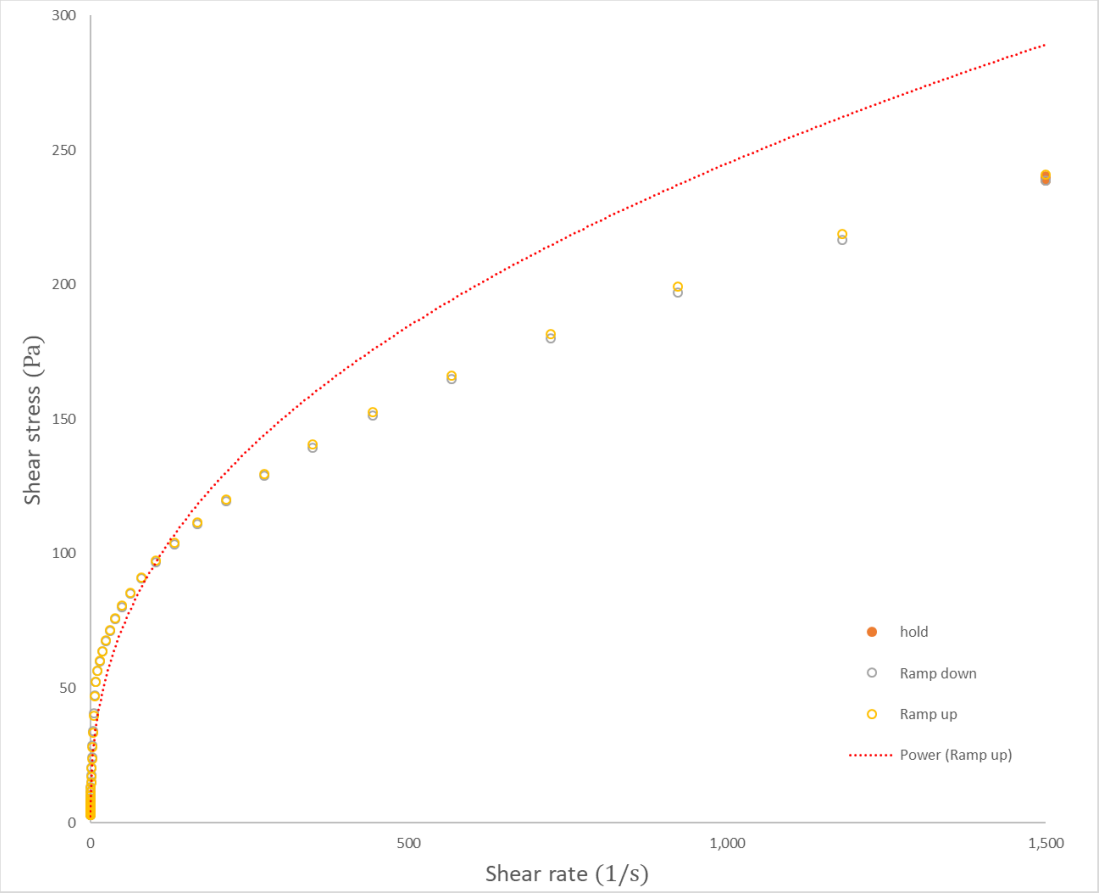

Figure 41. Carbopol® analysed in the Anton Paar rheometer and the corresponding fitted power curve (red line). The three plots sit on the same paths indicating no hysteresis in the fluid at low shear rates. The power law equation for the line of best fit (LOBF) of the ramp up sequence of data is: $\tau = 14(\dot{\gamma})^{0.4}$. The hold plots at maximum shear rate.

Table 12. Abridged raw data from the Anton Paar Rheometer showing the ramp up phase to a shear stress of 17 Pa, data was collected at 21.7°C

Point No.	Shear Rate	Shear Stress	Viscosity
	(1/s)	(Pa)	(Pa·s)
1	0.0101	3.0522	304
2	0.0128	2.9260	229
3	0.0163	2.9856	183
4	0.0208	3.1134	150
5	0.0265	3.2803	124
6	0.0338	3.4791	103
7	0.0431	3.7173	86.3
8	0.0549	3.9912	72.7
9	0.0700	4.3029	61.5
10	0.0893	4.5724	51.2
11	0.1140	4.9304	43.3
12	0.1450	5.3896	37.1
13	0.1850	5.9275	32
14	0.2360	6.5406	27.7
15	0.3010	7.2410	24
16	0.3840	7.9941	20.8
17	0.4900	8.9088	18.2
18	0.6250	9.9953	16
19	0.7970	11.307	14.2
20	1.0200	12.894	12.7
21	1.3000	14.818	11.4
22	1.6500	17.171	10.4

Non-Newtonian fluid experimental results

Data was collected and processed the same way for the non-Newtonian fluids as the Newtonian syrup, only the modelling and simulations were different. Five experiments were performed with as much variation in β and h as could be achieved as per Table 13. Once the data was processed through Streams the velocity field values were imported into COMSOL and interpolated into the curve seen in Figure 42. This curve has a distinctive flat nose and steep

sides. This suggests the flow is moving more like a plug in the centre and the shearing is predominantly happening on the edges.

Table 13. Data recorded during experiments with Carbopol® Experiment 5 was discarded as β was changed during the experiment and not enough time was given for re-equilibration.

Experiment number	**Pixel ratio**	**Offset [mm]**	**Beta angle β °**	**Flow width w [mm]**	**Flow height $h = \frac{w}{2-fillet}$ [mm]**
1	985/100	33.5	13	67	33.5
2	938/80	30	15.5	60	30
3	941/80	27.5	18	55	27.5
4	**939/80**	**30**	**20**	**60**	**30**
~~5~~	**939/80**	**34**	**9**	**68**	**34**

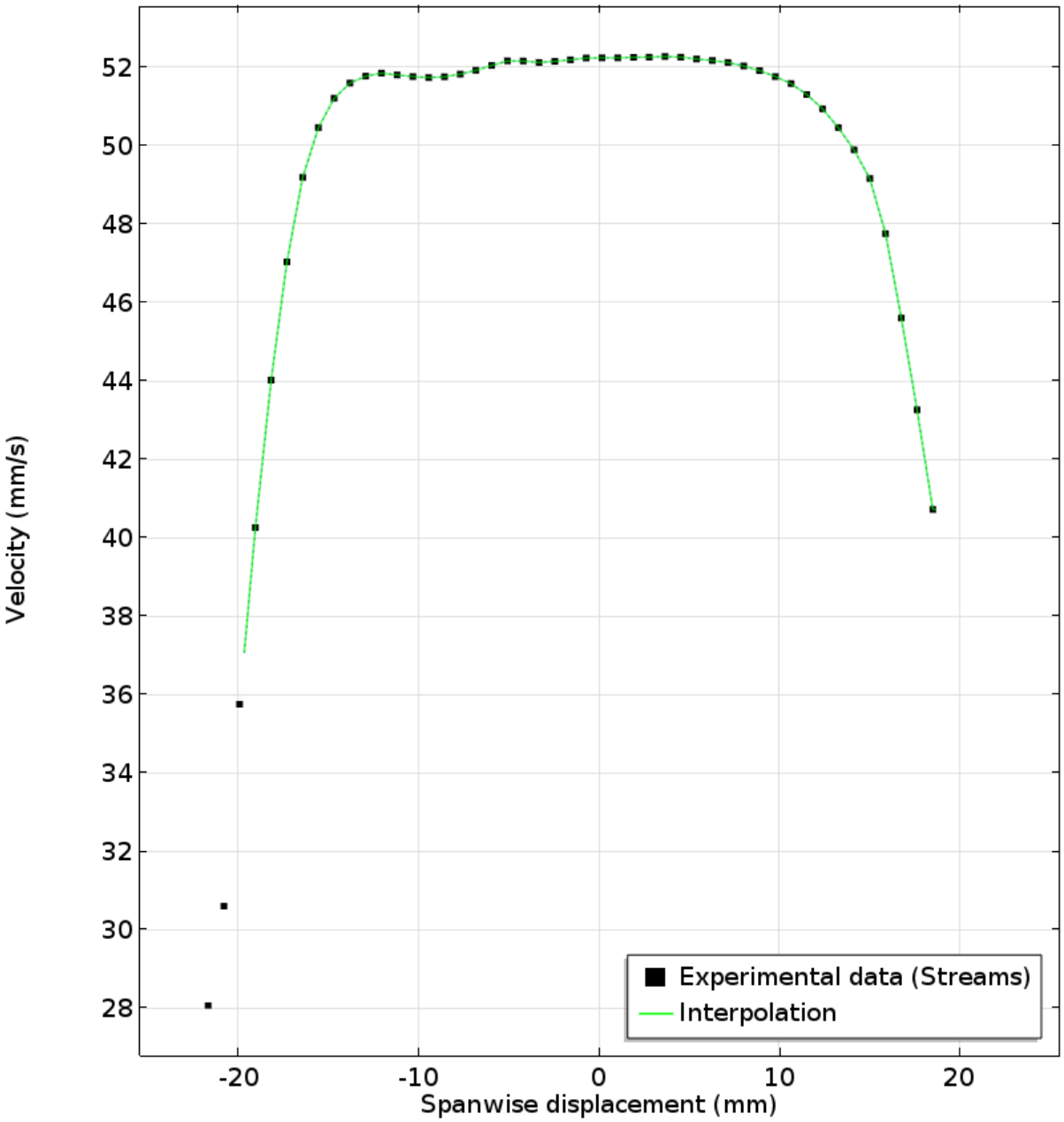

Figure 42. Streams data has been imported into COMSOL and the interpolation is mapped across the data points.

Non-Newtonian fluid COMSOL simulation results

The COMSOL model is configured as described in the methods section and the simulation results are then displayed over the top of the experimental data for comparison Figure 43. The two curves match well in the plug flow area but the experimental result has a paucity of data in the edges of the flow close to the channel walls. This is due to problems similar to the golden

syrup experiments as previously discussed. The visible trend, however, is a sharp reduction in velocity beyond the plug section, as the flow approaches the channel walls.

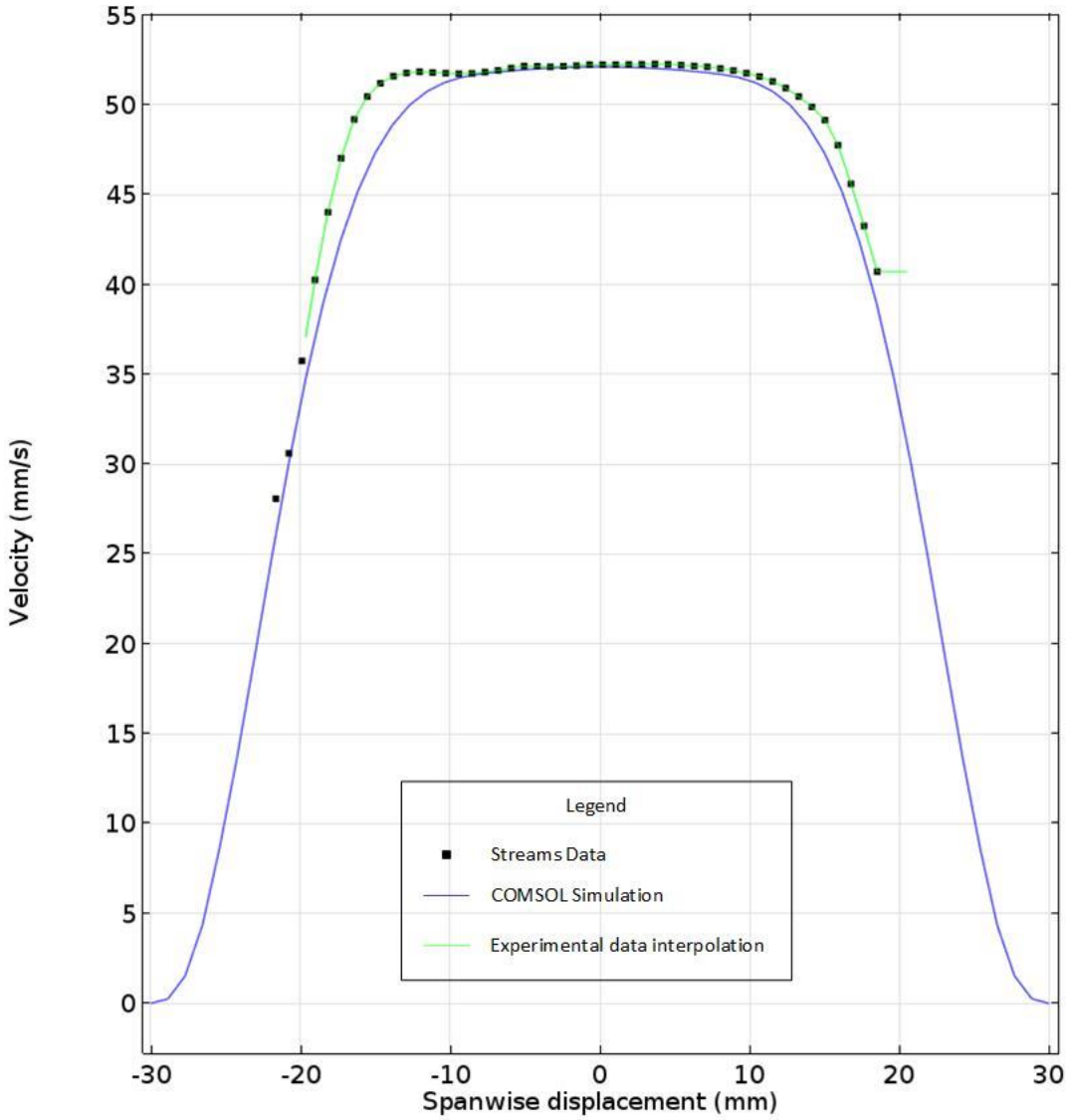

Figure 43. Streams data for experiment number 4, with an overlay of an interpolation curve and COMSOL simulation.

Viscosity is plotted against shear rate to allow for comparisons with the Anton Paar rheometer data and show the simulation's predicted values of viscosity to test the model.

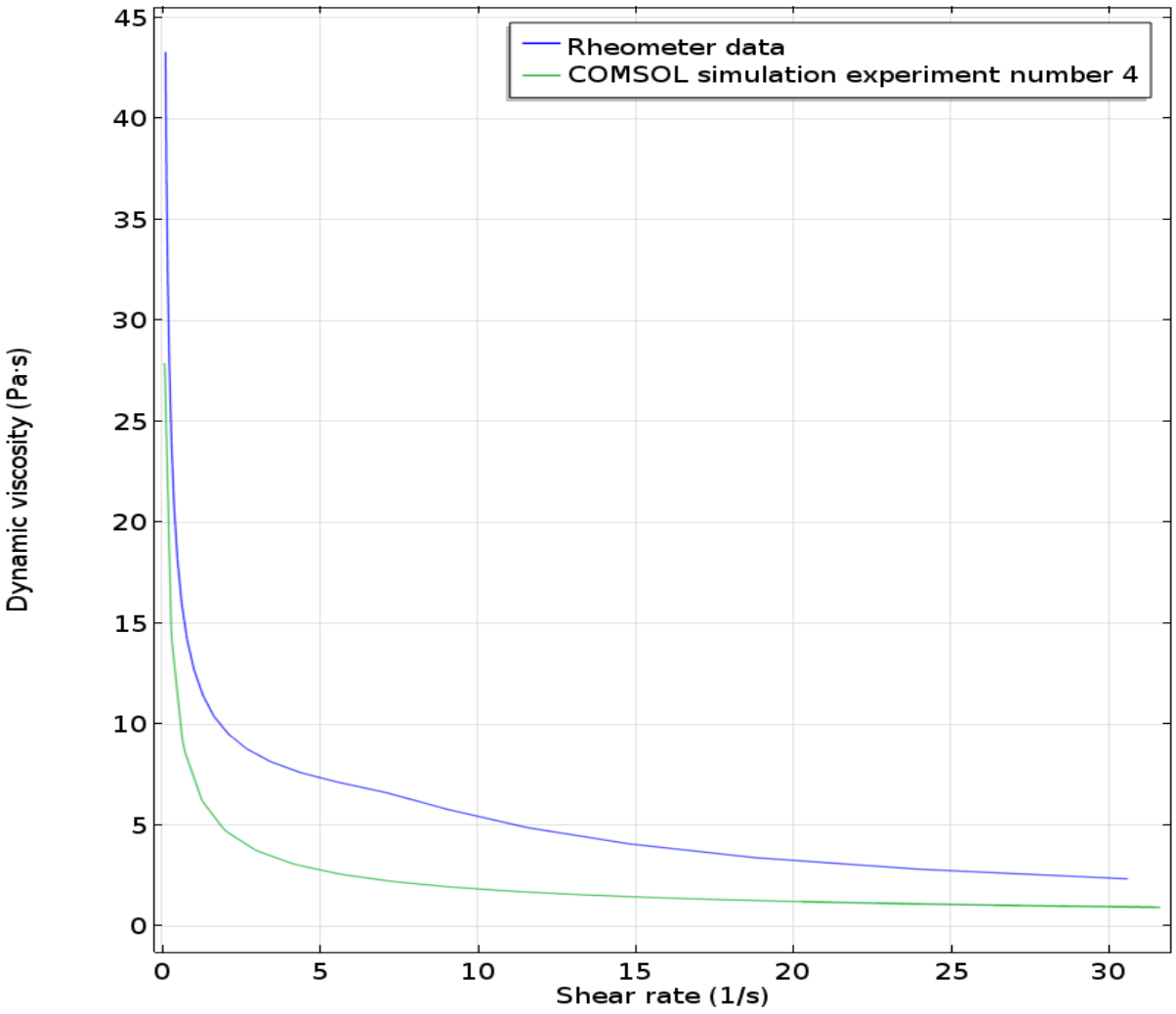

Figure 44. COMSOL simulation of experiment number 4 dynamic viscosity plotted against shear rate with Rheometer data overlay in blue.

The goal of the experiment was to fit the free surface velocity data collected onto that of the COMSOL simulation by varying k and n, the two coefficients that describe the power law (**Eq. 9**) restated here:

$$\mu = k(\dot{\gamma})^{n-1}$$

The derived values of k and n vary between 20.5 – 22.8 for k and 0.19 - 0.22 for n. It is also seen in Figure 44 and Figure 47 that, while the power law curve fits the rheometer data well in the range of shear rates, $1 < \dot{\gamma} < 3$ it does not entirely match the behaviour of the Carbopol® at lower shear rates, $\dot{\gamma} > 1$. The reason that the experimental data is not a perfect match to the model at low shear rates is likely due to the experimental limitations of collecting

data at the low end of the shear rate regime. Or possibly it means that there is a yield stress to be overcome.

We can also use the COMSOL model to view the velocity field in 3D. Figure 45 and Figure 46 show that the strain rates and shear stress are highest along the boundary of the V channel wall and then drop off quickly perpendicular to the wall towards the centre of the flow. This is intuitive as the walls are no slip and the velocity tends to zero at the boundary. This is the area that is poorly served by the data collected from the experiments. This also explains the flat nosed shape of the flow. The dark blue area of Figure 46 is behaving like a plug, a region that is flowing without any shearing between its adjacent layers. As the shear rate increases away from the boundaries the simulation curves start to fit with the shape of the Anton Paar rheometer curve.

It is also worth considering that the power law is not the best fit for the Carbopol® and that Herschel-Bulkley might be more appropriate if the fluid does have a yield stress on top of its strain rate dependent viscosity. As the Herschel-Bulkley equation has three unknowns, however, it was not attempted to try fitting it within the scope of this research project.

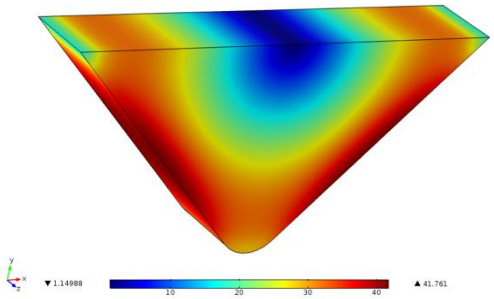

Figure 45. A COMSOL simulation of experiment number 4 showing the effect of Shear stress.

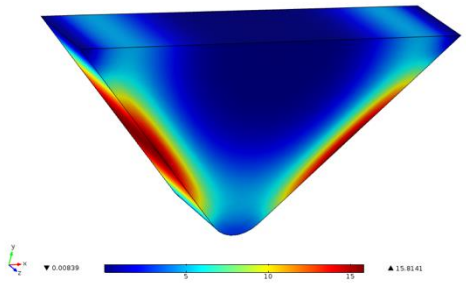

Figure 46. A COMSOL simulation of experiment number 4 showing the effect of strain rate at the boundary walls on the flow. The colour bar shows the maximum strain rate was 15.8 s^{-1}

Figure 47 shows the relationship between viscosity and strain rate. By interpolation of the experimental data and using the mean of the four experiments the averaged distance between the two curves was calculated. The result is very close to the commercial rheometer ($\dot{\gamma} = 1, \mu_{experimental} = 19\ \text{Pa} \cdot \text{s}\ \mu_{Rheometer} = 13\ \text{Pa} \cdot \text{s}.\ \sigma = 5\ \text{Pa} \cdot \text{s}$) for strain rates between 1 and

$3\,s^{-1}$. Commercial rheometers excel at low torque measurements compared to the experimental method of using beads on the free surface of the flow. Commercial rheometers, however, cannot be carried out into the field and used with lava flows, although some, e.g. Chevrel et al. (2018) have tried.

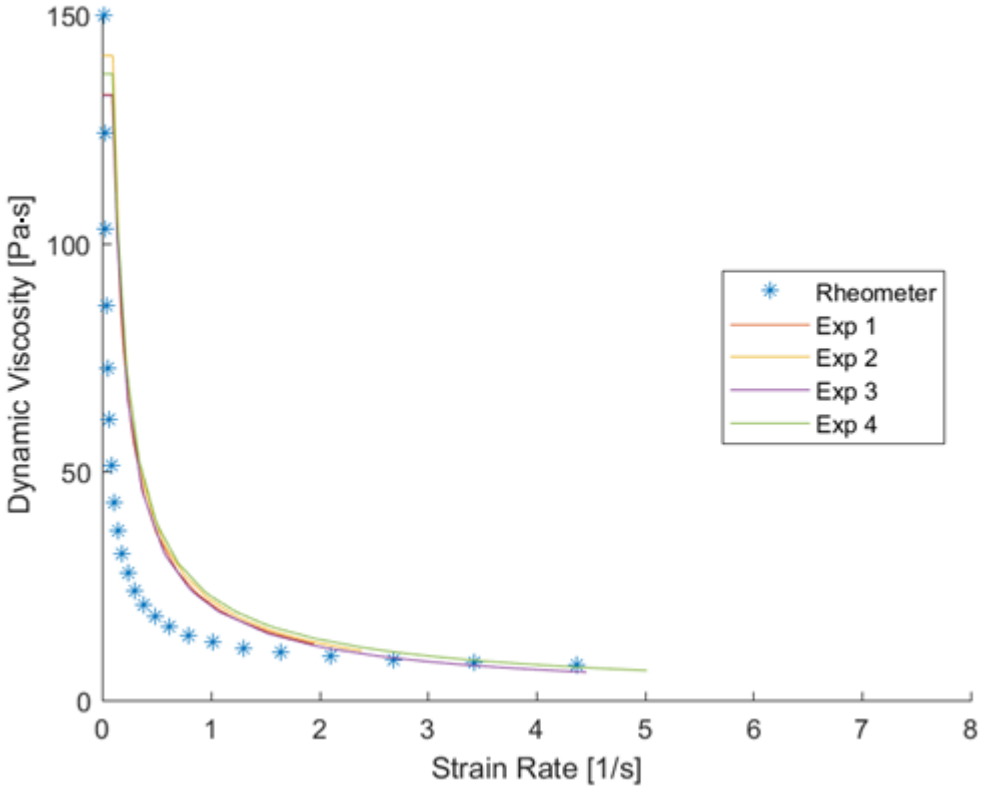

Figure 47. COMSOL model data plotted against the Anton Paar MCR302 Rheometer data.

Experimental sources of error

The beads used in the experiments need to have a minimum size to be detected by Streams and that affects the resolution of measurements at the edges of the flow where it is easy for the beads to adhere to the sides of the channel or catch on surface features. With a few more modifications to the experimental methodology these results could be further improved. Specifically improving the determination of the flow thickness as the shear rate varies with height would increase accuracy. Investigating smaller bead sizes and minimising interference from beads sticking to the channel walls would also greatly increase the efficacy of the results.

Carbopol® turned out be a difficult fluid to work with. Initial attempts failed when the viscosity was too high, or it simply did not have a high enough stress to exceed the yield stress. After trial and error the right consistency was achieved and some data collected. Again because of the climate control in the lab it was decided to do as many experiments on one day and to test the fluid on the Anton Paar rheometer as close to the experiments as possible. This was to avoid any dehydration occurring or the solution becoming contaminated.

The Carbopol® polymer is naturally a clear gel and it was difficult to get contrast with the fluid and the V channel so a dye was added to it with limited success. As the fluid had a tendency to slip down the smooth stainless steel V channel, an acrylic channel was used. This channel was lined with a high friction tape to prevent slipping on the boundary walls. This introduced new problems as light was reflecting off the gap between the tape strips at the bottom of the channel. Tweaking the contrast brightness ratios in VeeDub helped reduce this problem.

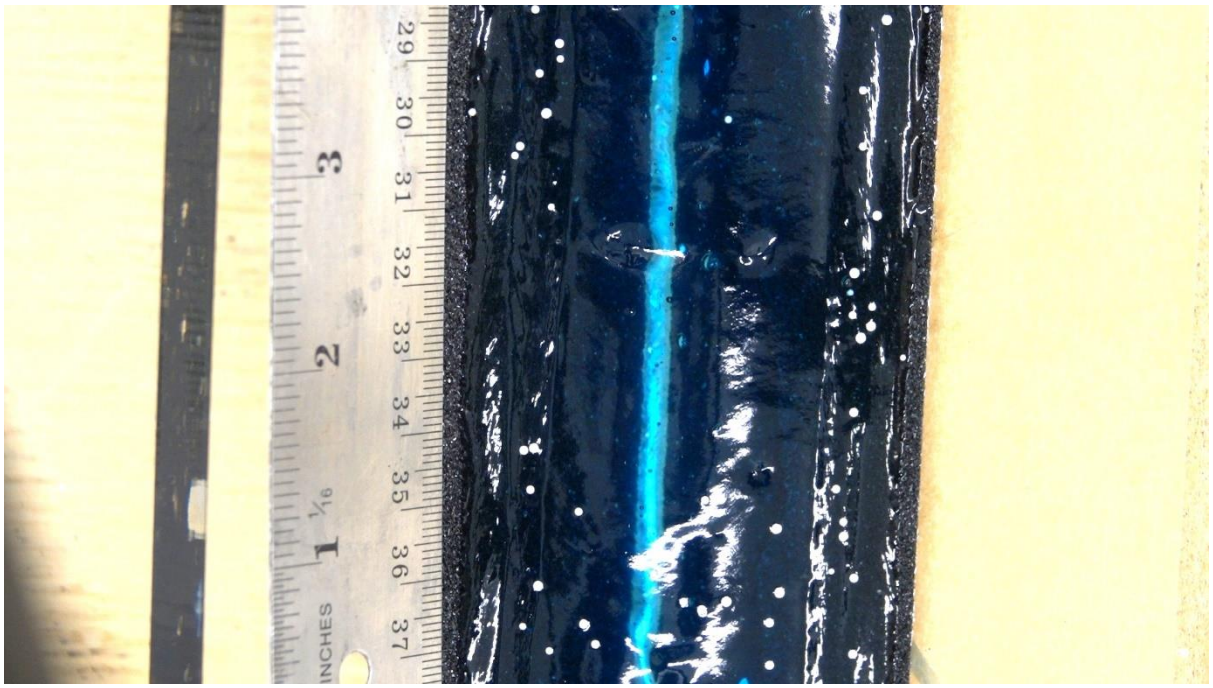

Figure 48. Carbopol® solution flowing down the channel; note the roughness of the surface and the irregularity of the boundaries. The light blue strip down the middle made it difficult for Streams to identify the tracking beads.

The free surface of the flow was affected by surface tension more than the golden syrup was so the surface was rougher (Figure 48) and sometimes it was difficult to determine the edges of the flow accurately.

Chapter Five: Discussion

Based on the results presented here, Figure 36, Figure 45 and Figure 47 this model represents a solid foundation upon which to build a more developed and complete method for rheology identification. If this work can be extended to use the heat equations similarly to Lev, et al. (2012), then it should be possible to overcome the limitations of using an analytical solution and allow the equations to be applied to a range of geometries and viscosities. Also using the entire velocity field, as part of an objective function based on the integral of the velocity curve, is perhaps more accurate than simply matching the maximum velocity of the flow as it captures the potential to match the different types of velocity profile, i.e. the flat nosed plug flow seen with the Carbopol® and observed in some lava flows (see Figure 50).

The methods described here successfully derived the viscosity of Newtonian fluids within acceptable margins of error. These methods are relevant to scenarios where the viscosity and strain rate of real lava flows allow its behaviour to be approximated in a Newtonian manner. With the input of density, flow thickness and slope angle and using the free surface velocity, the viscosity can be calculated using the COMSOL model. The intention was to control the dependent variables u, μ, however, due to environmental factors, uncontrolled variance in the viscosity of the golden syrup was seen in the experiments as the syrup's properties changed with time. In other words, the experiments were sensitive enough to detect the small changes in viscosity from dehydration. This was evident from the final rheometer test that showed the viscosity of a freshly opened tin of syrup was ≈ 26 Pa·s and that jumped to an average value of 61 Pa·s over the time the experiments took, see Figure 49. Re-examining the data from Table 10 after the rheometer test it was seen that the first experiment on the syrup recorded a viscosity of 26.9 Pa·s. This is considered an outlier in the final results but does appear to be the same result as the rheometer. Therefore it appears that the fluid viscosity is time dependent starting at 26 Pa·s and ending at ≈ 62 Pa·s over the course of the experiments.

The results of the non-Newtonian fluid simulations are very encouraging. They have shown that the model is capable of capturing the non-linear relationship between viscosity and shear rate. The comparison of the simulation solution and the rheometer are close. The differences could be due to evaporation. If the golden syrup could be affected so dramatically by the humidity controls in the laboratory then it is not difficult to imagine that the Carbopol®, which

is ~90% water is also affected. The Carbopol® was tested six days after the experiments were completed, plenty of time for its properties to change.

What is important is that the model was able to capture the plug shape of the flow, which is an effect seen in lava flows. In Figure 50 the dark region in the middle of the lava flow is the plug flow region, while the highest shear rates are the bright orange areas at the channel walls, where a crust cannot be sustained.

This is important because others have shown that lava rheology is not always consistent, and as such it varies depending on volatile and crystal content, and temperature. In their use of a portable viscometer at Mt Etna, Pinkerton and Sparks (1978) found the rheology of the 1975 Etna lava to be a pseudoplastic non-Newtonian fluid with a measurable yield strength. Chevrel et al. (2018) used a similar device on Kilauea's Pu'u ‘$'\bar{O}'\bar{o}$ eruption and fitted a power law to their strain rate, shear stress data.

The shear stress measured with the Carbopol® was in the range of 10 to 40 Pa (Figure 45) and in their data, Chevrel et al. (2018) were measuring much higher shear stresses in the order of 800 to 1900 Pa. Creating a new mixture of Carbopol® that had a shear stress in this range would allow for a better test of the model against real lava rheological data.

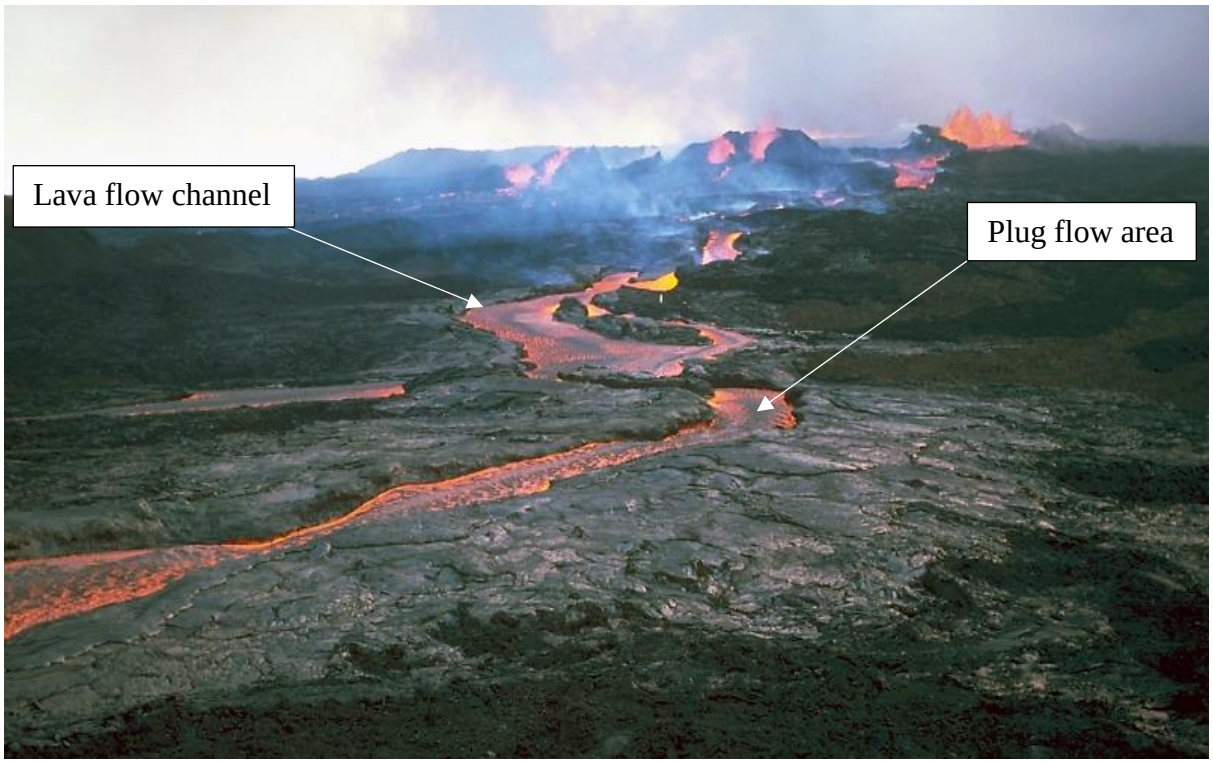

Figure 50. A‘ā lava flows from the Mauna Loa 1984 eruption. Lava flow is channelized in the foreground. Fissures of curtain lava are visible in the background. The dark crust like areas in the middle of the channelized flow are the plug flow regions. Public domain image by R.W. Decker modified by the author.

Limitations and future challenges

The rheology identification method does have some limitations. The flow is assumed to be in steady state for the model which is only applicable to select periods of natural lava flows with constant effusion rates, high temperatures, and low viscosity lava flowing in channels similar to the one in Figure 50.

It was also shown that the model is sensitive to flow depth, h. Uncertainty in the measurement of h will lead to errors in the derived viscosity. Measuring flow depth is difficult, and using pre-eruption terrain models may be ineffective due to thermal erosion on the channel bottom, where hot lava erodes the bottom of the channel and deepens it over time. See both Kereszturi and Hargitai (2014) and Williams (2004) for a discussion about thermal erosion. Most methods used to calculate flow thickness depend on some knowledge of the terrain before the eruption. They then use surface from motion techniques to build 3D models of lava flows. Another method tested by Naranjo et al. (2016) used Radar-interfero-grammetry to determine flow

thickness but this technique requires a satellite to take the images. Terrain models are improving with the use of aerial imaging from helicopters and drones, e.g. Biass et al. (2019), Patrick and Orr (2018). Some work on direct measurement of flow thickness *in situ* was done by Kauahikaua et al. (1998) in Kilauea. They used rebar to probe the bottom of lava tubes through skylights to determine flow thickness with an accuracy reported to be ± 0.1 m.

Adding topography

Another extension to the model would be to replace the flat surface of metal in the V channel with a channel built from the same material as found on volcanic slopes. Initially, 3D scans of small channels could be used with 3D printers to build accurate scaled down lava channels with levies and then analogue fluids to examine their behaviour. This has already been explored by Rumpf, Lev, and Wysocki (2018), who found surface roughness had a profound effect on flow velocity (up to 50% reduction in velocity). Hot lava can also be poured down inclined surfaces seeded with obstacles to enable their effects on the free surface flow to be observed as has been investigated by Dietterich, Cashman, Rust, and Lev (2015).

The effects of crust

This work has focused on free surface velocity, but as lava cools a crust develops (Calvari & Pinkerton, 1999). Our work is only relevant to scenarios where there is little or no crust if the crust is coupled to the flowing lava. If the effects of the crust are to be considered, there is no longer a free surface and the flow between the molten lava and the solidifying crust would have to be modelled differently as the flow would be more akin to pipe flow with a potentially moving upper surface. Measuring flow speed beneath a crust without being able to observe is a significant challenge for a fluid over 1200°C. The crust also acts as an insulator; Thordarson and Self (1998) found cooling rates of <0.1°C/km in the Roza eruption, although this is most likely an extreme end member due to the sustained duration of eruption and the volume of lava erupted, which was 1300 km^3 over 12 years.

Use real lava

As the University of Canterbury has now completed the upgrades and commissioned the furnace, this work can continue using real lava in place of analogues. Although smaller in scale to the Syracuse University facility in New York, it is much more readily accessible and experiments can be done in days rather than with months of planning. This allows for rapid prototyping and experimental procedure development to generate new datasets.

Adding the heat equations

Enabling the model to incorporate the effect a changing temperature has on viscosity is a vital step towards making this a complete model of lava flow. The heat equation has the general form for a function: $T(x, y, z, t)$

$$\frac{\partial T}{\partial t} = \alpha\left(\frac{\partial^2 T}{\partial x^2} + \frac{\partial^2 T}{\partial y^2} + \frac{\partial^2 T}{\partial z^2}\right)$$

And the radiation boundary condition is:

$$-\hat{n} \cdot \vec{q} = \varepsilon\sigma\left(T_{ambient}^4 - T^4\right)$$

Where, α is the thermal diffusivity, t, is time, x, y, z are the spatial variables in the Cartesian system and T is temperature, n is the vector normal to the boundary surface, q is the heat flux, ε is the thermal emissivity and σ is the Boltzmann constant. This equation can be added to COMSOL but further work is required to capture the temperature data experimentally and determine the correct value for α, e.g. Durham, Mirkovich, and Heard (1987) and Lev et al. (2012) who published the values of α for Mauna Loa 1984, Kilauea 1974, Etna 1983, and Etna 2001 as 2.2E-7 m^2s^{-1}.

Project Goals reviewed

This project's goals that were identified in the introduction are restated here in italics along with the relevant observations made after the project was completed.

1. *How can the magma rheology be deconstructed into a smaller, simpler yet realistic system? Determine with: Dimensional analysis and Buckingham Pi theory to identify the determining variables.*

   Dimensional analysis was applied in the design phase of the experiments and by comparing the Froude and Reynolds numbers from the analogue fluids to real lava flows a sense of confidence can be had that the experimental system matches the flow regime of real lava as much as practically possible.

2. *What are the governing equations that describe the system and can it be modelled mathematically and solved? Solve with: COMSOL, Navier-Stokes and continuity equations.*

   The Navier-Stokes equations were used in COMSOL to infer the viscosity of the analogue fluids. These equations describe viscous flow. As long as the boundary conditions can be identified, and the channel morphology can be modelled, these equations can be used to derive the viscosity of the fluid.

3. *Can experiments be conducted in a controlled manner and produce reliable, repeatable and useful data? Identify with pilot study.*

   A pilot study was initiated and the early data of 18 pilot experiments gave valuable insight into the work flow and challenges of the experiments. The experimental apparatus was improved to eliminate bubbles forming during pouring, removal of the beads from the fluid after the experiment, the control of light for video processing and Streams interpretation as well as the limits of the parametric space that could practically be covered with respect to β and h.

4. *How can the data be analysed, interpreted and compared with the model? Compare with: Takagi Huppert analytical equations.*

   A computer program was created to analyse the Streams data and do the Takagi calculations. These results were then compared to the COMSOL model and the viscometer for the Newtonian fluid. The rheometer was used to compare the non-Newtonian fluid. For the Newtonian fluid the viscosity measured by the experiments at 20.7°C was compared to the viscometer, the refractometer and the COMSOL model and found to be very close. For the non-Newtonian fluids, a shear stress vs shear rate curve and a dynamic viscosity vs shear rate curve were plotted and compared between the rheometer and the COMSOL simulations. While the results are not perfect, they are still within an order of magnitude of each other.

5. *How does the experimental data compare with the mathematical model? Compare with statistics.*

   With the Newtonian syrup analogue the analytical solution allowed for a direct comparison of the model's simulation with the experimental result. These experiments were repeated multiple times to allow a statistically meaningful analysis to be done. The experimental results were then also directly compared with those of the viscometer and the mean experimental viscosity was found to be within the margin of error of those of the viscometer. This means the approach has utility and could find application in environments where fluids' surface velocities can be observed but not directly measured with inflow apparatus. Possibly lava flows on Jupiter's moon Io could be analysed this way (Spencer et al., 2007).

6. *What is the value of the research outcome? Discussion of the relevance and utility of these results in the future of lava flow modelling.*

   The model performed well with both Newtonian and non-Newtonian fluids and is now ready to be adapted for variable temperature and Herschel-Bulkley rheology. Once these extensions have been made the model will be able to start modelling actual lava, initially

in a laboratory setting before moving into the field. Since all the sensitivity analysis has been done, the model has been created and the workflow has been optimised this should be achieved by adding the partial differential equation that describes heat distribution and then implementing a non-linear least squares approximation to calculate the coefficients of the Herschel-Bulkley formula in COMSOL. If successful, this will allow the measurement of viscosity from video capture. This should be much safer for volcanologists than trying to sample viscosity with rotational veins and should be faster that using thin sections and X-ray fluorescence generated bulk geochemistry of quenched samples, if the flow depth and density is known.

Chapter Six: Conclusions

Conclusion 1: **Free surface velocity can be used to indirectly measure the viscosity of a Newtonian fluid moving down an inclined V channel.**

The COMSOL Navier-Stokes Newtonian fluid model results matched the results from the analytical solution extremely well. The COMSOL result was also within the measurement uncertainty of the viscometer.

Conclusion 2: **The determination of viscosity from free surface velocity is extremely sensitive to the independent variables: flow height and flow inclination angle.**

It was found that flow depth is the most important factor in determining viscosity. This is of little surprise when considering the underlying mathematical equations governing fluid velocity and viscosity. Flow depth also appears in the three dimensionless numbers that govern this flow regime.

Conclusion 3: **The Takagi-Huppert analytical solution is valid.**

The steady state analytical solution for Newtonian isothermal fluids when applied to the experimental data determines the same solution as the Navier-Stokes equations used in COMSOL, which validates the Takagi-Huppert solution experimentally.

Conclusion 4: **A COMSOL model can be made to accurately calculate the viscosity of a non-Newtonian fluid from its free surface velocity.**

The results were close to the commercial rheometer and with some improvements to the experimental procedures and equipment it is believed that the results can improve further.

Chapter Seven: Future work

Improve measurement of flow height

Flow thickness was identified as a critical independent variable, along with, but to a lesser extent, inclination angle of the flow. Any improvements to measuring flow height will improve the model's accuracy. The use of ultrasonic or LiDAR range finders might facilitate the measurement where the distance to the base of the flow is known.

Extend to non-isothermal experiments

The effect of keeping temperature constant enabled the experimental data to be collected much faster. For lava, however, temperature dependent viscosity is an important component to model. The energy conservation equation can be combined with the Navier-Stokes equations so the model can be extended. The high temperature experiments, however, will take considerable time to design. Figure 51 shows early stages of this design work.

Figure 51. Non isothermal lava flow in a V channel.

Add the Herschel-Bulkley equations to COMSOL

It was decided early on to simplify the model and gradually add complexity as each change was validated. After the Newtonian fluid viscosities were satisfactorily represented by the COMSOL model, it was then modified to solve for pseudo-plastic or shear thinning fluids by extending the model to use the power law. Further work to improve the COMSOL model would encompass extending the COMSOL solver to solve the Herschel- Bulkley equation in place of the power law. Currently these equations are not built into COMSOL, but there is the feature to add custom equations.

Define and implement an objective function to improve calculations in COMSOL

In the case of the analytical solution the code produced was able to calculate the difference between the integral for the two equations of best fit for the velocity parabolas for the golden syrup experiments. This gave a metric whereby the search for a solution could be automated based upon a simple objective function. This was not done in the non-Newtonian case because there were only a few experiments to analyse and the time required to implement an objective function into COMSOL would have been much greater than doing this by hand. A parametric sweep was configured in COMSOL and the n and k values for the rheometer were used as a starting point to derive the simulation values for n and k. The variable k was tested in the range $0 < \mathrm{k} \leq 1000$ in increments of 100 initially and then 1 and then 0.1 as the shape started to converge. While the variable n was tested in the range $0 < \mathrm{n} < 1$ in increments of 0.1.

For the case where multiple experiments are going to be performed, or the complexity of a parametric sweep is increased by the Herschel-Bulkley equations then it would be recommended to implement. In mathematical terms, to implement a power law function $\mathrm{F(x)}$ that fits the experimental data $\mathrm{D(x)}$ as closely as possibly when minimising:

$$\int_a^b (D(x) - F(x))^2 dx$$

Where, a and b are the channel boundaries, where the velocity is zero.

References

Avila, K., Moxey, D., De Lozar, A., Avila, M., Barkley, D., & Hof, B. (2011, July 8). The onset of turbulence in pipe flow. *Science*. https://doi.org/10.1126/science.1203223

Bagdassarov, N., & Pinkerton, H. (2004). A review and investigation of the Non-Newtonian properties of lavas based on laboratory experiments with analogue materials. *Journal of Volcanology and Geothermal Research, 45*(3), 197. Retrieved from https://user.uni-frankfurt.de/~nickbagd/thixotropy.pdf

Bagdassarov, N. S. (2004). Non-Newtonian and Viscoelastic Properties of Lava Flows. *American Geophysical Union, Fall Meeting 2004, Abstract Id. V51D-04*. Retrieved from http://adsabs.harvard.edu/abs/2004AGUFM.V51D..04B

Behncke, B., & Neri, M. (2003). The July-August 2001 eruption of Mt. Etna (Sicily). *Bulletin of Volcanology*, *65*(7), 461–476. https://doi.org/10.1007/s00445-003-0274-1

Biass, S., Orr, T. R., Houghton, B. F., Patrick, M. R., James, M. R., & Turner, N. (2019). Insights into pāhoehoe lava emplacement using visible and thermal structure-from-motion photogrammetry. *Journal of Geophysical Research: Solid Earth*, 2019JB017444. https://doi.org/10.1029/2019JB017444

Blake, S. (1990). Viscoplastic Models of Lava Domes (pp. 88–126). Springer, Berlin, Heidelberg. https://doi.org/10.1007/978-3-642-74379-5_5

Calvari, S., & Pinkerton, H. (1999). Lava tube morphology on Etna and evidence for lava flow emplacement mechanisms. *Journal of Volcanology and Geothermal Research, 90*(3–4), 263–280. https://doi.org/10.1016/S0377-0273(99)00024-4

Castruccio, A., Rust, A. C., & Sparks, R. S. J. (2014). Assessing lava flow evolution from post-eruption field data using Herschel-Bulkley rheology. *Journal of Volcanology and Geothermal Research, 275*, 71–84. https://doi.org/10.1016/j.jvolgeores.2014.02.004

Chevrel, M. O., Harris, A. J. L., James, M. R., Calabrò, L., Gurioli, L., & Pinkerton, H. (2018). The viscosity of pāhoehoe lava: In situ syn-eruptive measurements from Kilauea, Hawaii. *Earth and Planetary Science Letters*, *493*, 161–171. https://doi.org/10.1016/j.epsl.2018.04.028

Chevrel, O., Labroquère, J., Harris, A., & Rowland, S. (2017). PyFLOWGO: an open-source platform for simulation of channelized lava thermo-rheological properties. *Computers in Geosciences, Underreview*, *111* (November 2017), 167–180. https://doi.org/10.1016/j.cageo.2017.11.009

Cordonnier, B., Lev, E., & Garel, F. (2016). Benchmarking lava-flow models. *Geological Society, London, Special Publications*, *426*(1). https://doi.org/10.1144/SP426.7

Costa, A., & Macedonio, G. (2005). Numerical simulation of lava flows based on depth-averaged equations. *Geophysical Research Letters*, *32*(5), 1–5. https://doi.org/10.1029/2004GL021817

Crawford, N. C., Popp, L. B., Johns, K. E., Caire, L. M., Peterson, B. N., & Liberatore, M. W. (2013). Shear thickening of corn starch suspensions: Does concentration matter? *Journal of Colloid and Interface Science*, *396*, 83–89. https://doi.org/10.1016/j.jcis.2013.01.024

Dawson, J. B., Pinkerton, H., Norton, G. E., & Pyle, D. M. (1990). Physicochemical properties of alkali carbonatite lavas:Data from the 1988 eruption of Oldoinyo Lengai, Tanzania. *Geology*, *18*(3), 260. https://doi.org/10.1130/0091-7613(1990)018<0260:PPOACL>2.3.CO;2

Dawson, J. B., Pinkerton, H., Pyle, D. M., & Nyamweru, C. (1994). June 1993 eruption of Oldoinyo Lengai, Tanzania: exceptionally viscous and large carbonatite lava flows and evidence for coexisting silicate and carbonate magmas. *Geology*, *22*(9), 799–802. https://doi.org/10.1130/0091-7613(1994)022<0799:JEOOLT>2.3.CO;2

Dietterich, H., Cashman, K., Rust, A., & Lev, E. (2015). Diverting lava flows in the lab. *Nature Geoscience*, *8*(July), 8–10. https://doi.org/10.1038/ngeo2470

Dietterich, H., Lev, E., Chen, J., Cashman, K., & Honor, C. (2015). Benchmarking computational fluid dynamics models for application to lava flow simulations and hazard assessment [abs.]. *American Geophysical Union, Fall Meeting 2015 Abstracts*, abstract no. V13D-07. https://doi.org/10.1186/s13617-017-0061-x

Doocy, S., Daniels, A., Dooling, S., & Gorokhovich, Y. (2013). The Human Impact of Volcanoes: a Historical Review of Events 1900-2009 and Systematic Literature Review. *PLoS Currents*. https://doi.org/10.1371/currents.dis.841859091a706efebf8a30f4ed7a1901

Dragoni, M., Bonafede, M., & Boschi, E. (1986). Downslope flow models of a Bingham liquid: Implications for lava flows. *Journal of Volcanology and Geothermal Research*, *30*(3–4), 305–325. https://doi.org/10.1016/0377-0273(86)90059-4

Dragoni, M., & Tallarico, A. (1994). The effect of crystallization on the rheology and dynamics of lava flows. *Journal of Volcanology and Geothermal Research*, *59*(3), 241–252. https://doi.org/10.1016/0377-0273(94)90098-1

Dragoni, N. (1989). *A dynamical model of lava flows cooling by radiation* (Vol. 51). Retrieved from https://link.springer.com/content/pdf/10.1007%2FBF01081978.pdf

Drazin, P. G., & Riley, N. (2006). *The Navier-Stokes Equations : a Classification of Flows and Exact Solutions*. Cambridge University Press.

Durham, W. B., Mirkovich, V. V., & Heard, H. C. (1987). Thermal diffusivity of igneous rocks at elevated pressure and temperature. *Journal of Geophysical Research: Solid Earth*, *92*(B11), 11615–11634. https://doi.org/10.1029/JB092iB11p11615

Farrell, J., Karson, J., Soldati, A., & Wysocki, R. (2018). Multiple-generation folding and non-coaxial strain of lava crusts. *Bulletin of Volcanology*, *80*(12). https://doi.org/10.1007/s00445-018-1258-5

Favalli, M., Chirico, G. D., Papale, P., Pareschi, M. T., & Boschi, E. (2009). Lava flow hazard at Nyiragongo volcano, D.R.C. 1. Model calibration and hazard mapping. *Bulletin of Volcanology*, *71*(4), 363–374. https://doi.org/10.1007/s00445-008-0233-y

Favalli, M., Pareschi, M. T., Neri, A., & Isola, I. (2005). Forecasting lava flow paths by a stochastic approach. *Geophysical Research Letters*, *32*(3), L03305. https://doi.org/10.1029/2004GL021718

Fefferman, C. L. (n.d.). *EXISTENCE AND SMOOTHNESS OF THE NAVIER-STOKES EQUATION*. Retrieved from http://www.claymath.org/sites/default/files/navierstokes.pdf

Fournier d'Albe, E. M. (2007). Objectives of volcanic monitoring and prediction. *Journal of the Geological Society*, *136*(3), 321–326. https://doi.org/10.1144/gsjgs.136.3.0321

Giordano, D., Romano, C., Papale, P., & Dingwell, D. B. (2004). The viscosity of trachytes, and comparison with basalts, phonolites, and rhyolites. *Chemical Geology*, *213*(1–3), 49–61. https://doi.org/10.1016/J.CHEMGEO.2004.08.032

Gregg, T. K. P., Fink, J. H., & Griffiths, R. W. (1998). Formation of multiple fold generations on lava flow surfaces: Influence of strain rate, cooling rate, and lava composition. *Journal of Volcanology and Geothermal Research*, *80*(3–4), 281–292. https://doi.org/10.1016/S0377-0273(97)00048-6

Griffiths, R. W. (2000). The Dynamics of Lava Flows. *Annual Review of Fluid Mechanics*, *32*(1), 477–518. https://doi.org/10.1146/annurev.fluid.32.1.477

Harris, A. J. L., & Rowland, S. K. (2015). Lava Flows and Rheology. In *The Encyclopedia of Volcanoes* (pp. 321–342). https://doi.org/10.1016/b978-0-12-385938-9.00017-1

Huxley, A. S. (1967, August). Hysteresis experiments in rheology. *Nature*. Nature Publishing

Group. https://doi.org/10.1038/215620a0

James, M. R., Applegarth, L. J., Pinkerton, H., & Fryer, T. (2010). Estimating rheological properties of lava flows using high-resolution time lapse imaging. The Lancaster Environment Centre. Retrieved from http://eprints.lancs.ac.uk/51714/1/James_et_al_AGU.pdf

James, M. R., Robson, S., & Pinkerton, H. (2011). Determining the rheology of active lava flows from photogrammetric image sequence processing. Natural Environment Research Council. Retrieved from http://eprints.lancs.ac.uk/69326/1/James_et_al_AGU_2010_Rheology.pdf

Jeffreys, H. (1925). LXXXIV. The flow of water in an inclined channel of rectangular section. *The London, Edinburgh, and Dublin Philosophical Magazine and Journal of Science*, *49*(293), 793–807. https://doi.org/10.1080/14786442508634662

Kauahikaua, J., Cashman, K. V., Mattox, T. N., Heliker, C. C., Hon, K. A., Mangan, M. T., & Thornber, C. R. (1998). Observations on basaltic lava streams in tubes from Kilauea Volcano, island of Hawai'i. *Journal of Geophysical Research: Solid Earth*, *103*(B11), 27303–27323. https://doi.org/10.1029/97JB03576

Kelfoun, K., Vallejo Vargas, S., & Vargas, S. V. (2015). VolcFlow capabilities and potential development for the simulation of lava flows. *Geological Society, London, Special Publications*, *426*(1), 337–343. https://doi.org/https://doi.org/10.1144/SP426.8

Kereszturi, Á., & Hargitai, H. (2014). Thermal Erosion Channel. In *Encyclopedia of Planetary Landforms* (pp. 1–4). New York, NY: Springer New York. https://doi.org/10.1007/978-1-4614-9213-9_369-1

Kim, K., Pant, P., & Yamashita, E. (2018). Managing uncertainty: Lessons from volcanic lava disruption of transportation infrastructure in Puna, Hawaii. *Journal of Emergency Management*, *16*(1), 29. https://doi.org/10.5055/jem.2018.0351

Lensky, N. G., Lyakhovsky, V., & Navon, O. (2002). Expansion dynamics of volatile-supersaturated liquids and bulk viscosity of bubbly magmas. *Journal of Fluid Mechanics*, *460*, 39–56. https://doi.org/10.1017/S0022112002008194

Lev, E., Spiegelman, M., Wysocki, R. J., & Karson, J. A. (2012). Investigating lava flow rheology using video analysis and numerical flow models. *Journal of Volcanology and Geothermal Research*, *247–248*, 62–73.

Lide, D. R. (1999). *CRC Handbook of Chemistry and Physics - Reference Book of Chemical and Physical Data*. CRC Press. Retrieved from

https://books.google.co.nz/books?hl=en&lr=&id=q2qJId5TKOkC&oi=fnd&pg=PP23&dq=crc+handbook+of+chemistry+and+physics+1978&ots=9WaX-FnhHk&sig=9Q31ohWbTPG714hSdPlGHJJ95QI#v=onepage&q=crc handbook of chemistry and physics 1978&f=false

Liu, K. F., & Mei, C. C. (1990). Approximate equations for the slow spreading of a thin sheet of Bingham plastic fluid. *Physics of Fluids A: Fluid Dynamics*, *2*(1), 30–36. https://doi.org/10.1063/1.857821

Llewellin, E. W., Mader, H. M., & Wilson, S. D. R. (2002). The rheology of a bubbly liquid. *Proceedings of the Royal Society A: Mathematical, Physical and Engineering Sciences*, *458*(2020), 987–1016. https://doi.org/10.1098/rspa.2001.0924

Manga, M., Castro, J., Cashman, K. V., & Loewenberg, M. (1998). Rheology of bubble-bearing magmas. *Journal of Volcanology and Geothermal Research*, *87*(1–4), 15–28. https://doi.org/10.1016/S0377-0273(98)00091-2

Miyamoto, H., & Sasaki, S. (2002). Simulating lava flows by an improved cellular automata method. *Computers & Geosciences*. https://doi.org/10.1016/s0098-3004(96)00089-1

Miyamoto, H., & Sasaki, S. (2004). Numerical simulations of flood basalt lava flows: Roles of parameters on lava flow morphologies. *Journal of Geophysical Research: Solid Earth*. https://doi.org/10.1029/98jb00438

Moore, Henry, J. (1987). Preliminary Estimates of the Rheological Properties of 1984 Mauna Loa Lava.pdf. *USGS Professional Paper*, *1350*(99), 1569–1588.

Naranjo, M. F., Ebmeier, S. K., Vallejo, S., Ramón, P., Mothes, P., Biggs, J., & Herrera, F. (2016). Mapping and measuring lava volumes from 2002 to 2009 at El Reventador Volcano, Ecuador, from field measurements and satellite remote sensing. *Journal of Applied Volcanology*, *5*(1), 8. https://doi.org/10.1186/s13617-016-0048-z

Neal, C. A., Brantley, S. R., Antolik, L., Babb, J. L., Burgess, M., Calles, K., … Damby, D. (2019). The 2018 rift eruption and summit collapse of Kīlauea Volcano. *Science (New York, N.Y.)*, *363*(6425), 367–374. https://doi.org/10.1126/science.aav7046

Negro, C. Del, Fortuna, L., Herault, A., & Vicari, A. (2007). Simulations of the 2004 lava flow at Etna volcano using the magflow cellular automata model. https://doi.org/10.1007/s00445-007-0168-8

Nokes, R. (Department of C. and N. R. E. (2018). Streams version 2.06. Christchurch: University of Canterbury. Retrieved from https://www.canterbury.ac.nz/engineering/schools/cnre/software/streams/

Patrick, M. R., Kauahikaua, J., Orr, T., Davies, A., & Ramsey, M. (2016). Operational thermal remote sensing and lava flow monitoring at the Hawaiian Volcano Observatory. *Geological Society, London, Special Publications*, *426*(1), 489–503. https://doi.org/10.1144/SP426.17

Patrick, Matthew R., & Orr, T. R. (2018). *Operational Tracking of Lava Lake Surface Motion at Kīlauea Volcano , Hawai'i*. *Volcano Monitoring*. Retrieved from https://pdfs.semanticscholar.org/a6c3/05911e7af39f4b35c7ed49bc919b11b0fb8e.pdf?_ga=2.262650825.473624545.1566358350-2003311400.1566358350

Pinkerton, H. Sparks, R. S. . (1996). The 1975 sub-terminal lacas, Mount Etna: A Case History of the formation of a compound lava field. *Journal of Volcanology and Geothermal Research*, *65*, 255–257. https://doi.org/10.1016/j.tetlet.2006.08.105

Pinkerton, H., & Sparks, R. S. J. (1978). Field measurements of the rheology of lava [7]. *Nature*, *276*(5686), 383–385. https://doi.org/10.1038/276383a0

Pixabay GmbH. (n.d.). Lava tube skylight. Retrieved July 29, 2019, from https://pixabay.com/photos/lava-volcanic-crust-molten-window-1524277/

Prakash, M., & Cleary, P. W. (2011). Three dimensional modelling of lava flow using Smoothed Particle Hydrodynamics. *Applied Mathematical Modelling*, *35*(6), 3021–3035. https://doi.org/10.1016/j.apm.2010.12.023

Roberts, G. P., Barnes, H. A., & Carew, P. (2001). Modelling the flow behaviour of very shear-thinning liquids. *Chemical Engineering Science*, *56*(19), 5617–5623. https://doi.org/10.1016/S0009-2509(01)00291-3

Rowland, S. K., & Walker, G. P. L. (1988). Mafic-crystal distributions, viscosities, and lava structures of some Hawaiian lava flows. *Journal of Volcanology and Geothermal Research*, *35*(1–2), 55–66. https://doi.org/10.1016/0377-0273(88)90005-4

Rumpf, M. E., Lev, E., & Wysocki, R. (2018). The influence of topographic roughness on lava flow emplacement. *Bulletin of Volcanology*, *80*(7), 63. https://doi.org/10.1007/s00445-018-1238-9

Shaw, H. R., Wright, T. L., Peck, D. L., & Okamura, R. (1968). The viscosity of basaltic magma; an analysis of field measurements in Makaopuhi lava lake, Hawaii. *American Journal of Science*, *266*(4), 225–264. https://doi.org/10.2475/ajs.266.4.225

Spencer, J. R., Stern, S. A., Cheng, A. F., Weaver, H. A., Reuter, D. C., Retherford, K., … Dumas, C. (2007). Io volcanism seen by new horizons: a major eruption of the Tvashtar volcano. *Science (New York, N.Y.)*, *318*(5848), 240–243.

https://doi.org/10.1126/science.1147621

Takagi, D., & Huppert, H. E. (2007). The effect of confining boundaries on viscous gravity currents. *Journal of Fluid Mechanics*, *577*, 495. https://doi.org/10.1017/S0022112007005174

Takagi, D., & Huppert, H. E. (2010). Initial advance of long lava flows in open channels. *Journal of Volcanology and Geothermal Research*, *195*(2–4), 121–126. https://doi.org/10.1016/j.jvolgeores.2010.06.011

Thordarson, T., & Self, S. (1998). The Roza Member, Columbia River Basalt Group: A gigantic pahoehoe lava flow field formed by endogenous processes? *Journal of Geophysical Research: Solid Earth*, *103*(B11), 27411–27445. https://doi.org/10.1029/98jb01355

Upton, G., & Cook, I. (2014). *A Dictionary of Statistics*. *A Dictionary of Statistics* (3rd ed.). Oxford: Oxford University Press. https://doi.org/10.1093/acref/9780199679188.001.0001

Williams, D. A. (2004). A potential thermal erosion lava channel on Io. *Geophys. Res. Lett*, *31*, 23702. https://doi.org/10.1029/2004GL021378

WIlliams, R. (1973). LAVA-COOLING OPERATIONS DURING THE 1973 ERUPTION OF ELDFELL VOLCANO, HEIMAEY, VESTMANNAEYJAR, ICELAND. *U.S. GEOLOGICAL SURVEY OPEN-FILE REPORT*, 97–724.

Zago, V., Bilotta, G., Cappello, A., Dalrymple, R. A., Fortuna, L., Ganci, G., … He, A. (2018). Preliminary validation of lava benchmark tests on the GPUSPH particle engine, *61*. https://doi.org/10.4401/ag-7870

Appendices

Appendix I List of Symbols

T	Temperature
d	Flow height
β	Flow inclination angle
α	Thermal diffusivity
g	Acceleration due to Earth gravity
t	Time
v	Velocity
p	Pressure
w	Thermodynamic work
q	Heat flux
η, μ	Dynamic Viscosity
m	Mass
a	Acceleration
k	Flow consistency index
$\dot{\gamma}$	Shear rate
n	Behavioural index
h	Flow depth
L	Dimensionless unit length
M	Dimensionless unit mass
T	Dimensionless unit time
i	Iterator integer
j	Iterator integer
Q	Flow rate
K	Scaler constant
Θ	Half the angle of the V channel
λ	Scaler coefficient
X	Transformed coordinate
Y	Transformed coordinate
m'	Tan(θ)
M	Inclination dependent parameter
s	Seconds
Π	Pi group
f	Function
P	Parameter
n	Governing parameters
P	Wetted perimeter
L_h	Entrance length

Appendix II COMSOL model details

The COMSOL model was created using the following steps:

1. Open a new project and add the physics packages
2. Build a 2D slice of the model's geometry
3. Extrude the model to create a 3D model
4. Define the boundary conditions
5. Define the slip conditions no slip, no slip, slip
6. Define the flow conditions
7. Build the mesh
8. Enter the parameters and variables used to solve the equations
9. Compute the solution with Laminar flow, stationary solver and a user defined density and viscosity

Table 14. User defined variables.

Settings | Properties

Variables

Label: my variables

Variables

Name	Expression	Unit	Description
g	9.81 [m/s/s]	m/s^2	gravity
rho	1430 [kg/m^3]	kg/m^3	density
fy	rho*g_const*cos(b)	N/m^3	body force
b	10/ 180 * pi		inclination angle
mu	nu*rho	kg/(m·s)	dynamic viscosity
nu	0.185[m^2/s]	m^2/s	kinematic viscosity
L	height		flow depth
exp	8		experiment number
fz	rho*g_const*sin(b)	N/m^3	body force

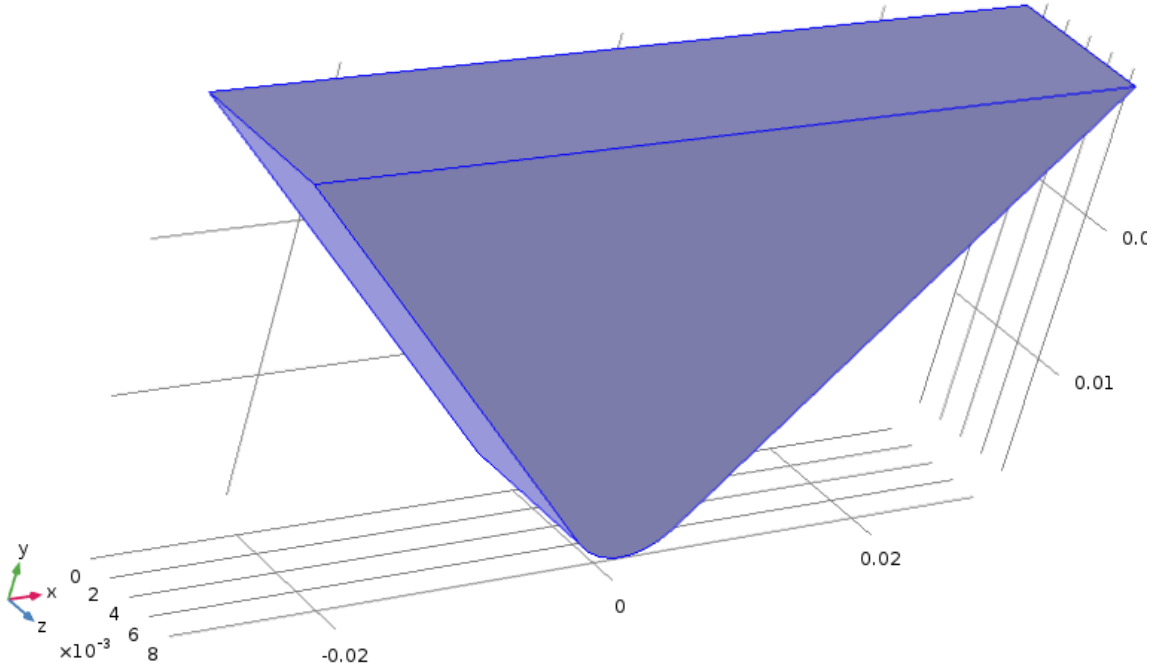

Figure 52. Basic geometry of the V channel complete with a small fillet at the bottom. The height is determined by the user variable height.

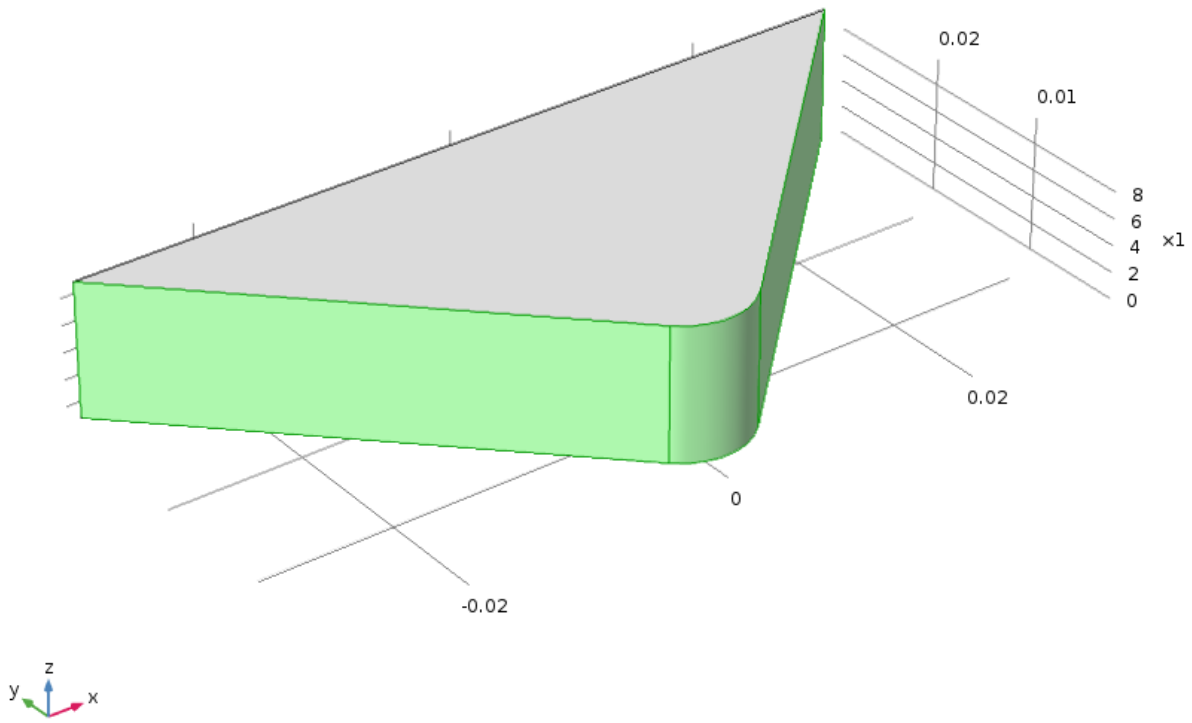

Figure 53. No slip boundaries on the V channel walls in light green.

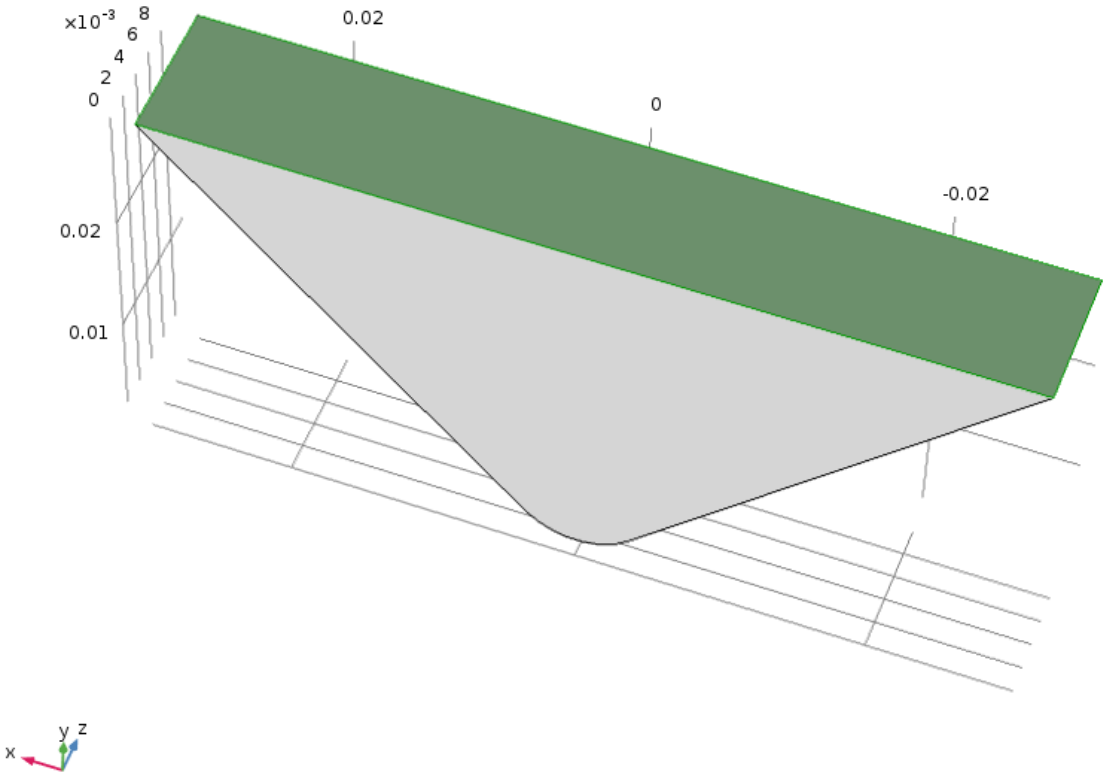

Figure 54. Slip boundary conditions enabled on the free surface of the flow in green.

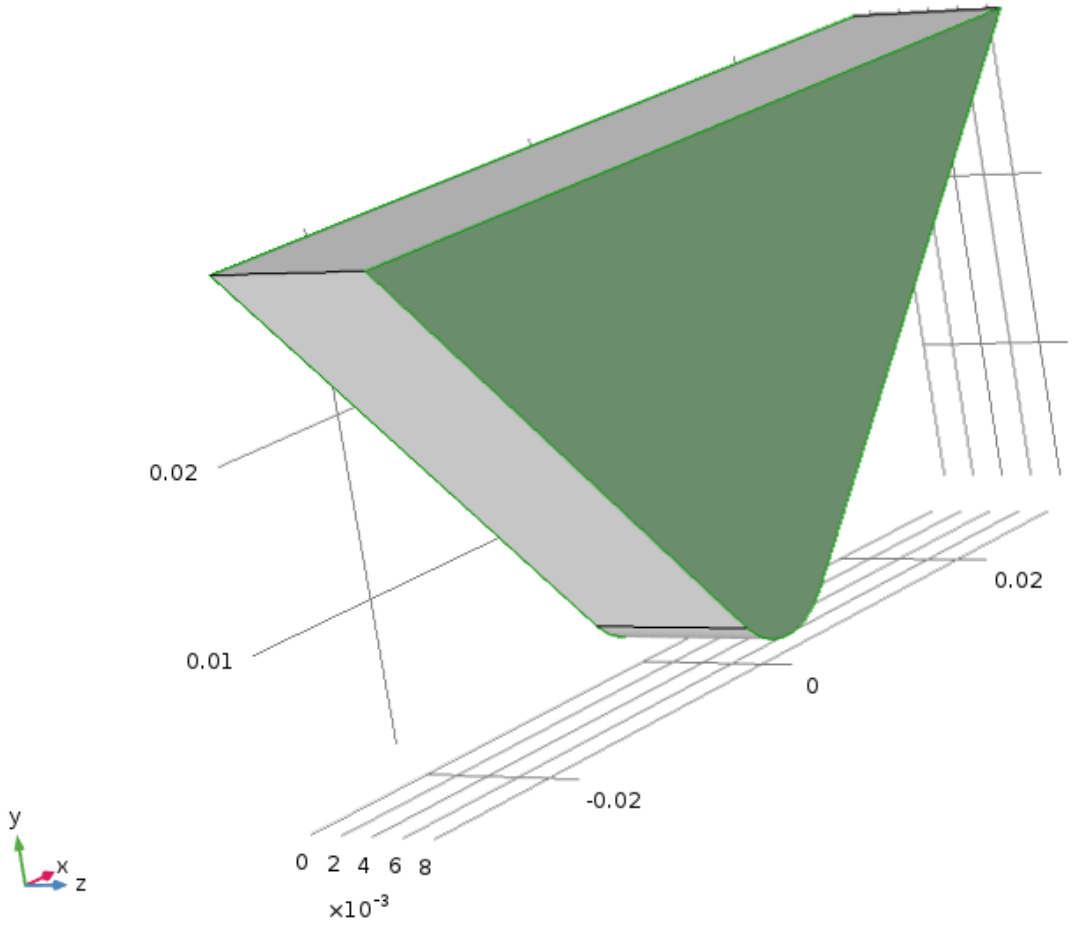

Figure 55. Periodic flow condition, in green, applied to the internal flow down the channel.

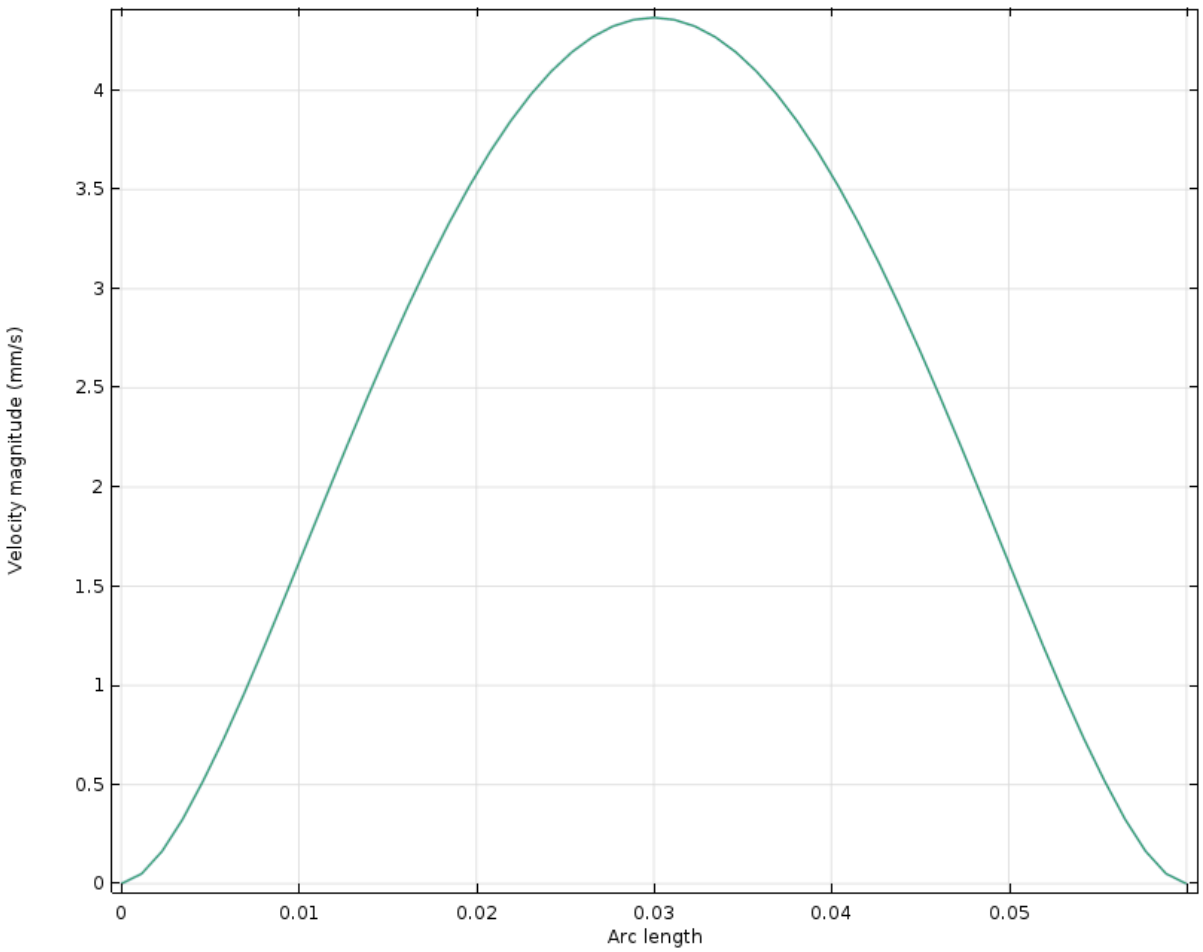

Figure 56. Line graph of velocity magnitude (mm/s) as per experimental parameters shown in **Table 14.**

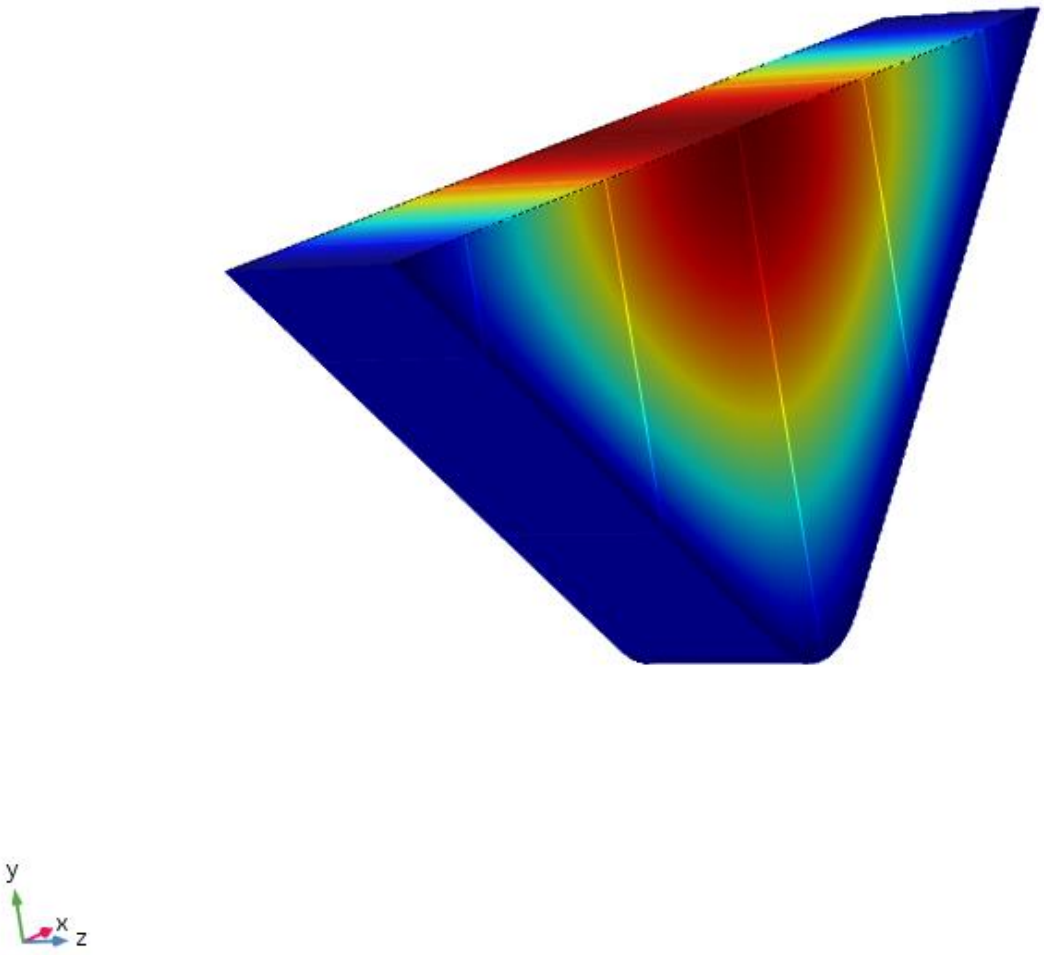

Figure 57. Slice shows velocity magnitude (m/s). Surface shows velocity magnitude (m/s).

Figure 57 shows the final computed solution for golden syrup. The warmer colours represent the higher velocities as they increase monotonically towards the centre of the V channel. Figure 56 shows the peak streamwise velocity, $u = 4.41\ mm/s$.

Appendix III Preparation of Carbopol® polymer 980

1. A predefined quantity of Carbopol® was slowly dispersed over the surface of 3L of demineralized water contained in a 4L glass beaker. The beaker was placed above a magnetic agitator with a heating element and left for 2 days stirring at 50°C to completely dissolve the Carbopol® powder into the water.
2. 3 ml of blue food colouring was added to the clear gel solution to improve contrast.
3. Sodium hydroxide (NaOH) 18%wt was added at an initial 2.3/1.0 ratio of base to polymer to neutralise the solution. The pH was measured using a Mettler Toledo pH meter and the amount of NaOH was increased if needed to bring the pH up to between 7 and 8. Mixing stopped as soon as the solution started to react.
4. Water was added to the pH stabilised solution to further reduce the viscosity at a ratio of 1:4 distilled deionised water to polymer solution.
5. The solution was covered and left at rest at least 12 hours.

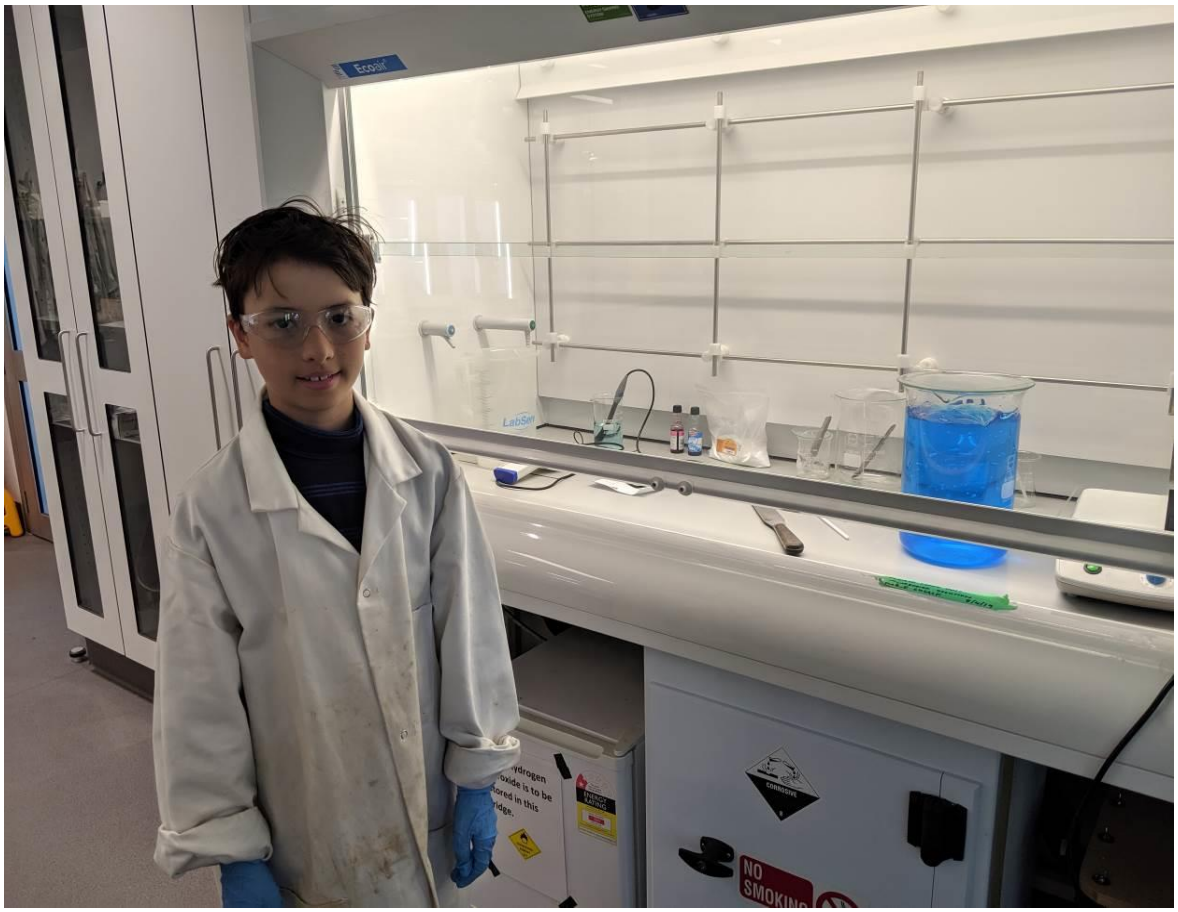

Figure 58. The Carbopol® solution in the fume cupboard after stabilization and colouring. The polymer is a clear gel and colour was added for contrast. To the left the heating plate/magnetic agitator is visible and in the background the pH meter can just be seen.

Appendix IV Anton Paar rheometer

Figure 59. Bottom right is the water cooler and controller, top right is the compressed air supply, middle is the Rheometer and left is the computer running Rheocompass. The sample of Carbopol® being analysed can be seen on the table next to the mouse.

Figure 60. The cup and ball method was used to measure the viscosity.

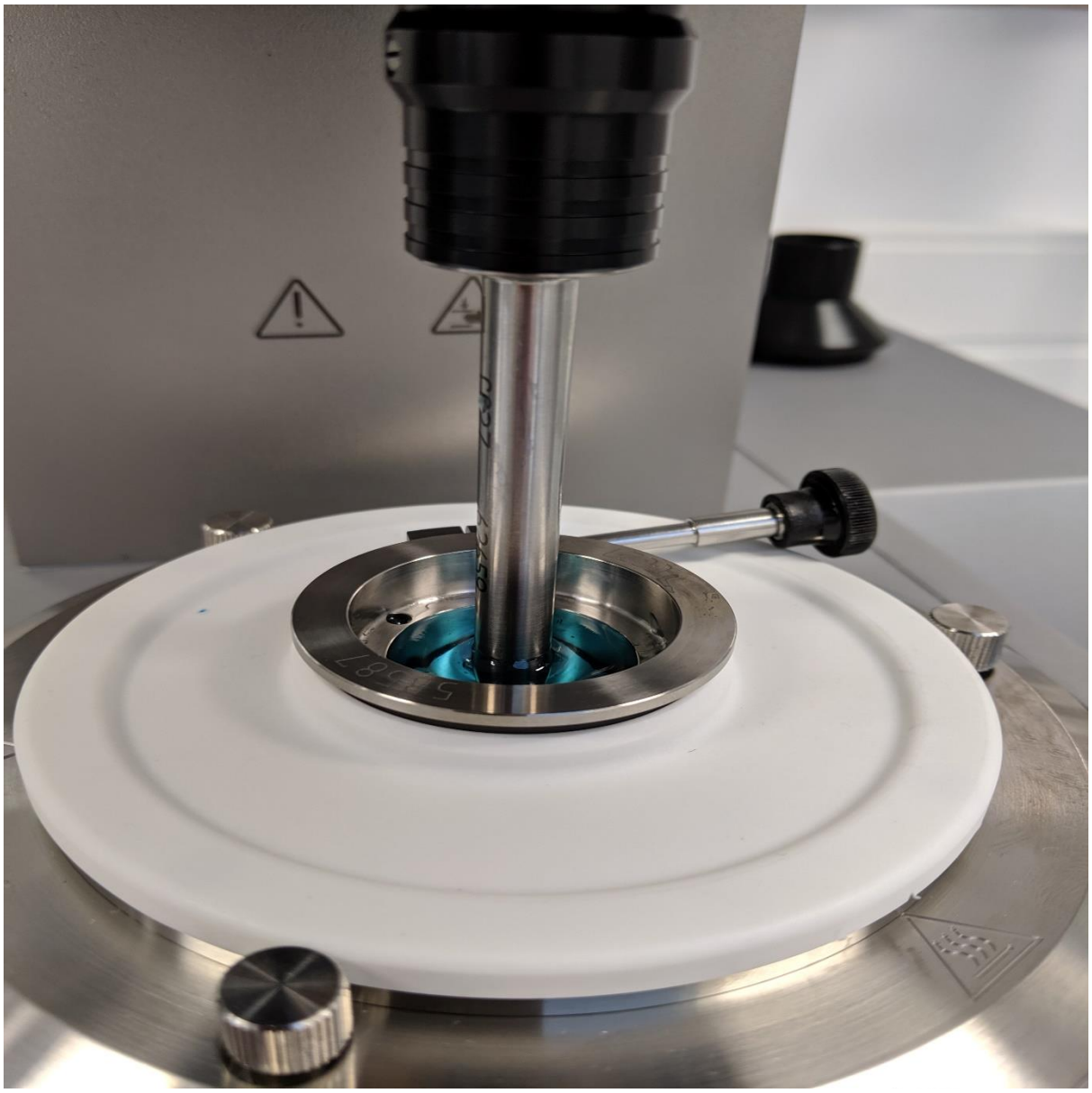

Figure 61. The Carbopol® solution in blue, is loaded into the cup and the ball has been inserted and calibrated.

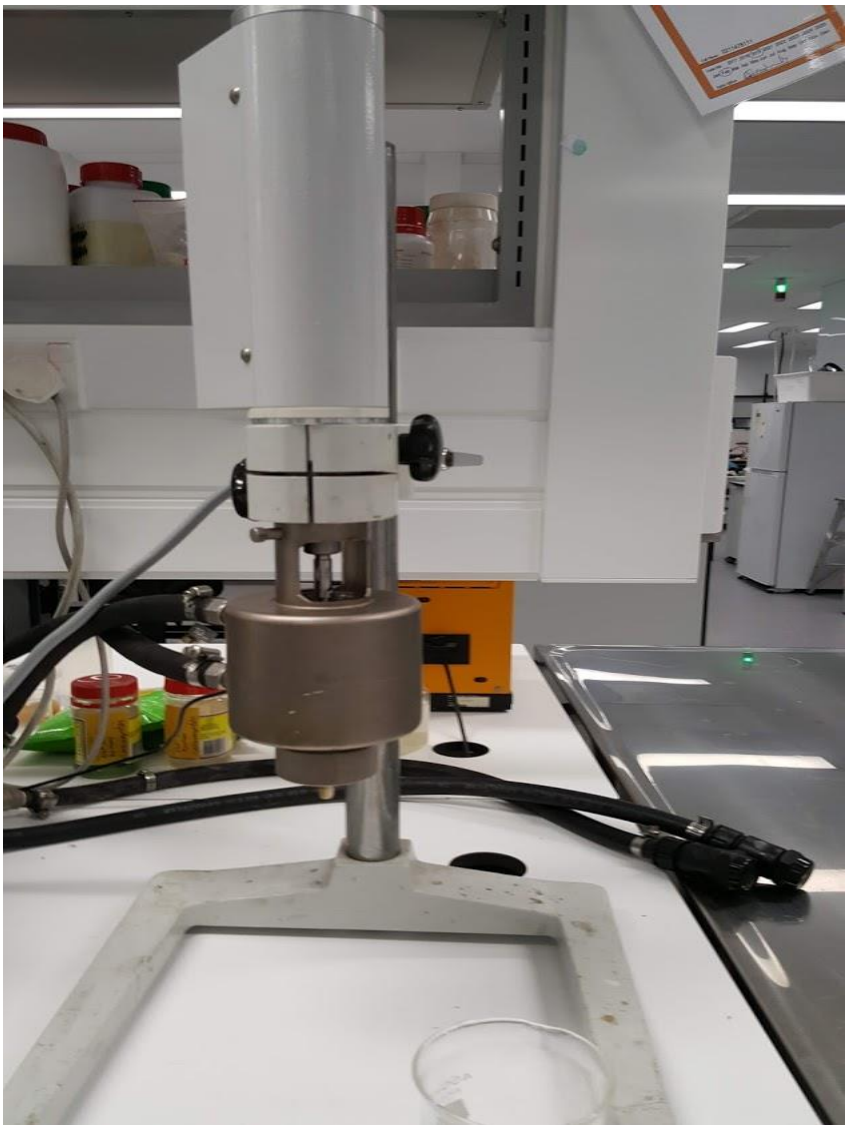

Figure 62. The ancient Haake RV 20 viscometer has now been replaced with the Anton Paar rheometer. Golden syrup samples for analysis can be seen bottom left.

Appendix V Independent variables

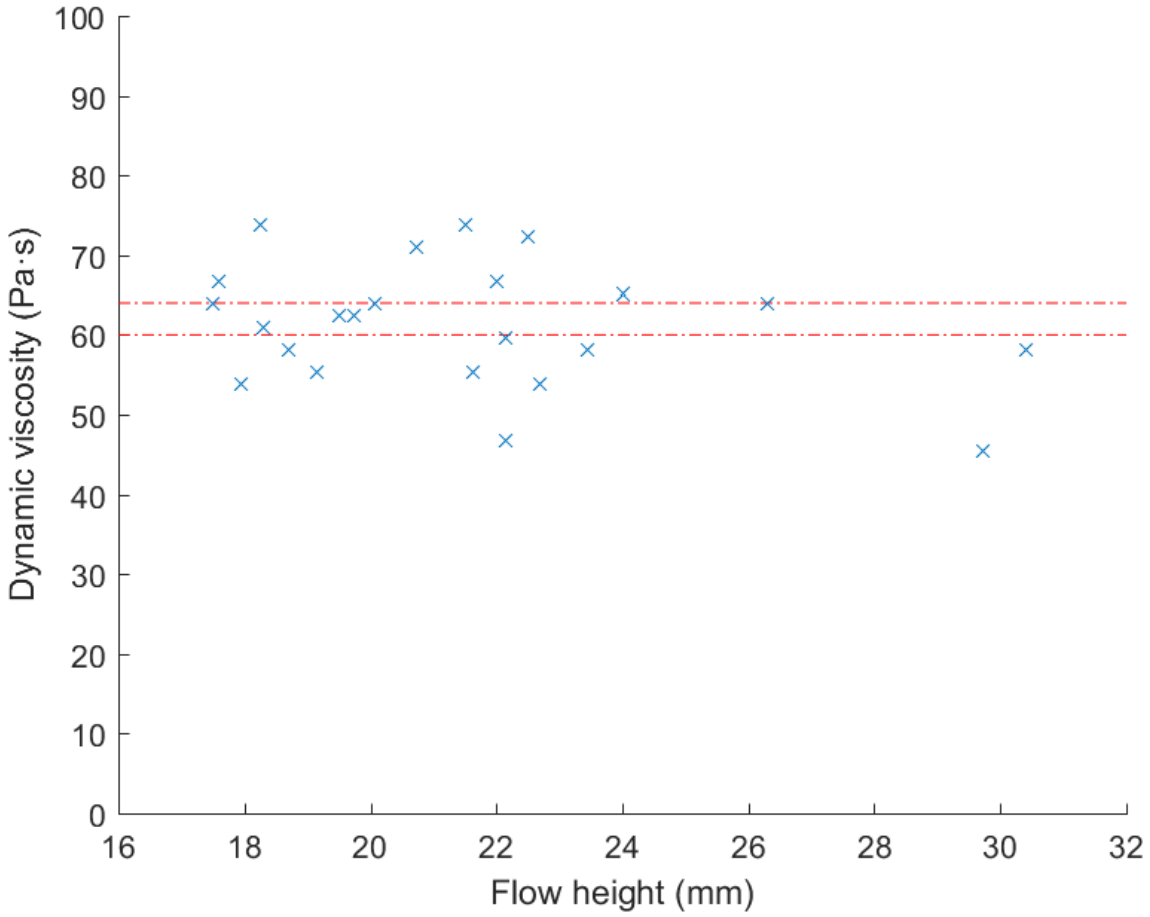

Figure 63. The range of flow thicknesses tested (blue crosses). Red dashed lines are the upper and lower rheometer results.

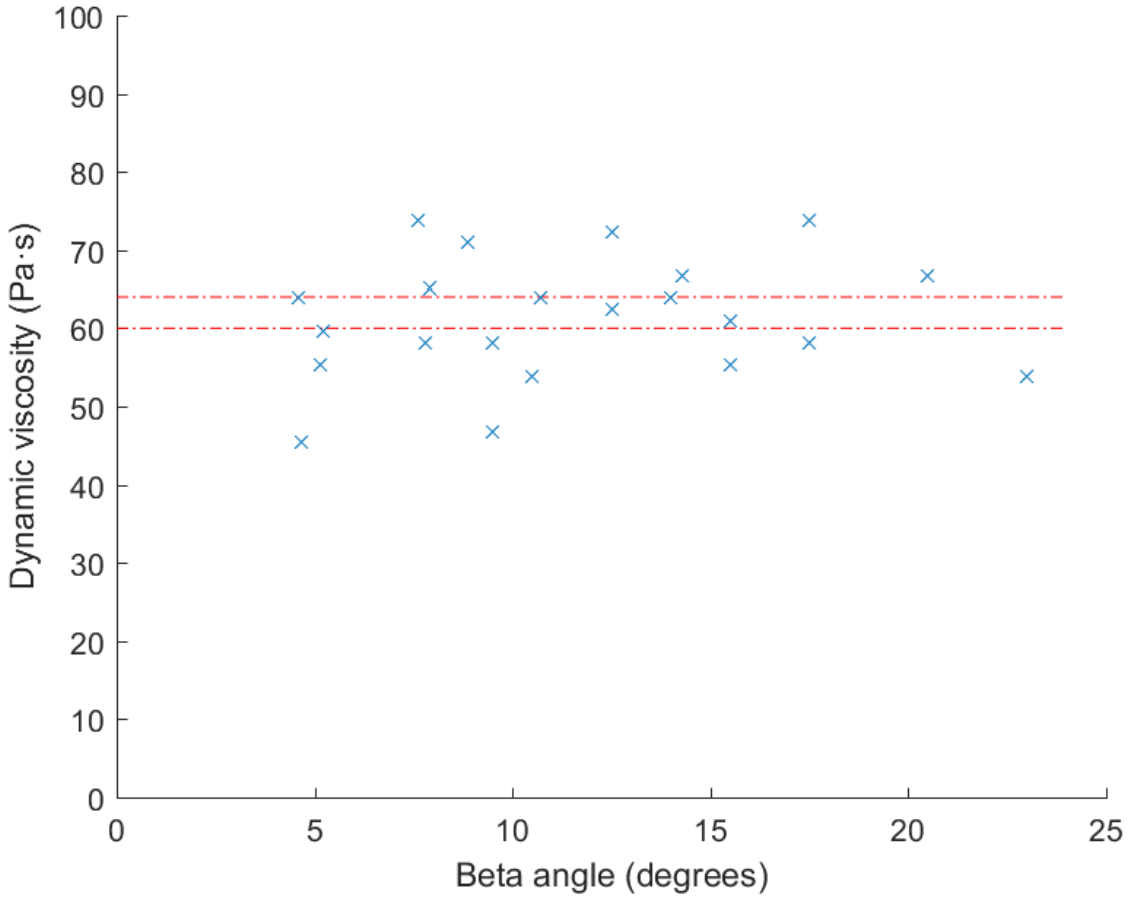

Figure 64. The range of inclination angles, β tested (blue crosses). Red dashed lines are the upper and lower rheometer results.

Appendix VI Hysteresis test

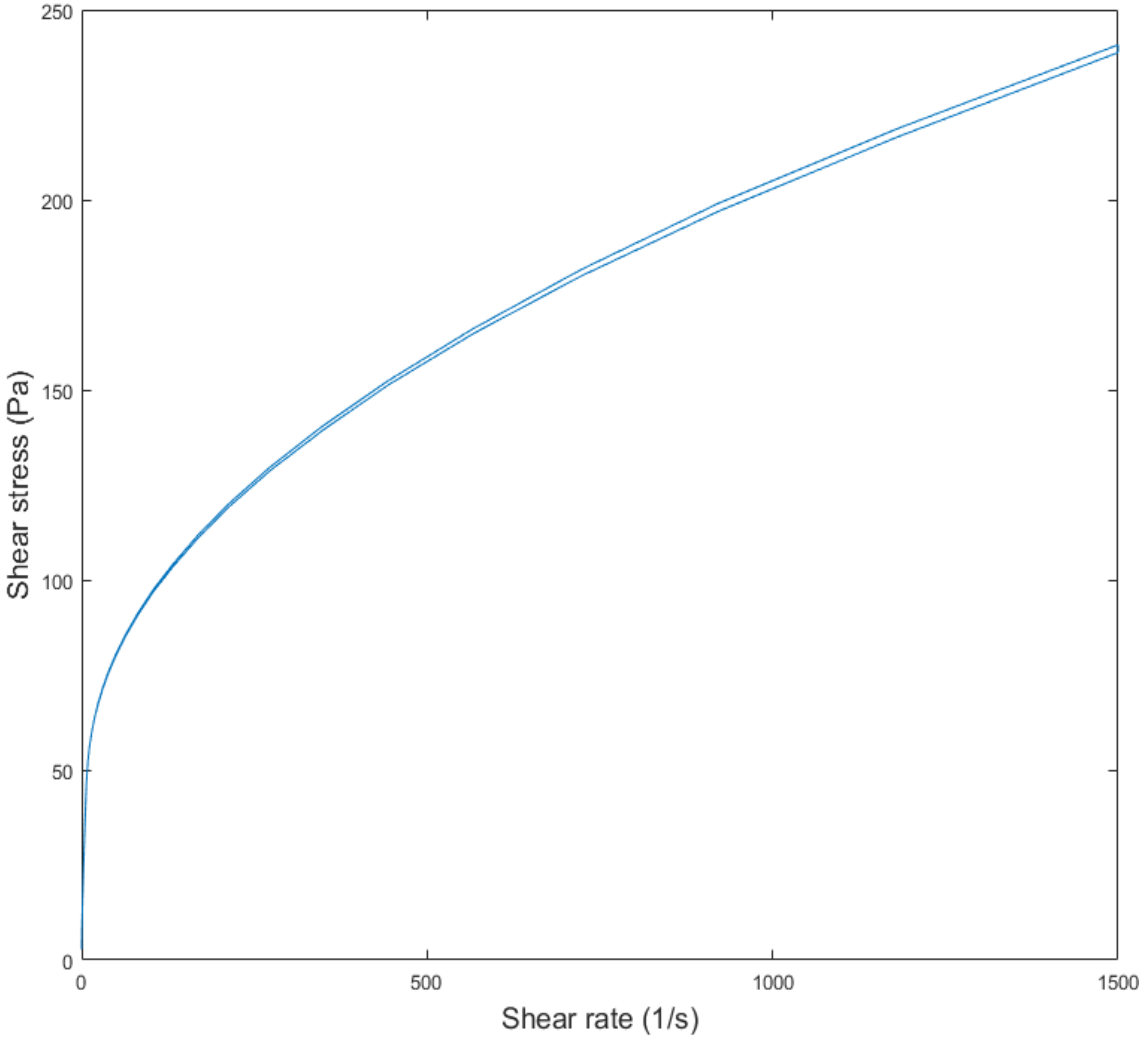

Figure 65. The Anton Paar rheometer test of the Carbopol® consisted of a ramp up, hold and ramp down test. No hysteresis was observed.

Appendix VII Takagi python function

See supplemental attachments for the complete code

```
def takagi_model(nu,h,beta,a,b):

    ''' Calculates velocity from Takagi Huppert model given a kinematic viscosity '''
    dict = {}

    # declare all constants
    Beta = (beta*np.pi)/180          # inclination angle of v-channel (3*np.pi)/180
    h = h/1000                       # Depth of flow in meters

    g = 9.81                         # Earth gravity in m/sec^2
    i = 0;j = 0                      # initialize sum iterators
    theta = np.pi/4                  # v shaped boundary with sidewalls meeting at 2theta or
np.pi/4
    m = np.tan(theta)                # half the distance in the x direction
    x = np.linspace(-1,1,100)*m*h    # Creates an array
    y = h
    X = (1/h) * (y + (x/m)) -1       # from TAKAGI & HUPPERT (2007) eqn 2.23a,b
    Y = (1/h) * (y - (x/m)) -1
    M = (g/nu) * np.sin(Beta)
    u = 0
                                     # Iterate of the double sum formulae
    for i in range(10):
        lamda_i = np.pi*(0.5+i)
        for j in range(10):
            lamda_j = np.pi*(0.5+j)
            a_i_j = ((-1.0)**(i+j))*4*M* m**2* h**2/ (  (1+m**2) * lamda_i * lamda_j* (
lamda_i**2 + lamda_j**2  ))
            u = u + a_i_j * np.cos(lamda_i*X) * np.cos(lamda_j*Y)
```

```
    dict = {'Incline angle in degrees (B):   ':(beta),'Depth of flow (m):   ':h,'Kinematic Viscosity m^2/s:   ':nu*1e3}


    z2 = np.polyfit(x*1e3, u*1e3, 3)                    # calculus
    q2 = np.polyint(z2)
    Area_Takagi = abs(np.diff(np.polyval(q2,[a,b])))
    Area_Takagi = abs(round(Area_Takagi[0],5))

    return x,u,dict,Area_Takagi
```